UNIVERSITÀ DEGLI STUDI DI PADOVA

Dipartimento di Fisica e Astronomia "Galileo Galilei"

Corso di Laurea Magistrale in Astronomia

Tesi di Laurea

The current limits in the photometry of galaxies

Relatore

Prof. Mauro D'Onofrio

Laureando

Giulia Golini

Anno Accademico 2018/2019

A chi non c'è più...

Abstract

The search for faint astronomical objects allows us to deepen our knowledge on galaxy formation and evolution. Some unresolved cosmological questions like the apparent absence of stellar halo in some galaxies, the problem of the missing galactic satellites and the relative abundance of light and matter in the Universe can be explained through the study of faint tidal features around disk galaxies, faint extended stellar halos and ultra-diffuse-galaxies. The observation of these faint astronomic structures is a very challenging issue. Sources with magnitudes fainter than 30 $mag/arcsec^2$ in the r-band are very difficult to detect mainly due to the light coming from bright objects scattered in the optics of the telescope, CCD defects, ghosts and the background sky radiation. In this thesis I present the steps of an optimized reduction-pipeline developed for the Hipercam-camera mounted on the Gran Telescopio de Canarias (GTC), which allows cleaning up the science images from the main noise sources in order to obtain images of dark galaxies that the current photometric deep surveys are unable to detect. I will focus on the main problems that I encountered during the data-reduction, such as the difficulty of obtaining a good-quality Master-flat, the troubles in the sky subtraction and the problem of building a good mask to identify the edges of the galaxy to estimate its brightness. In particular, this Hipercam pipeline is used to unveil the nature of an extended and extremely low surface brightness galaxy located at $RA = 20.86418538$ h and $DEC = -0.6229532711$ detected in the IAC Stripe 82 Legacy Survey, very close in projection to the Abell 194 cluster ($z = 0.0275$), more or less at the distance of Coma. The work I conducted succeeded in obtaining a high resolution RGB color image and a first approximation of the brightness of this unknown galaxy, the basis to learn its outskirts, to investigate whether this object can be resolved into stars, to study in deep its dark matter halo mass, its stellar population gradient and its formation. This Hipercam-pipeline is open source and it is available for download at *https//gitlab.com/Giulia Golini/hipercam-pipeline.*

I limiti attuali della fotometria delle galassie

La ricerca di sorgenti astronomiche molto deboli si rivela estremamente importante in quanto permette di approfondire ed ampliare le nostre attuali conoscenze in merito alla formazione e alla storia delle galassie. Alcune questioni cosmologiche irrisolte, come l'apparente assenza di alone stellare in alcune galassie, il problema dei satelliti galattici mancanti e la relativa abbondanza di luce e materia nell'Universo, possono essere spiegate proprio attraverso lo studio di strutture molto deboli osservate attorno alle galassie a disco, di estesi aloni stellari a bassissima luminosità e di galassie "ultra diffuse". L'osservazione di queste deboli strutture astronomiche è molto complessa, risulta assai impegnativa ma allo stesso tempo stimolante. Le fonti con magnitudine inferiore a 30 $mag/arcsec^2$ nella banda R si sono dimostrate assai difficili da rilevare a causa della luce proveniente da altri oggetti più luminosi che viene deviata nell'ottica del telescopio, dei possibili difetti di costruzione dei CCD e della radiazione emessa dal cielo notturno (background). In questa tesi presento i passaggi fondamentali di una pipeline di riduzione dati da me sviluppata ed ottimizzata per la Hipercam camera montata sul Gran Telescopio de Canarias (GTC). Questo metodo consente di ripulire le immagini scientifiche dalle principali fonti di rumore, siano esse luminose, termiche e quant'altro, al fine di ottenere immagini di galassie di bassa brillanza superficiale che i telescopi attuali più utilizzati non sono in grado di rilevare. Mi soffermo in particolare modo sui principali problemi che ho riscontrato durante la riduzione dei dati come la difficoltà di ottenere un Master flat di buona qualità, quella di creare un modello che sia abbastanza rappresentativo dell'emissione del cielo ed inoltre di costruire una maschera che, togliendo le sorgenti puntiformi che si sovrappongono a questo tipo di galassie a allo stesso tempo consentendo di individuarne i confini, ci permetta di studiarne la luminosità. Nello specifico, questa pipeline viene utilizzata per svelare la natura di una galassia estesa con brillanza superficiale estremamente bassa avente coordinate RA =20.8641853h e DEC = −0.6229532711, rilevata per la prima volta nell'IAC Stripe 82 Legacy Survey. Questa galassia risulta essere molto vicino, in proiezione, all'ammasso Abell 194 (z =0.0275), all'incirca alla medesima distanza dell'ammasso di Coma (∼100 Mpc). Il lavoro svolto mi ha permesso di ottenere un'immagine RGB ad alta risoluzione di questa galassia sconosciuta e di stimarne approssimativamente il valore della sua luminosità. Ritengo che lo studio da me esposto in questa tesi possa considerarsi una buona base di partenza per riuscire ad analizzare le caratteristiche morfologiche e le proprietà fisiche di questa galassia; per indagare se quanto individuato possa essere o meno risolto in stelle, per valutare la possibile esistenza di un alone di materia oscura ed ipotizzarne l'origine e la futura evoluzione. Questa pipeline Hipercam è pubblica ed è disponibile per il download all'indirizzo *https//gitlab.com/Giulia Golini/hipercam-pipeline.*

Acknowledgments

I am so grateful to Raul Infante Sainz, who has been an inspiring and patient advisor for a student who did not know how to solve debugging problems. He is very intuitive. He also allowed me to learn at my own and to grow as an independent researcher. I would like to acknowledge Ignacio Trujillo for everything he provided for me. He taught me how to think scientifically. I admire his wide range of knowledge. I am also grateful to Nuskia Chamba who helped me to build the RGB image. She was always very kind. I also acknowledge the comments from the supervisor Mauro D'Onofrio who helped me to write scientifically and gave me the opportunity to work on this thesis at the IAC in Tenerife, Spain. I acknowledge financial support from University of Padova. And I am so grateful to my family. They always have been supportive and patient. They helped me grow as a student and as a person.

Contents

Introduction

Figure 1: Ultra Diffuse Galaxy observed with GTC.

Deeper and deeper in the universe, far away, in time. How far have we gone? Can we go further to find out what we still do not know about the nature of galaxies? Is it possible to detect objects so weak that even Gaia or Hubble are unable to detect? Over the past 15 years, a number of surveys have succeeded in locating low surface brightness galaxies. There is no convention for defining low surface brightness; discussion is mostly restricted to galaxies with central surface brightness fainter than $\mu_0 = 23\ mag/arcsec^2$ B-band, and they include objects as diverse as giant gas-rich disks and dwarf spheroidals. One of the first astronomers who discovered an exponential tail of mostly low

surface brightness dwarfs was Zwicky in 1957 [1] and only few years later we got the first catalog (The David Dunlap Observatory) to contain a significant number of diffuse galaxies with low mass [2]. Many LSB dwarfs were detected in the survey of the Virgo cluster by Binggeli, Sandage & Tammann in 1985 but the next major steps forward came with the Sloan Digital Sky Survey and with the Hubble Ultra Deep Field [3] [4]. Despite these numerous observational steps forward there are lots of questions on galaxies formation and evolution that remain unsolved.

In Chapter 1, I focus on the main characteristics of LSBGs, taking particular attention on the importance that these faint objects have in astrophysics to explain the discrepancies between theoretical predictions and observations. As an example, though Lambda Cold Dark Matter cosmology predicts all the faint features surrounding Milky Way-like galaxies actually detected [5] [6] [7] [8] and the morphological match to the cosmological simulations constitutes new evidence that theoretical models apply to a large number of other Milky Way-mass disk galaxies in the Local Volume [5], there are some important gaps in our present understanding of galaxy scaling relations and what they can tell us about galaxy formation [6] [9]. Studies carried out on the circular velocity distribution function of galaxy satellites in the Local Group show that models are very different from observed ones: The hierarchical clustering scenario theorizes that galaxies are created by the accretion of about 300 satellites of different sizes and masses inside a 1.5 Mpc radius, but some of them seem to be missed and only 40 satellites are actually observed [10] [11]. Moreover, despite the observations of common faint tidal features around disk galaxies, like around Sagittarius [12] and Andromeda [13], there are galaxies with apparent absence of stellar halo such as the massive M101 [14]. Low surface brightness galaxies are so important because they offer a new window onto the diversity of galaxy morphology and on the relative abundance of light and matter in the Universe [1] [15] [16]. As a matter of fact, the M/L ratio of these galaxies is typically larger than that of normal galaxies with the same total luminosity and morphological type [15] and it is believed that LSB galaxies are the major baryonic repositories in the local Universe. In addiction, it is assumed that the relatively flat faint-end slopes of the luminosity function of galaxies are attributed to photoionization or suppressed cooling [17] but there is an extreme disagreement between observations and predictions at the low-mass end.

To fill these gaps comes the need to develop new techniques to observe ever fainter astronomical sources and, desirably, outside the environment of the Local Group. A further gain in sensitivity is achieved by digitally stacking scans of existing sky survey plates. As an example, the APM group at Cambridge have attempted to make an objective survey for LSBGs by using the APM machine to scan UKST plates of the Fornax Cluster area reaching a limiting magnitude of 26.5 $mag/arcsec^2$ r-band [18].Another chance is to use Tech Pan emulsions as it was done from the UK Schmidt Telescope to study the Virgo cluster up to 27 $mag/arcsec^2$ r-band [19]. Studies based on star counts of Local Group galaxies are able to reach effective surface brightness levels of 30 $mag/arcsec^2$ [20]. However, a huge part of the dark universe remains unseen below this magnitude limit mainly owing to scattered light, interstellar dust, sky emission and technical problems [21].

The idea that galaxies can be overwhelmed by the brightness of the night sky was first commented by Zwicky (1957) but until the 1970s low surface brightness is not what most telescopes were optimized for, the priority was given to telescopes aimed at resolving point-like sources and not at large-scale low-light sources. In 1976 the astronomer Disney investigated the observational bias

against galaxies with low surface brightness concluding that these were effectively under-represented. The confirmation that the sky background plays a significant role came with McGaugh in 1995, who found the space density of galaxies as a function of disk central surface brightness to be flat toward the fainter side and to have a sharp decline toward the brighter side of the Freeman value, meaning that LSBGs were really under-estimated [1]. Many bright extended galaxies we observe by using very deep surveys like The Canada-France-Hawaii Telescope Legacy Survey [22] show artificial features that look like holes around them. These structures are produced by a too aggressive reduction pipeline, in which the foreground sky is over-subtracted and the real signal from galaxy halos or inter-cluster light is confused with background [23]. Even SDSS reduction pipeline is not optimized for astronomical structures that are close to the night sky emission.

Another serious issue when observing the dark universe is the pollution by Galactic cirrus of dust around our galaxy. The cirrus emission was discovered by the Infrared Astronomy Satellite (IRAS) in 1984 and manifests itself as photon noise whose fluctuations are Poissonian. Any brightness fluctuation at scales below those of the beam size could be mistaken with the real sources. As a matter of fact this faint emission around 27 $mag/arcsec^2$ can partially block and confuse our sight by mimicking the shape and brightness of faint extragalactic features. The steep power spectra of Galactic cirrus peaks at FIR wavelengths, it can be explained by the presence of dust at various temperatures [24] [25] but the physical emission process is still not well characterized [9] [26] [27] [28] [29] [30] [31].

Furthermore, reflections in the camera and in the optics of telescopes can generate fringing or ghosts that could be confused with stellar halos that surround galaxies. Tidal tails or the intra-cluster light in which cluster galaxies are embedded could be hidden by the scattered light coming from bright stars or nucleus of galaxies. In this case a good characterization of the PSF of the camera and a good quality Master-flat is needed [7] [21] [23] [32] [33] [34].

In Chapter 2 I illustrate a new technique, a new reduction pipeline for faint-sources thanks to which I managed to build a color image of an ultra-diffuse galaxy with a resolution better than that of SDSS9. The work I conducted at the Instituto de Astrofísica de Canarias (IAC) with the help of the astrophysicists Trujillo and Infante-Saintz, consisted in optimizing the Hipercam-camera reduction pipeline mounted on the 10.4 m Gran Telescopio de Canarias (GTC) and, taking into account all of technical problems related to the observation of faint objects, to succeed in showing a color image of a dark unknown galaxy located at RA = 20.86418538h and DEC= -0.6229532711 detected in the Stripe 82 survey.

Figure 2 points out the result of my work whereas, Figure 3 presents the sky seen with SDSS9. The difference is remarkable, it is evident that the number of sources detected with GTC is so much greater and it is impossible to see the ultra diffuse galaxy in the middle with the Sloan.

In the same chapter of this thesis I describe briefly the structure of the Hipercam camera and the image acquisition procedure. Subsequently, I describe the main steps of the pipeline, paying particular attention to the problems I encountered while working on images such as the flat which is done two times and by stacking all science images, the gain correction to arrange images, the sky polynomial fit and the issue on U-filter astrometry due to too few sources in each single image. To build the pipeline I worked with the GNU-Make software and the Python Programming Language,

all the steps are saved on the website $< https://gitlab.com/GiuliaGolini/hipercam-pipeline >$. The pipeline is fully automatic for all five optical filters until the sky subtraction, after which I decided to proceed with one filter per time to avoid any bugs. With a 2,3 GHz Intel Core i5 processor computer it takes around 2 hours and a half to compute the final stacked image for one filter.

In Chapter 3 I present how I performed surface photometry on the galaxy to investigate on its brightness, structure and mass. After that I discuss prospects for future research.

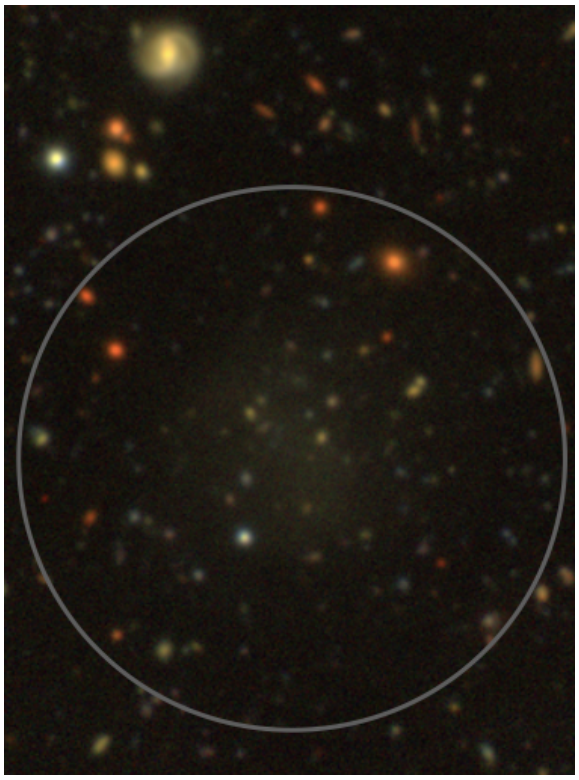

Figure 2: UDG with GTC.

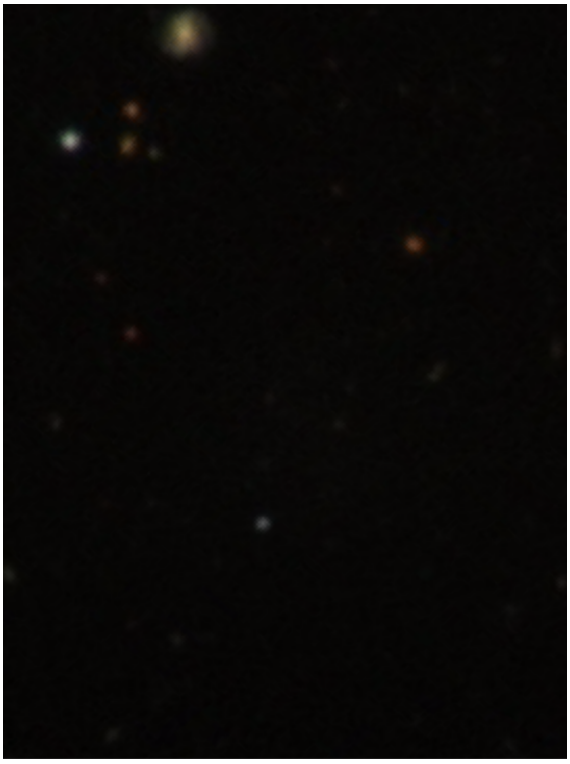

Figure 3: UDG with SDSS9. Aladin Lite.

Chapter 1

Low surface brightness galaxies

Our knowledge of Low Surface Brightness galaxies (LSBGs) is still limited and many issues regarding their formation, morphology and evolution remain poorly understood. In this Chapter I present the main features shared by almost all LSBGs, I illustrate the hypothesis on where and when they form, the supposed theories on the physical processes that happen inside and around their environment, their very high mass-to-light ratio and the gaps that have to be filled between predictions and observations on low surface brightness galaxies formation and evolution. Figure 1.5 presents four optical images of four different LSB galaxies from McGaugh (1995b), in $2'$ x $2'$ box. Each object shows a different structure [35].

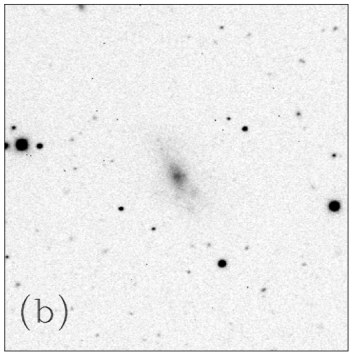

Figure 1.1: D6465 Galaxy, V band.

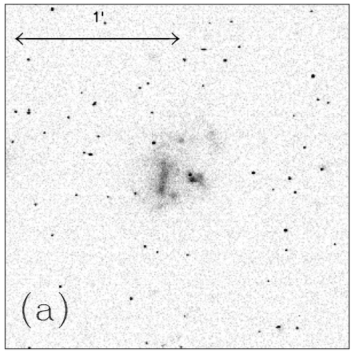

Figure 1.2: F563-V2 Galaxy, V band.

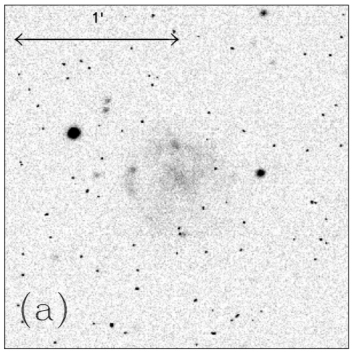

Figure 1.3: F561-1 Galaxy, V band.

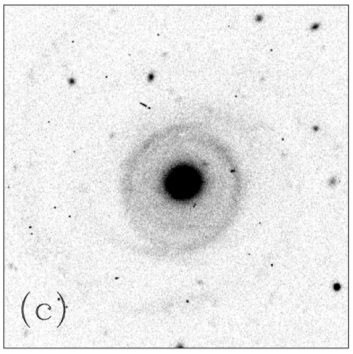

Figure 1.4: UGC6614, V band.

Figure 1.5: Low surface brightness galaxies. McGaugh et al. (1995b).

1.1 Characteristics of low surface brightness galaxies

1.1.1 Brightness and Space density distribution

Low surface brightness galaxies are mostly late-type galaxies. The discs of the spiral galaxies follow an exponential superficial brightness profile $I(r) = I(0)exp(-r/r_0)$, measured along the major axis of the galaxy image. Until few years ago, the value of $I(0) \sim 140\ L_{\odot}pc^{-2}$ was believed to be about constant corresponding to $\sim 21.7\ mag/arcsec^2$ in B band (Freeman's Law). Subsequent observations have instead shown a population of spiral galaxies systematically lost in the previous observations, with surface brightness lower than the Freeman value. The first Catalog of Low Surface brightness Galaxies came out in 1963 by Sidney van den Bergh. It is the David Dunlap Observatory (DDO) consisting in many diffuse, low mass, faint galaxies located in the Local Group at z $\leq$ 0.1 [1]. In 1982 the astronomer Longmore characterized LSB galaxies as extended and relatively quenched systems with large exponential scale lengths ($r_0 \geq 10$ kpc), gas-rich and with low central surface brightness (low surface flux density). It is now common to classify as LSB those galaxies with a central surface brightness below $\mu_0 = 23$ B-band $mag/arcsec^2$. At the present day galaxies with $23 \leq \mu \leq 24.5\ mag/arcsec^2$ in the r band are 'Classical low-surface-brightness galaxies' (Cl. LSBGs) and galaxies with $\mu \geq 24.5\ mag/arcsec^2$ [36] in the r band are called Ultra-diffuse galaxies (UDGs). LSB galaxies have been observed since 80s but the first discovery of UDGs, in the Coma cluster by van Dokkum was few years ago in 2015. UDGs represent the fainter end of the LSB galaxy population with optical luminosity typical of dwarf galaxies (L $\sim 10^{7-8}L_{\odot}$) but half light radii typical of much larger spirals, such as the Milky Way ($R_e \sim 1.5 - 5$ kpc).

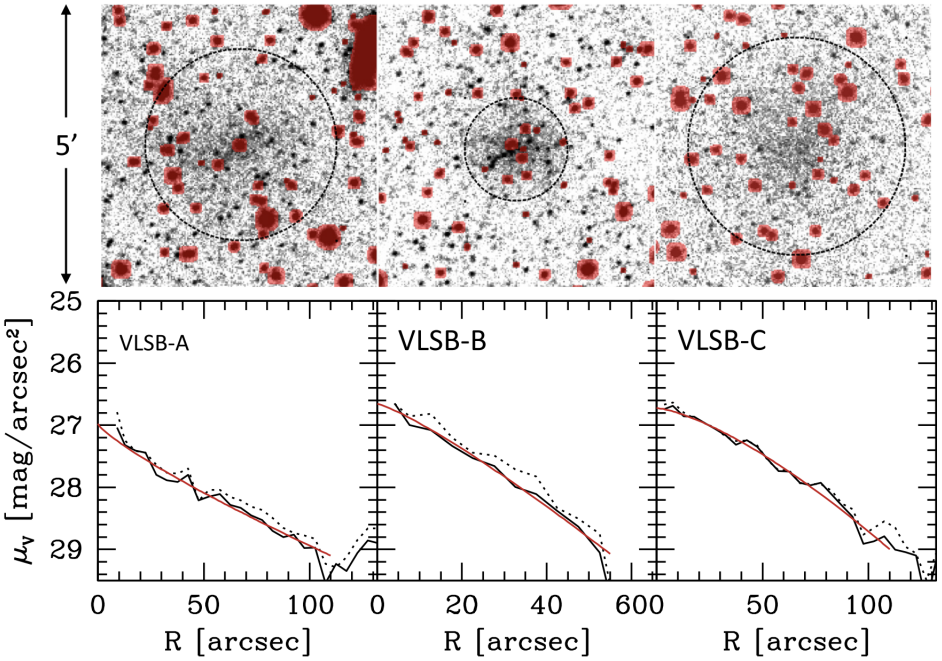

Figure 1.6: Schmidt imaging of LSB galaxies in Virgo cluster on the top and their surface brightness profiles on the bottom. Credits to Mihos et al. (2015).

UDG candidates were discovered with William Herschel Telescope in the Perseus cluster core by Wittmann in 2017 with mean effective V-band surface brightness ranging from 24.8 $mag/arcsec^2$

to 27.1 $mag/arcsec^2$ with half-light radii up to 0.7-4.1kpc [37]. Figure 1.6 shows the surface photometry for three large (half-light radii 3-10 kpc) low surface brightness galaxies with $2 \cdot 10^7 L_\odot \leq L_V \leq 9 \cdot 10^7 L_\odot$ in the Virgo cluster. The observations were carried out with the Burrell Schmidt telescope by Mihos in 2015. Surface brightness profiles were built by using both the average which includes the light from the fainter unmasked sources (dotted black curves) and median which traces the diffuse light alone (solid black line) pixel intensities as a function of radius [38]. Red curves identify Sersic fits to the median profiles. We can realize that, by studying only three galaxies, low surface brightness galaxies are quite diverse in their physical properties. With the Dark Energy Camera wide-field camera mounted on the 4-m Blanco telescope at the Cerro Tololo Inter-american Observatory in 2015 Muñoz reported the discovery of faint galaxies in Fornax cluster core regions. Figure 1.7 reports an illustration of 3 square degrees centered on NGC 1399, the brightest Fornax galaxy. Low surface brightness galaxies are marked with a red circle while dwarf galaxies identified by Ferguson are marked with small grey circles [39]. Moreover, Janssens [40] reported the discovery of UDGs in the massive galaxy cluster Abell 2744 at z = 0.308 with the Hubble Frontier Fields program.

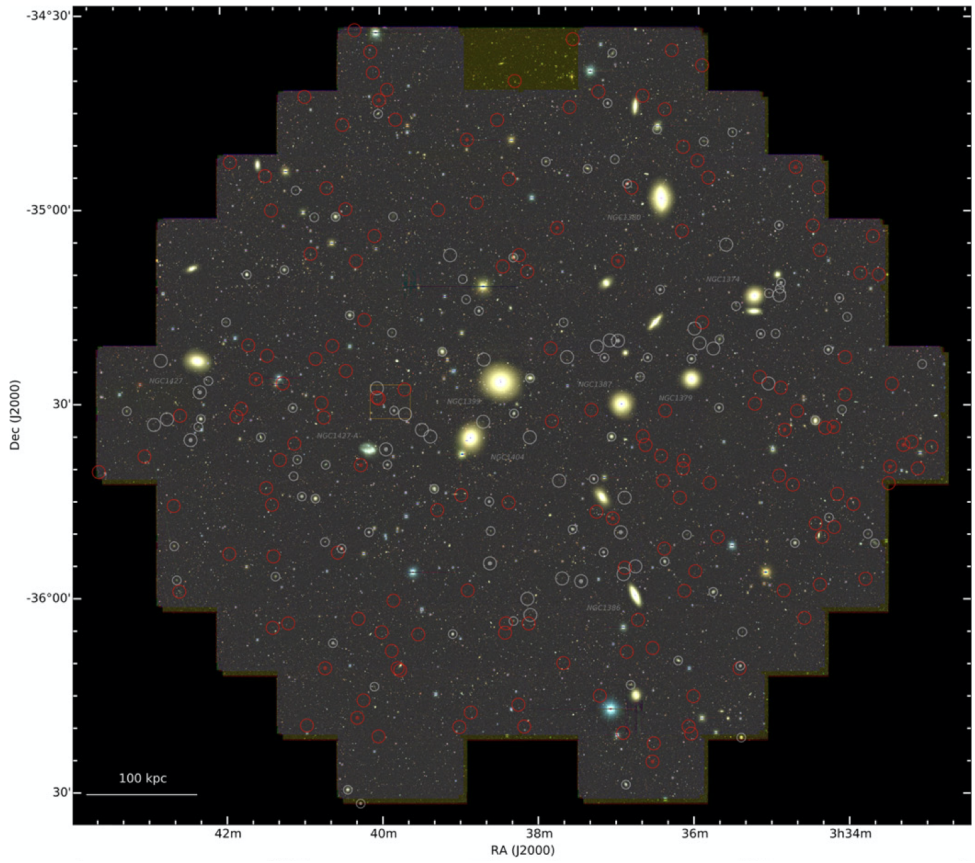

Figure 1.7: UGI color image of Fornax cluster. LSB galaxies marked by red circles. Credits to Muñoz et al. (2015).

This kind of galaxies is not only found in clusters. As a matter of fact galaxy groups such as Centaurus A, M77, M96 and Leo-I contain lot of LSB galaxies but faint objects are also found in the fields of nearby galaxies such as NGC 4594 (M 104) and NGC 5457 (M 101) by Javanmardi in 2016 or filaments [41]. It is worth nothing that the abundance of field UDGs is at least comparable

to the abundance of those in clusters and groups [42]. Ultra diffuse galaxies located in cluster tend to be red, dark matter-dominated with old and metal-poor stellar populations, their abundances is proportional to the host cluster halo mass, and they are usually not found in the centre of clusters. This fact is due to the possible, but observationally rare, disruption and dissociation of UDGs by the strong tidal forces in the inner regions. Another possibility is their more recent infall into the clusters than the dwarf counterparts so that UDGs have not arrived in the inner regions yet. In contrast, in lower density environments these faint objects tend to be bluer, more irregular, gas rich with younger and more metal-rich stellar populations.

The technical drawback in detecting sources as faint as, or even fainter, than that of the night sky give rise to a significant bias in galaxy catalogs. As a matter of fact, due to their faintness and their low brightness, LSBGs are subject to severe selection effects. The previously discussed Freeman law is no more representative of the general population of galaxies, there is a space density of galaxies which is higher than predicted, there is an over-density at low brightnesses. A significant number of galaxies are distributed on a continuous tail extending towards the left side of the graph in Figure 1.8 which shows the space density of galaxies as a function of central surface brightness. McGaugh (1996) was the first to fit a flat line to the data.

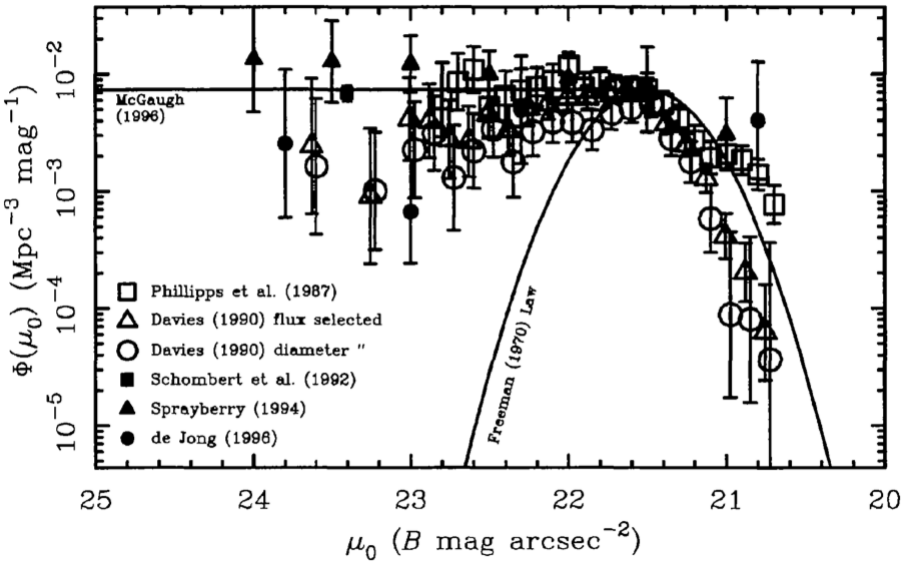

Figure 1.8: Space density of galaxies as a function of central surface brightness B-band. Credits to Bothun.

Figure 1.9 remarks that faint galaxies are more than the high brightness counterpart and the predicted amount of space density of galaxies below 23 $mag/arcsec^2$ must be corrected. The extrapolated curve continues almost flat towards the left side of the graph. Increasing new technologies have proven that low surface brightness galaxies exist, and they are many, with a number density which outnumber that of the high surface brightness galaxies.

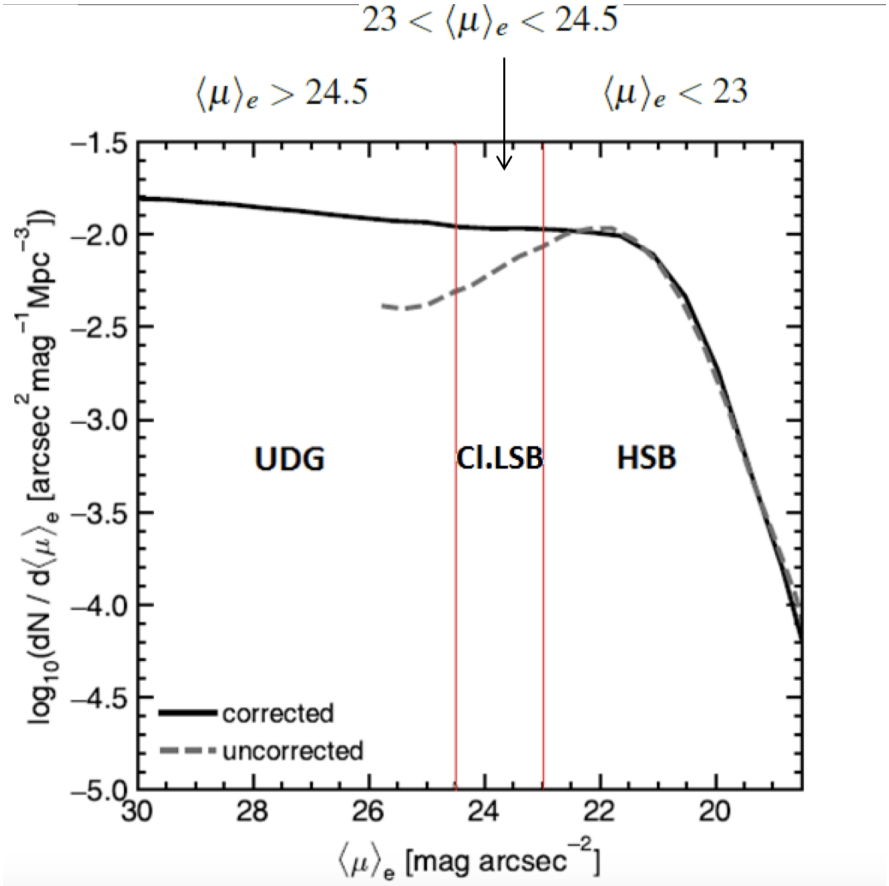

Figure 1.9: Space density of galaxies as a function of central surface brightness B-band. Credits to Bothun.

1.1.2 Masses and sizes

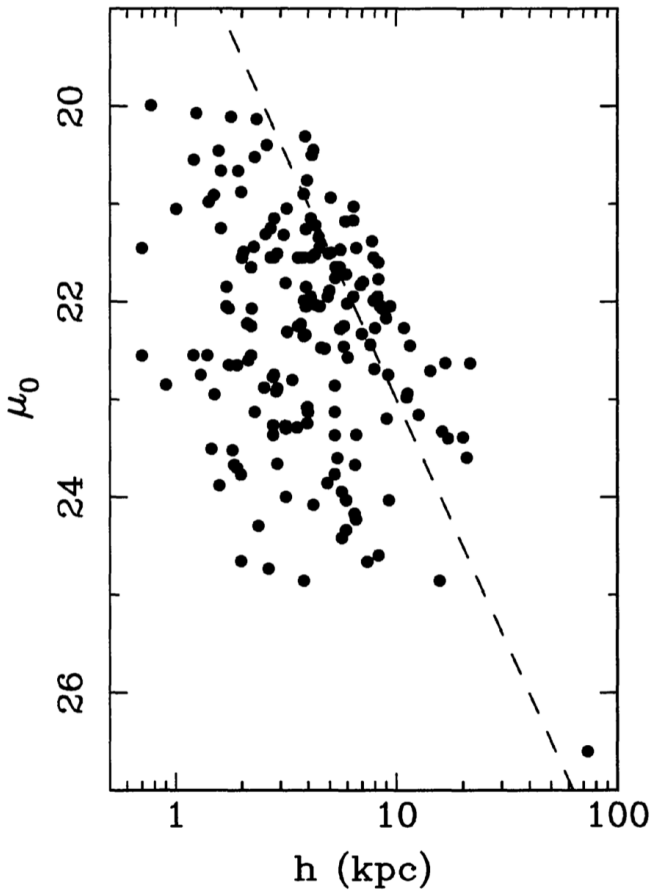

Figure 1.10: Surface brightness to scale height for a sample of galaxies B-band in the Hubble Sequence. LSB data come from McGaugh and Bothun (1994) and Sprayberry (1994) and the HSB data come from de Jong (1995). Credits to Bothun.

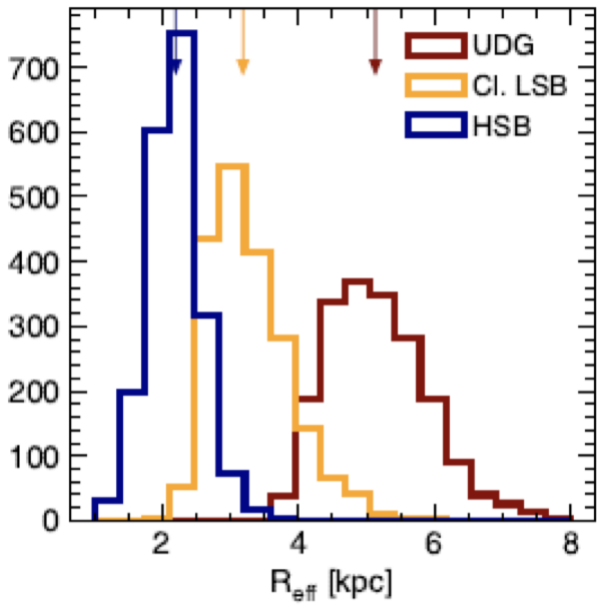

Figure 1.11: Effective radius for a sample of galaxies. Credits to G. Martin et al.(2019).

LSB objects are not exclusively large systems of similar sizes as characterized by Longmore. Figure 1.10 plots the position of a sample of galaxies in the Hubble sequence in the surface brightness vs radius plane, with scale length spanning from 1 to 100 kpc. There seems to be correlation; with decreasing surface brightness effective sizes become larger. As said previously, the subset of larger systems with radius ranging from 2 kpc to 8 kpc, with surface brightness values $\mu_0 \sim 25$ $mag/arcsec^2$ in the B-band, and with low stellar masses ranging from $\sim 10^6 M_\odot$ to $\sim 10^8 M_\odot$, are the ultra diffuse galaxies. It is highlighted in Figure 1.11 the effective radii of UDG, LSBGs and HSBGs in blue, yellow and red respectively. It is remarked that, statistically, with increasing luminosity, sizes are decreasing.

Figure 1.12 presents a color image of an example of UDG, the Dragonfly 44 one, observed with Keck II and Gemini North telescopes in Hawaii. Dragonfly 44 has a luminosity of $L_V = 2 \cdot 10^8 L_\odot$ and it is located 300 million light-years away in Coma cluster, surprisingly it has a mass similar to that of the Milky Way and it is almost entirely composed of dark matter. Its velocity dispersion is about 50 km/s, its dynamical mass of $M_{dyn} \leq r_{half-light} = 0.7 \cdot 10^{10} M_\odot$ within its de-projected half-light radius and a mass-to-light ratio of $M/L(\leq r) \sim 48 M_\odot/L_\odot$.

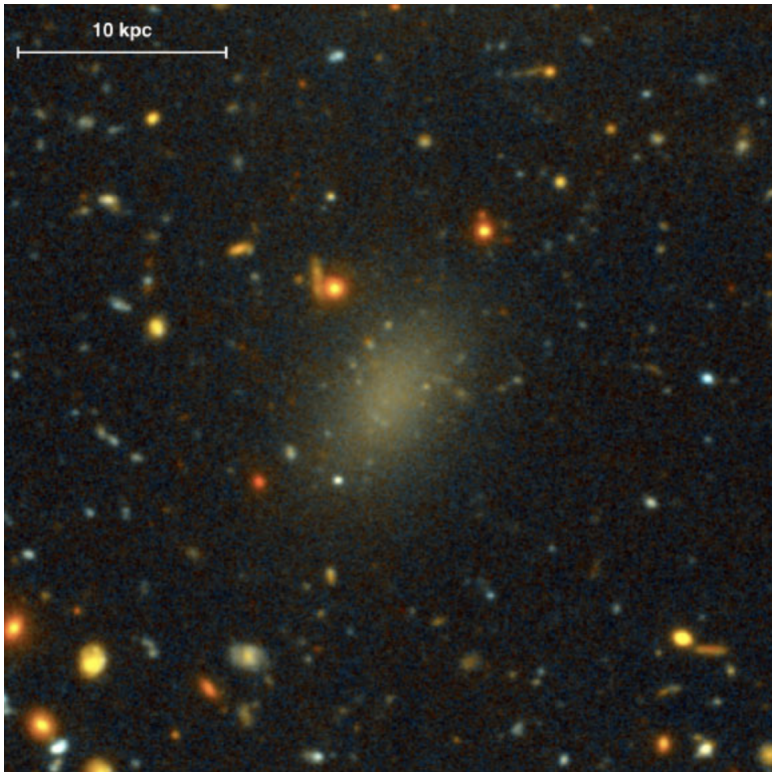

Figure 1.12: Dragonfly44 UDG. Image credit: Pieter van Dokkum / Roberto Abraham / Gemini Observatory / SDSS / AURA.

Turning back to Figure 1.10, we observe that on the left side of the graph there are also few objects detected by Schombert in 1995; the firsts LSB dwarf spirals and irregular drafts with very low surface brightness and smaller scale lengths ($\sim 1 - 2$ kpc for luminosity below 0.01 $L_\odot$). LSB galaxies are not even just low-mass galaxies as it was in the David Dunlap Observatory catalog. As a matter of fact, in 1987, the serendipitous discovery of the giant LSB disk galaxy Malin 1 (bottom left dot in Figure 1.10) in the Next Generation Virgo Cluster Survey [43] made this galaxy the

first prototype of giant systems (Giant Low Surface Brightness galaxies) which have low surface mass density stellar disks, large physical sizes (∼160 kpc, about 4 times that of the Milky Way) and enormous amounts of neutral hydrogen ($\sim 10^{11} M_{\odot}$) [44] [45]. Figure 1.13 illustrates an optical image of Malin 1 obtained using the Magellan/Clay telescope (6.5 m). Malin 1 presents well-formed spiral arms down to $\mu_B \sim 28\ mag/arcsec^2$ and it exhibits a clear bright inner region [46].

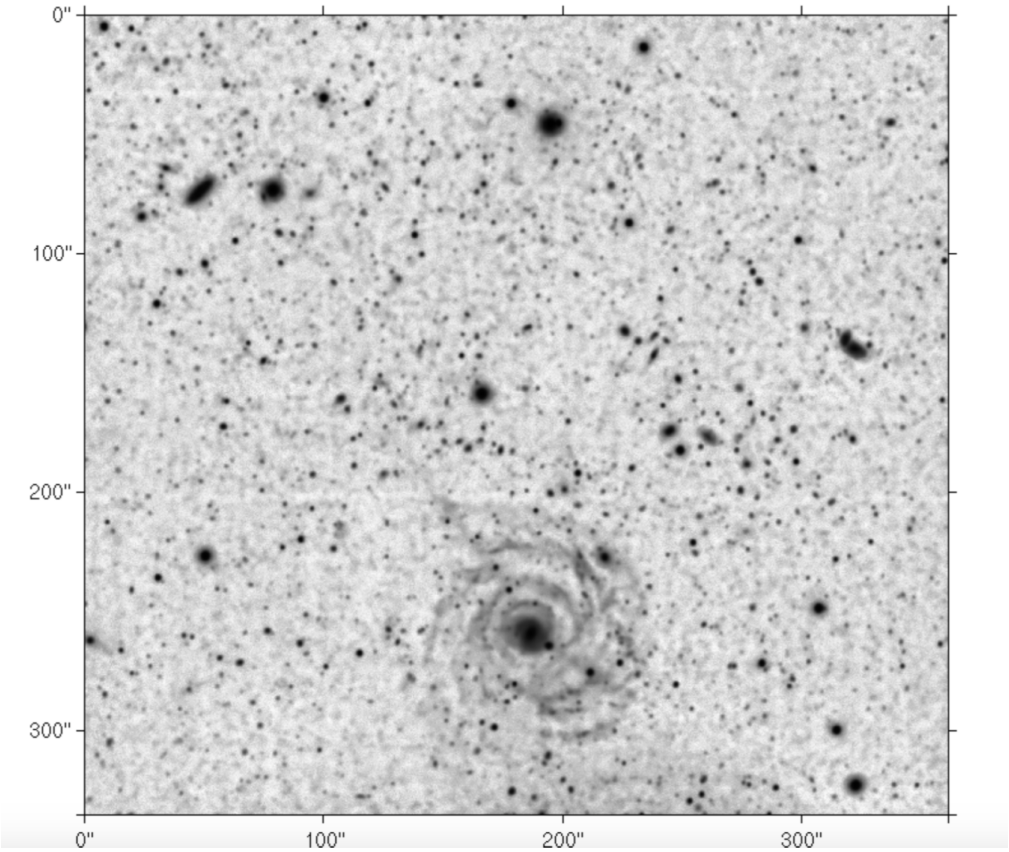

Figure 1.13: Optical image of Malin 1. Credits to Galaz.

The effective radius versus stellar mass for an arbitrary selection of galaxies in the Local Universe is plotted in figure 1.14. Blu, yellow and red dots came from the Horizon-AGN simulation, while the other data from previous works by McGaugh.

Thanks to the increasing advanced observational techniques and new wide-field surveys such as the Sloan Digital Sky Survey more and more LSB galaxies and Ultra Diffuse Galaxies are being discovered. Low surface brightness galaxies are a heterogeneous family then, spanning the entire galactic mass range from most massive disk LSB galaxies such as Malin 1 with $M_{stars} \geq 10^{10} M_{\odot}$ and $M_{gas} \sim 10^{10} M_{\odot}$ to the extremely diffuse elliptical drafts. LSBs objects can be either smooth disks or irregulars without any brighter central part and with a higher or lower metallicity depending on their evolution in their surroundings. Figure 1.15 summarizes the typical characteristics while distinguishing the galaxies in the three groups according to the brightness; an ultra diffuse galaxy, a low surface brightness galaxy and a high surface brightness galaxy respectively. Sizes are smaller with increasing surface brightness and colors are bluer with decreasing surface brightness, however there may be exceptions within groups.

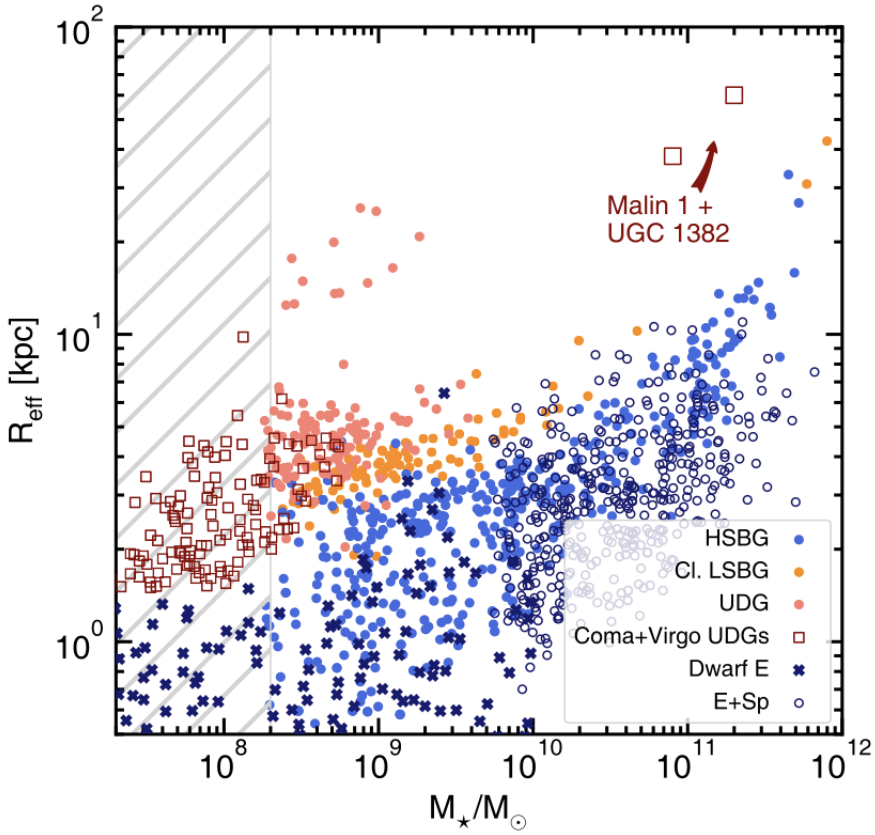

Figure 1.14: Effective radius vs stellar mass. Credits to G. Martin et al.(2019).

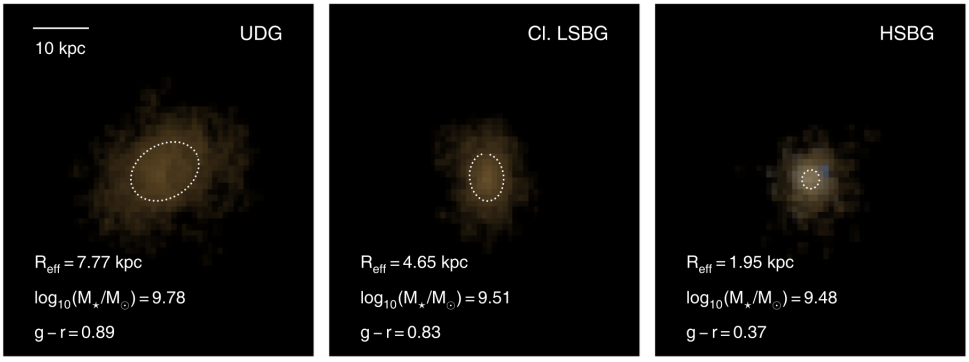

Figure 1.15: g, r, and i-band false color images of low-mass Horizon-AGN galaxies. The dotted white ellipses are isophotes that contain half of the galaxy's r-band flux [47]. Credits to G. Martin et al.(2019).

1.1.3 Rotation curves and Tully-Fisher relation

The dynamical mechanism of the rotating LSB disks has long been misunderstood, until very recently. LSB disk galaxies in the optical bands rarely show any kind of symmetry, they usually manifest a chaotic pattern that suggest a peculiar kinematics. To study the speed at which each part of the galaxy moves and how galaxies rotate astronomers use the rotation curve, where the rotation velocity of the galaxy gas is usually obtained through the radio 21 cm HI emission. The innermost part of the galaxies rotates like a rigid body, so the angular velocity does not depend on the radius and the radial velocity increases with increasing radius. Outside this region the speed initially rises, then gradually should decrease. However, the observational data for different spiral galaxies were not in agreement with the predictions for a Keplerian rotation curve. This is because we need to take into account the actual mass distribution in galaxies, disk, bulge and dark matter. A small number of HI rotation curves of LSB giants have been published, but velocity dispersion for the LSB dwarfs are beyond the capabilities of existing telescopes, so they are usually poorly sampled [48]. However, the results obtained by many observational efforts on rotational curves indicate that LSB galaxies with the same rotation velocity and mass of HSB galaxies have a shallower rotation curves at small radii and maximum velocities are typically between 50 km/s and 120 km/s. Figure 1.16 displays the comparison of the observed rotation curves of two galaxies, morphologically very similar, with a factor of 10 difference in surface brightness that occupy identical positions on the Tully-Fisher relation: LSB galaxy UGC 128 (24.2 $mag/arcsec^2$ B band) and HSB galaxy NGC 2403 (21 $mag/arcsec^2$ B band) [49]. By looking at these shapes we can evince that in LSBGs the rotation curve is slowing rising until it become constant though the asymptotic velocity is the same as for NGC 2403. Moreover, the gas is dynamically more important in UGC 128 and its amount of dark matter must dominate down to a small radius.

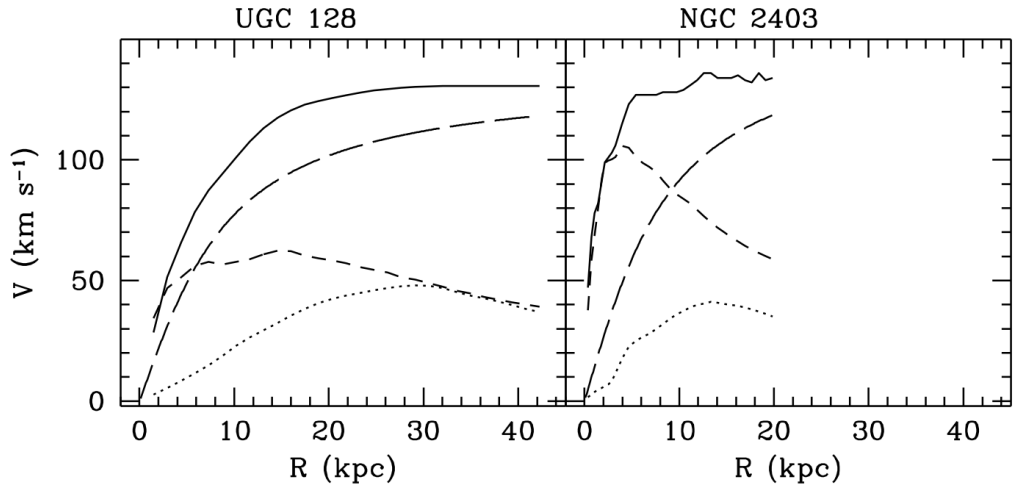

Figure 1.16: Rotation curves of LSB galaxy UGC 128 and HSB galaxy NGC 2403. The drawn lines are the observed rotation curves; the dotted lines represent the rotation curves of the gas components; the short dashed lines are the rotation curves of the disk, scaled to maximum disk; the long-dashed lines represent the rotation curves of the halos under the maximum disk assumption. The light dash-dotted lines in both panels show the rotation curve of NGC 2403 smoothed to the same physical resolution as the UGC 128 observations. Credits to de Blok (1996).

The Tully-Fisher is an empirical relationship which links the rotation gas velocity (HI) of the disk of spiral galaxies to their luminosity. If the magnitude of the galaxy is dust-extinction corrected and the speed de-projected (regarding the inclination, by a factor cos (i)) the relation brings L $\propto V^4$. Figure 1.17 presents the Tully Fisher relation for HSB galaxies (solid line), points correspond to a sample of LSBG. Absolute magnitudes are computed in B band and velocities in km/s.

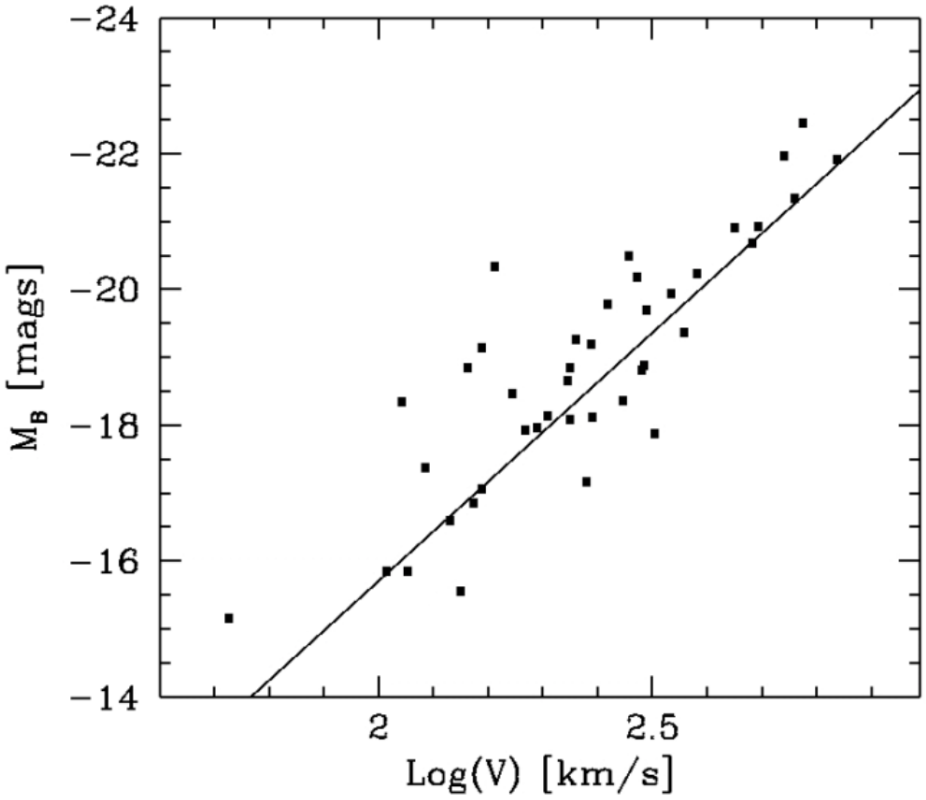

Figure 1.17: Tully Fisher relation for a sample of LSGB (points) compared to the relation defined by HSB galaxies (solid line). Credits to Scarpa.

It is evident that LSBGs follow the same Tully-fisher relation of HSB galaxies, but even though the dynamical masses are comparable to those of HSB galaxies, LSBGs are supposed to be embedded in more extended and less dense dark matter halos than HSB galaxy halos. The TF relation so far defined is well followed by brilliant spiral galaxies. As luminosity decreases, galaxies tend to deviate from the relationship, showing a higher speed than expected. This fact could be due to the significant presence of HI gas in faint galaxies. Definitely, from these rotation curves we can infer important properties on the abundance of gas and matter which forms LSBs objects [49].

1.1.4 Amount of gas of LSBGs

It is important to notice that when deriving values for the total masses of low surface brightness galaxies from rotation curves we are computing the lower limits. One of the characteristics that we can infer from these curves is that at virtually all radii, the gaseous component of LSBs is dynamically relevant and the dynamical mass to luminosity ratio (M/L), although difficult to obtain, is globally and locally two (or even three for drafts) times higher than that of normal galaxies of the same total luminosity and morphological type [15] [48] and it increases with decreasing surface brightness. The gas to mass fraction f_g of a galaxy is defined as

$$f_g = M_{gas}/[M_{gas} + M_{star}] \tag{1.1}$$

f_g for the most of LSB galaxies is high, meaning that they are gas-rich systems. Studies on 21 cm HI emission have revealed that f_g of LSBGs increase smoothly and sometimes approaches unity. There seems to be a strong correlation between f_g and the B-band surface brightness μ_B as shown in Figure 1.18 for a sample of galaxies with μ_B below 20 $mag/arcsec^2$. However, while the lack of HSB objects with high gas-mass fraction is real, LSB galaxies with low f_g can be missed due to selection effects.

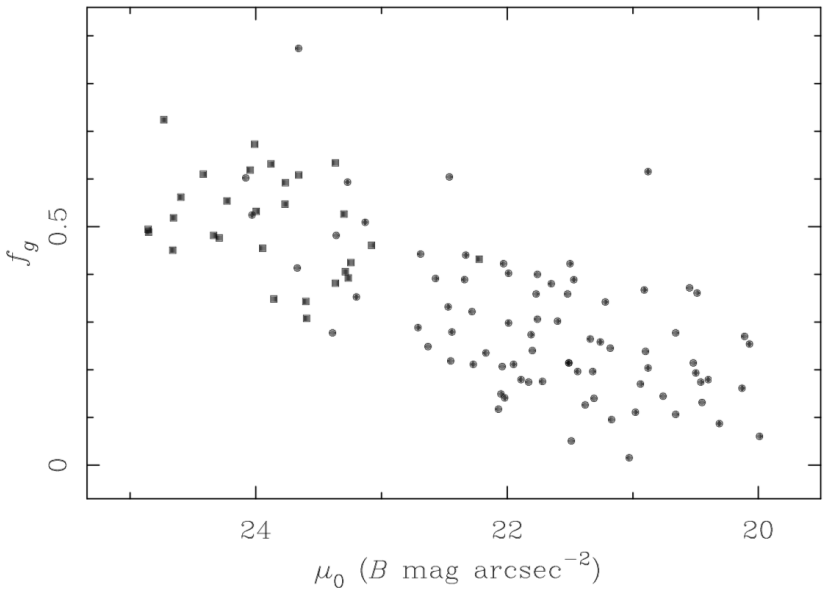

Figure 1.18: Gas to mass fraction as a function of surface brightness B band. Credits to McGaugh.

The main repository of the baryonic matter of these faint sources is the neutral hydrogen gas ($\sim 10^9 M_\odot$). Thanks to this huge quantity of gas, their 2D distribution of HI (and their rotation curves) can be derived from aperture-synthesis data and by using the VLA and WSRT radio arrays. The results of these efforts shows that the HI mass distribution of LSBGs is similar to the one of the normal galaxies in the Uppsala General Catalogue of Galaxies (Nilson 1973) but they have lower than average surface densities. Moreover, while low surface density HI disks changes by a factor 2, low surface brightness stellar disks vary for a factor 5. I mention as an example the HI surface density distribution for the low surface brightness galaxy disk of UGC 6614 (Data from Pickering

et al. (1997)) and its rotation velocity plotted in Figure 1.19 with respect to the radius.

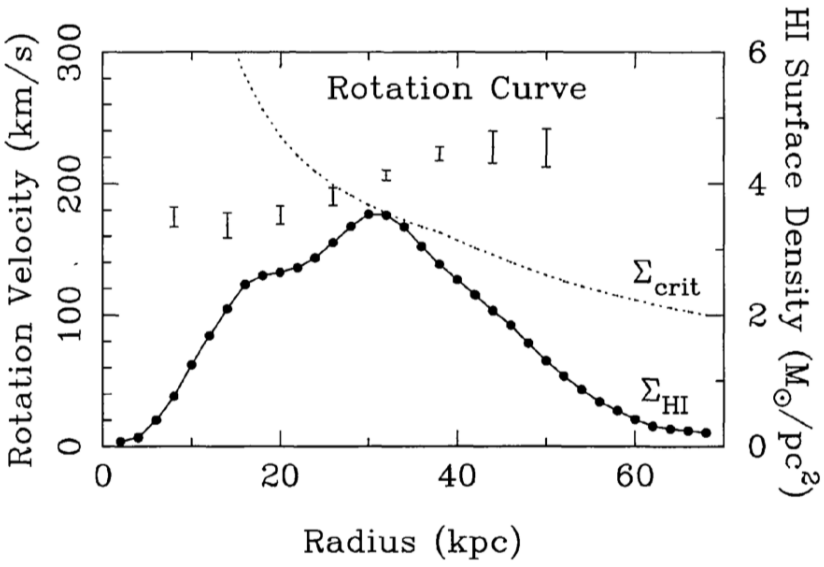

Figure 1.19: UGC 6614 HI surface density versus radius. Data from Pickering et al. (1997). Credits to Bothun.

The surface density of HI gas for UGC 6614 is, as happens for the majority of LSBGs, everywhere below the critical density and lower than in late type HSB galaxies. A small amount of star formation is reached at 30 kpc, but as long as the gas density is below the threshold for molecular cloud formation, the metal production is very low and so low surface brightness galaxies are very inefficient in converting gas into stars. Though observations have shown that late-type edge-on LSB spiral galaxies have $CO_{J=1-0}$,$CO_{J=2-1}$ emission, most LSB spirals have very little molecular gas compared to HSB spirals of the same mass. In addition, no dust emission has been detected neither with the Spitzer Space Telescope in the UV nor with the Infrared Array Camera making astronomers presume that LSBGs are dust-poor systems. The high M/L ratio leads to important consequences when estimating the amount of dark matter on which the galaxy resides. Moreover, the luminous baryonic matter does not determine the form of a low surface brightness galaxy rotation curve, no theoretical model fits this hypothesis, it is the dark matter content that dominates disks at almost all radii and contribute the most [48]. To demonstrate observations, the Newtonian theory of gravity must appeal dark matter as I will explain subsequently in next section.

1.1.5 Colors and metallicity

LSB galaxies have a bluer trend in the optical broad-bands and in the near-infrared (NIR) wavelength regime compared to the widely studied HSBGs which define the Hubble sequence. Their typical colors range from $U-B=-0.17\pm0.05$, $B-V=0.49\pm0.04$, and $V-I=0.89\pm0.04$ to $B-V=0.75\pm0.03$ and $V-R=0.53\pm0.02$ [35]. It is observed that with decreasing size and surface brightness of the central disk of low surface brightness galaxies, colors become even more blue. One of the more curious aspects of the color distributions of LSB samples (from McGaugh and Bothun (1994)) is shown in figure 1.20 which indicates that there is no correlation between integrated disk color and observed surface brightness. This is difficult to interpret, unexpectedly for the disc fading scenario that I will describe later, it seems to be a tendency to bluer colors while decreasing surface brightness but this appearance can be also due to selection effects.

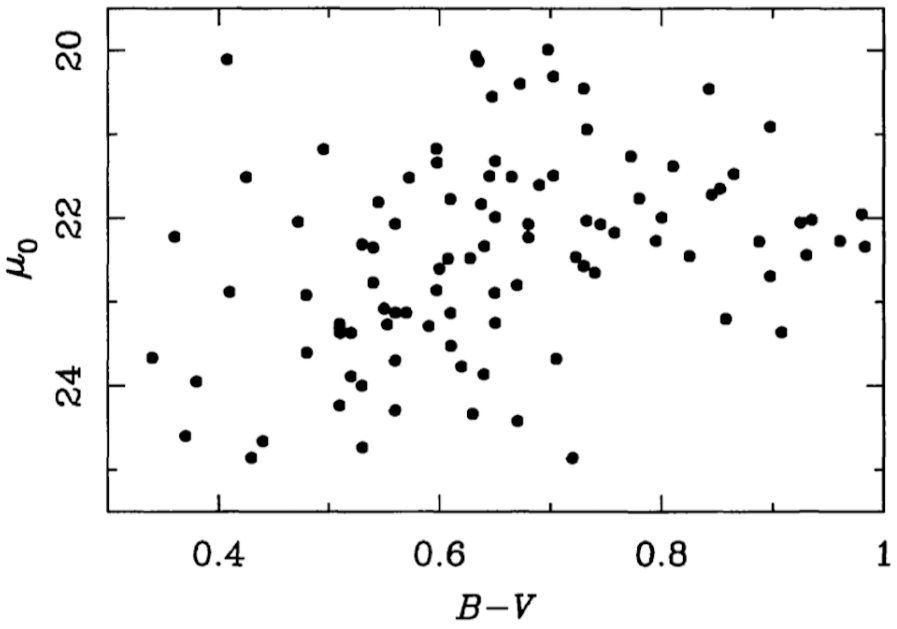

Figure 1.20: Un-correlation between surface brightness and colors. Sample of LSB galaxies from McGaugh 1994. Credits to Bothun.

The positions of LSB galaxies in the Hertzsprung-Russell diagram defined by their bluer $V-I$ colors suggest that they are low metallicity systems. One way to confirm this low abundance of metals is trough the analysis of the optical spectra of HII regions in LSB disk galaxies. Figure 1.21 shows the spectrum of one of the HII regions in UGC 1230, a low surface brightness galaxy where the bright emission lines are mainly due to oxygen and hydrogen. The emissions occur for the prohibits lines of $[OII]$ $\lambda3727$, $[NeIII]$ $\lambda3869$, $[OIII]$ $\lambda4363$, $[OIII]$ $\lambda4959$, $[OIII]$ $\lambda5007$, $[NII]$ $\lambda6548$, $[NII]$ $\lambda6583$, $[SII]$ $\lambda6717$, $[SII]$ $\lambda6731$ and for H_γ, H_β, He I ($\lambda5876$) and H_α.

Results show that LSBGs are metal poor, and they have a Z value ranging from 0.1 to one third the solar metallicity. One would expect correlation between central surface brightness of disks and HII regions abundances (metallicity) but it is not so obvious, there could be some trend but it is not well-defined as shown in Figure 1.22.

However, the primary cause of these bluer colors similar to the most metal-poor galactic globular

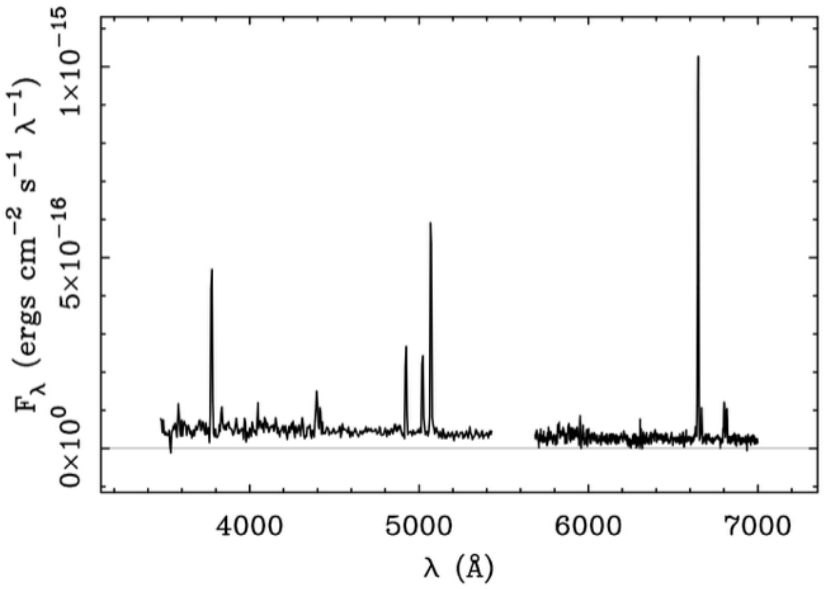

Figure 1.21: The spectrum of one of the HII regions in UGC 1230. Credits to McGaugh.

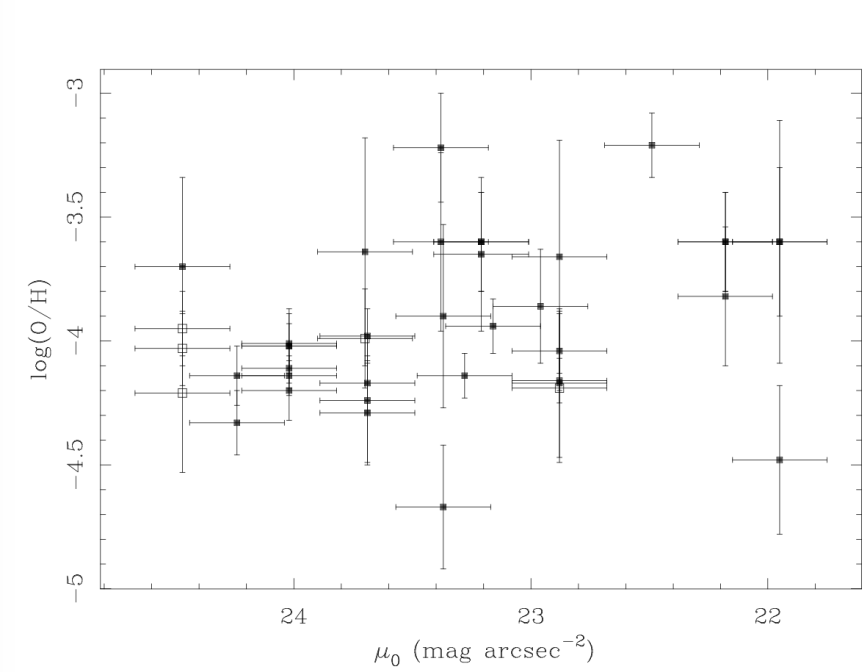

Figure 1.22: Oxygen abundances with respect to the surface brightness B-band. Credits to McGaugh.

clusters, should not be sought only in the low metallicity because there are even some observed old and metal-rich low surface brightness galaxies but, above all, in discerning of the star formation rate of the galaxy.

1.1.6 Star formation history and evolution

The star formation rate (SFR) is the number of stars that form in the infinitesimal mass interval [M, M + dM] in the time unit (usually measured in $M_{\odot}/years$):

$$SFR(M) = dN_{(M,t)}/dt \tag{1.2}$$

It is linked to a high number of physical parameters, as well as to environmental phenomena and conditions such as the amount of gas available, according to the infall model:

$$SFR = M_{gas}/t_s \tag{1.3}$$

where t_s is the star formation time scale. Moreover, it depends on the initial mass distribution of the stars (initial mass function IMF), a simple power law as a function of mass for values higher than a solar mass proposed by Salpeter (1955) and Scalo (1979):

$$\Phi(M) = dN(M)/dln(M) \tag{1.4}$$

To understand the mechanisms and timing of the formation and evolution of galaxies astronomers study the temporal evolution of the SFR of galaxies, the Star Formation History (SFH), an issue which is still open to investigations and hypotheses. Regarding the star formation history of LSB galaxies, there are few scenarios and theories that may apply, each one with its merits and shortcomings. One of these is the *disc-fading scenario* in which LSB galaxies are supposed to be the faded remnants of high surface brightness galaxies. This theory is disproved because a clear reddening with decreasing surface brightness is not observed. Similar to this scenario there is the *initial starburst with cutoff theory* discarded because the observed colors of LSB galaxies are less red than that ones predicted. The scenario of the *exponentially declining star formation rate* is not accurate, as a matter of fact any galaxy that have undergone an exponential SF history must have a large population of old stars but the colors of LSB galaxies are bluer that of HSBGs suggesting that there is a lack of this old population. For the same reason, also the hypothesis of constant SFR is not good. The most accurate scenario advance a low sporadic star formation rate in the past, the old population did not have enough time to develop and star formation has increased only recently. The most of the light coming from LSBGs originate from their young stellar population. Star formation histories of LSB galaxies are mainly done by using optical broad-band photometry, the measure of SFRs through Hα photometry, ultraviolet photometry and far-infrared photometry is not yet widespread. Studies based on the analysis of HII regions of LSBGs show that the emission equivalent widths of HII regions in LSBGs are lower than those in HSBGs, and their star formation rates per unit area in the past and nowadays is lower than that of HSBGs with similar sizes. The analysis conducted by the astrophysicist Van Zee in 2001 on a set of draft LSB galaxies shows that they have SFR even lower than 0.1 $M_{\odot}$ per year, which is an order of magnitude lower than in HSB Sc galaxies ($\sim 4\ M_{\odot}$). The star formation is usually experienced outside the molecular-cloud environment and the gas depletion is long with timescales of tens of Gyrs. In Figure 1.23 are presented the median age of HSB, LSB and UDG stellar populations colored blue, yellow and red respectively, with the Horizon AGN simulation. For UDGs the mean is 9 Gyr, 50% older than their

HSB counterparts.

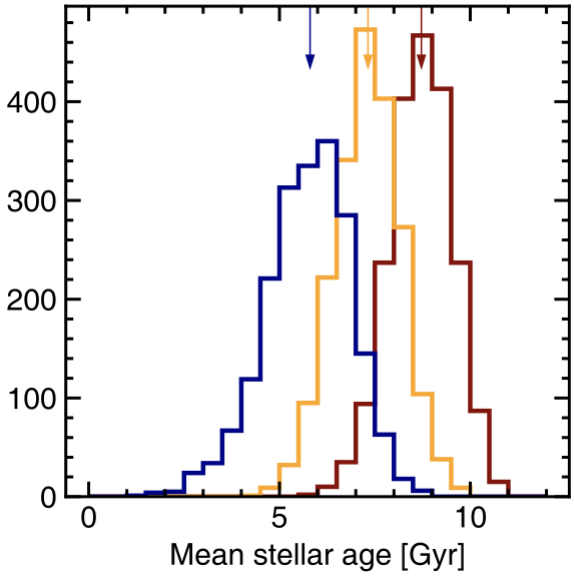

Figure 1.23: Mass-weighted mean stellar age of HSBGs (blue), LSBGs (yellow) and UDGs (red). Credits to McGaugh.

The large age differences between LSBGs and HSBGs indicate that the LSB nature of these systems must be partly driven by gas exhaustion at early epochs and consequently a more quiescent recent star history. This large timescale make astronomers suppose that many Gyrs ago LSB galaxies were in late-type HSB galaxies of comparable mass. But what about the environment? Is it important to define the evolution of galaxies? Most of LSBGs detected, analyzed and studied are located in the clusters of Virgo, Coma and Fornax but the majority of LSB galaxies (90%) is found in filaments instead of clusters when compared with HSB. Limited samples of UDGs were discovered in groups and field [50], most of late-type galaxies at fixed stellar mass are found in extremely isolation on scales $\leq$ 2 Mpc, dwelling in relatively void regions. Only LSB giants are not located in strict isolation, but they have smaller neighbors than normal LSB galaxies. Figure 1.24 illustrate that for a given stellar mass, at z = 0, the frequency of LSBGs is higher in denser environments. The LSB peak progressively dominates as we move to higher density environments.

Conversely, the bottom-right panel of Figure 1.24 show that many UDGs occur in regions of much lower density although they appear to exist preferentially in regions of high number density. HSBGs appear to be essentially uniformly distributed. This fact is remarked in Figure 1.25 on scales of Mega parsecs where higher densities are indicated with lighter colors. Studies report that typically, galaxies of group and cluster environments are found in halos with masses $10^{12.5} M_{\odot} \leq M_{halo} \leq 10^{13.5} M_{\odot}$ and $M_{halo} \geq 10^{13.5} M_{\odot}$ respectively. Most low density galaxies (field) are isolated with typical halo masses of $\sim 10^{12}$ $M_{\odot}$ for satellites [47]. We are still not able to explain with a single evolutionary path which are the mechanisms capable of producing low surface brightness objects. Few theories have been proposed to explain their formation across different environments but the exact way is still debated. Are them gas outflows due to supernova (SN) feedback? Ram pressure? Strong tidal fields? Mergers? Blue colors, low metallicity, large gas mass fraction and the small

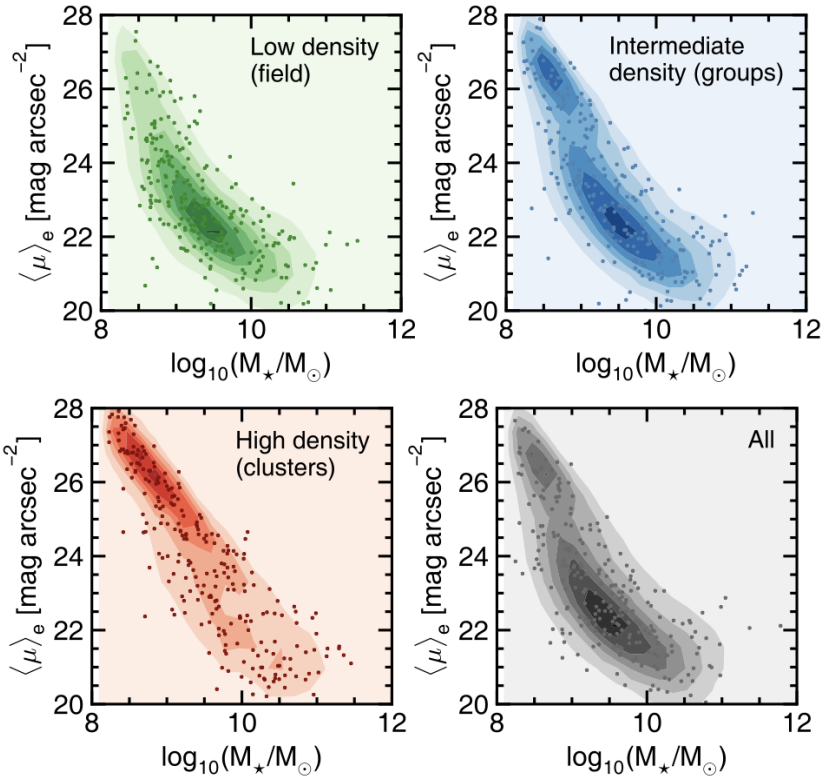

Figure 1.24: Number density of galaxies as a function of effective surface-brightness and stellar mass. The bottom right panel shows the same for all galaxies in the sample from G. Martin et al.

amounts of star formation suggest a slow evolution driven by ram-pressure stripping, late formation epoch and youth. As recently confirmed, LSBGs are statistically less evolved than gas poor galaxies, and they may be the most un-evolved objects in the universe.

Undoubtedly, in lower-density environments, gas rich galaxies are subject to few tidal interactions with other galaxies, but this kind of heating is supposed to be able to produce the large sizes and low star-forming gas fractions of low and intermediate redshifts UDGs even regardless of the environment, since UDGs are found in field, clusters and groups. Moreover, there are some faint galaxies, both in high and low density environments, that are observed to be experiencing tidal effects like the ones in the Perseus cluster core [37]. To analyze this effect on LSBGs astronomers uses the perturbation index:

$$PI = \int_{z=3}^{z} \sum_{i} (M_i/M_{gal})(R_{eff}/D_i)^3 dt/Gyr \tag{1.5}$$

that is the cumulative contribution of all nearby galaxies of the studied galaxy within 3 Mpc (and between z = 3 and the redshift in question) which contribute to the environmental tidal field. PI depends on the stellar mass of the galaxy in question (M_{gal}), the stellar mass of the perturbing galaxy (M_i), the effective radius (R_{eff}) and the distance from the perturbing galaxy(D_i). We can see in Figure 1.26 that the median PI values in the LSBG and HSBG populations is similar at high redshifts, but they tend to diverge with time, in case of UDGs the PI value turn to be larger than that for the HSBGs (2 orders of magnitude greater). However, we observe a decreasing number

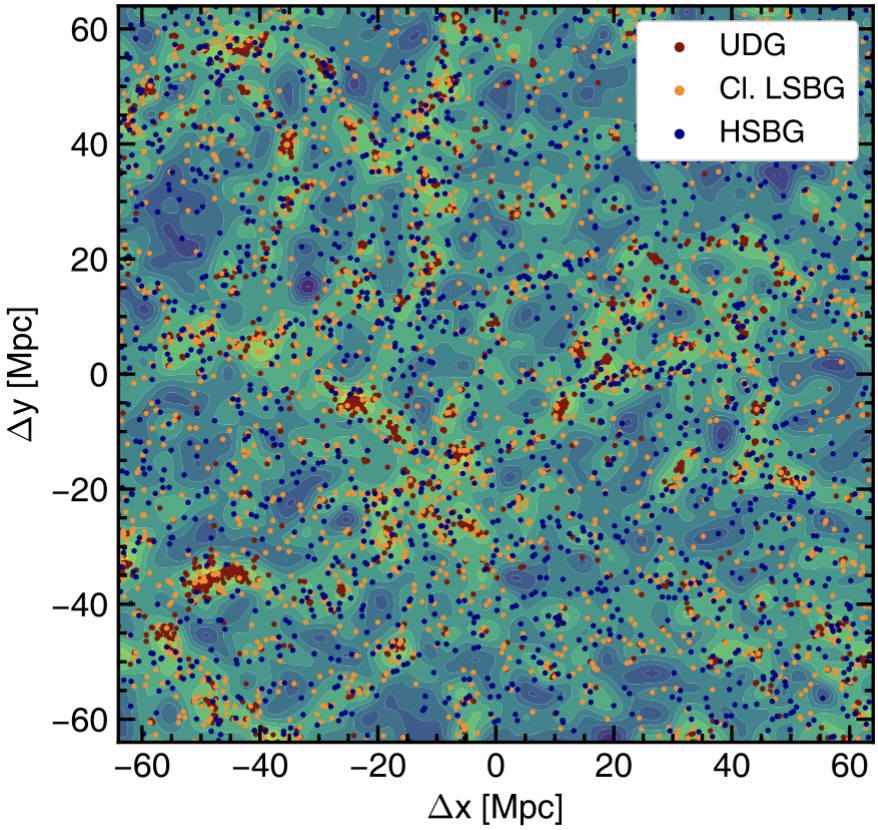

Figure 1.25: The spatial distribution of the UDG, Cl. LSBG, and HSBG populations within the cosmic web. Credits to G. Martin et al.(2019).

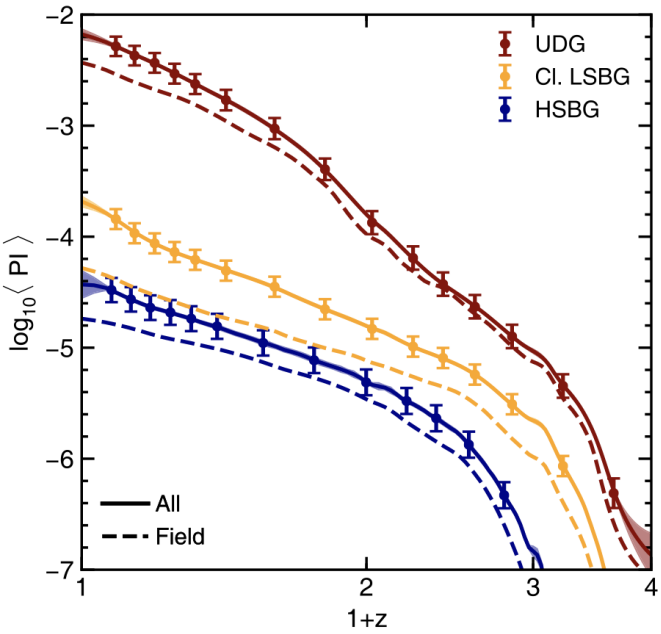

Figure 1.26: Median perturbation index PI as function of redshift. G. Martin et al. (2019).

density of faint LSB galaxy candidates in the cores of galaxy clusters as discussed in the analysis of Wittmann(2017); the ultra diffuse galaxies with larger sizes in the Perseus cluster core [37] cannot

survive the strong tidal forces and this disruption of LSB galaxies close to the cluster centre is also predicted by numerical simulations of Yozin & Bekki (2015). Ram-pressure stripping indeed, is the most significant mechanism may be capable of producing LSBGs. A large fraction of local UDGs are satellites, meaning that their haloes are identified as sub-structures of a more massive halo, and they are found in high gas density regions. They experience ram pressure due to the host halo they are embedded in and, especially in clusters, ram pressure removes gas from in-falling UDG progenitors, starting around z = 1. The result is that UDGs undergo higher ram pressure than that of classical LSBGs and HSBGs. The curves that fits the evolution of the ram pressure parameter:

$$P_{ram} = \int_{z=3}^{z} \rho_{IGM} \nu_{gal}^2 dt/Gyr \tag{1.6}$$

where ρ_{IGM} is the mean gas density of the surrounding medium and ν_{gal} is the velocity of the galaxy relative to the bulk velocity of the surrounding medium [37] as a function of redshift felt by UDG, HSB and LSB galaxies are presented in Figure 1.27 with blu, yellow and red colors. It is important to note here that UDGs experience more ram pressure than that by Cl. LSBGs and HSBGs at all redshift, even if they are located only in the field. This trend can be due to the fact that a larger fraction of local UDGs are satellites.

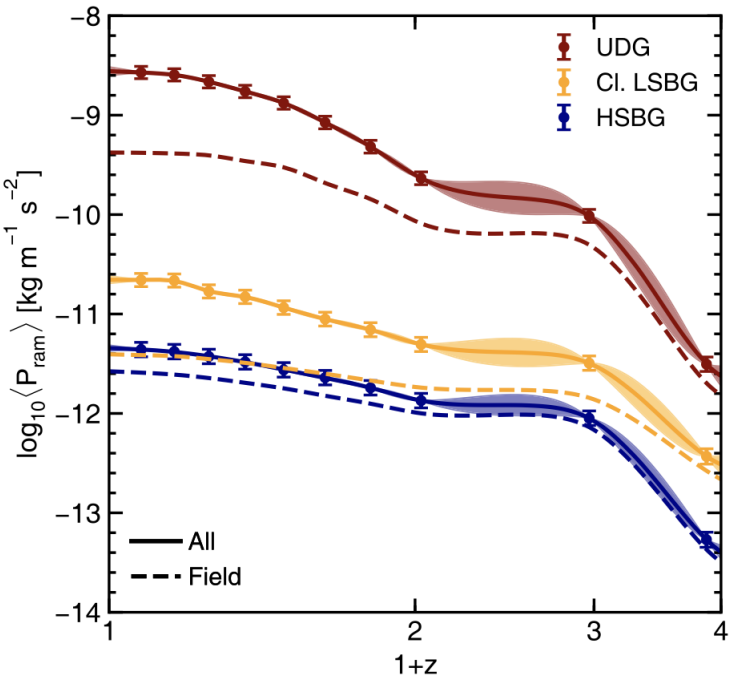

Figure 1.27: Cumulative ram pressure felt by galaxies as function of redshift. G. Martin et al. 2019.

Figure 1.28 depicted the redshift evolution of the median gas fraction:

$$M_{gas,SF}/(M_{gas,SF} + M_\star) \tag{1.7}$$

for UDGs, HSB and LSB galaxies. From this model we can evince that UDGs experience more rapid star formation between z = 3 and z = 1 and HSBGs and LSBGs originate from populations with almost identical gas fractions and effective radii at z = 3. The subsequent Figure 1.29 illustrates

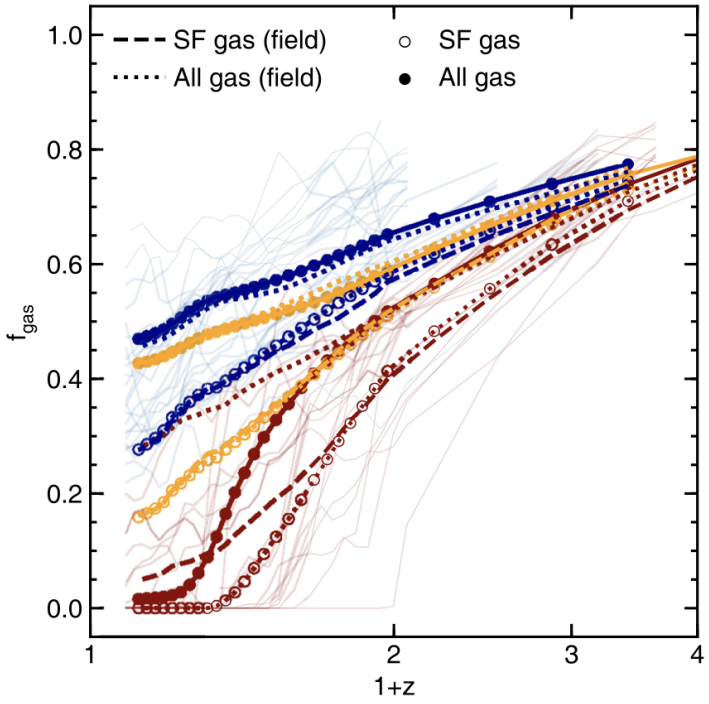

Figure 1.28: The redshift evolution of the median gas fraction. G. Martin et al. 2019.

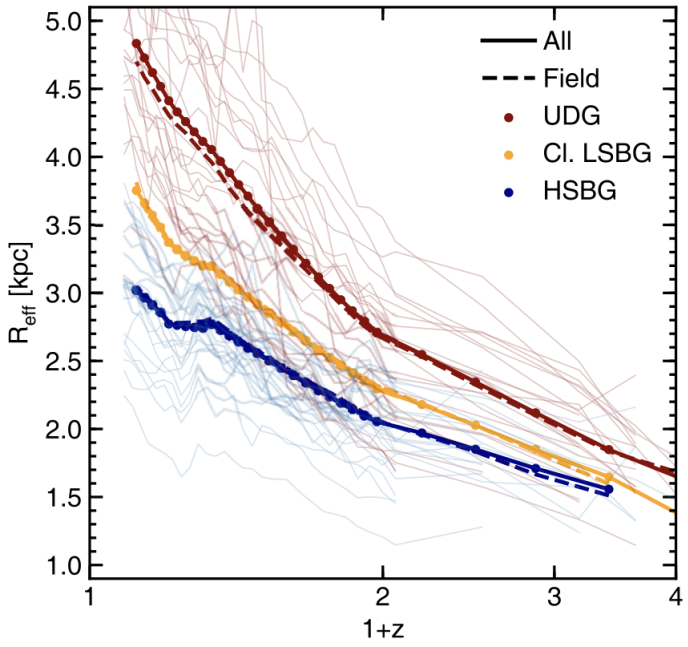

Figure 1.29: The redshift evolution of effective radii. G. Martin et al. 2019.

how the radii of different types of galaxies changes with time. UDG radii and UDG gas fractions increase smoothly and due to this we can conjure that LSBGs are not formed in single violent events, but they are supposed to evolve from gradual collapse. HSB, LSB and ultra diffuse galaxies seem to have had similar radii at high redshift, and then they started to diverge relatively recently.

Thought LSBGs evolve from the same progenitor population as HSBGs at high redshift ($z \sim 3$),

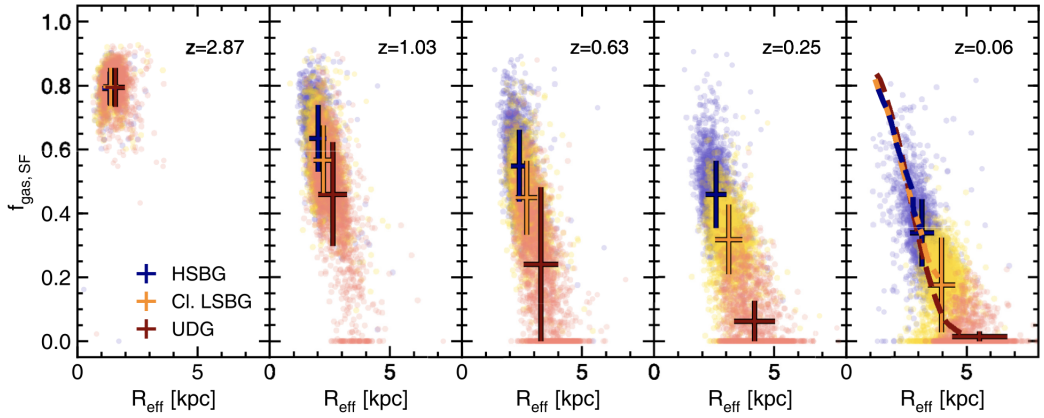

Figure 1.30: Star-forming gas fraction radius at different redshifts. Dashed and dotted lines without points show the evolution of f_gas for total gas and star-forming gas respectively for field galaxies only. Pale red and blue lines show tracks for the effective radii and star-forming gas fractions of a random sample of individual UDGs and HSBGs. Credits to Martin et al. (2019).

they diverge significantly around $z \sim 2$ and the evolution especially at $z \leq 1$ of LSBGs (and UDGs in particular) is very rapid as remarked in Figure 1.30. Another mechanism that could drive the evolution of these faint objects is supernovae feedback. The cosmological hydrodynamical simulation Horizon-AGN leads to define [47] that for redshifts between 3 and 1, low surface brightness galaxies and UDGs in particular are affected by high levels of SN feedback, the SN energy release peaks between z = 2 and z = 1 and the slope of the gas density profile is made shallower towards z=0. Ultra diffuse galaxies at high redshift have a star-forming gas fraction ≥ 0.4 and then declines, indicating that the supernovae feedback could be the initial trigger for the divergence of UDGs from the rest of the galaxy population and it is not strong enough to carry out star formation leaving these faint systems more incline to tidal processes over cosmic time (see Figure 1.30).

1.2 Cosmological significance

A number of cosmological questions can find an answer in the discovery of a substantial population of LSB galaxies at z = 0. LSB galaxies play a key role in cosmology to fill those discrepancies that are not completely clear yet, and they are very important to understand why theoretical expectations do not always agree with real observations. These objects are affected to observational limitations and, especially for this, some issues concerning them are still poorly supported by scientific data and not very developed in depth. On the other hand, LSB galaxies are well studied with regard to the distribution of dark matter since they are believed to be dominated even in the central regions. I will describe in this chapter the main points.

1.2.1 Quasar Absorption mechanism

The optical spectra of Quasars shows many absorption lines which are believed to be due to gas and galaxies along the line of sight. The most interesting systems are those that show the Mg II resonance doublet (λ2796, λ2803) since these lines can be detected in the optical region of the spectrum for quite low-redshift absorbers with direct imaging. Figure 1.31 reports a typical quasar spectra, the PG 1206+459 one. The narrowness of those QSO lines depends on the column density of this material and, since the density is low and a huge cross section is needed, it is possible to invoke large galaxy halos (LGH) or low surface brightness galaxies as absorbers. For many years this mechanism was believed to be due to LGH but some well-known difficulties such as the searching for metal-line systems in QSOs near bright galaxies that usually fails, the lack of their observed evolution compared to their required evolution and the difficult search for such objects in nearby clusters, nowadays astronomers conjecture on LSBGs to find answers on the origin of this absorption process. Taking into account numerous LSBGs as absorbers we can overcome LGH hypothesis anomalies, since the actual QSO-bright galaxy separations and halo sizes discrepancy becomes irrelevant and the total population cross-section is enough to explain the observed number of quasars. Therefore, we no longer need huge halo sizes. We cannot yet prove this hypothesis, but on the other hand it is certainly not possible to discard it only on the basis of present observations since they are still not exhaustive [51].

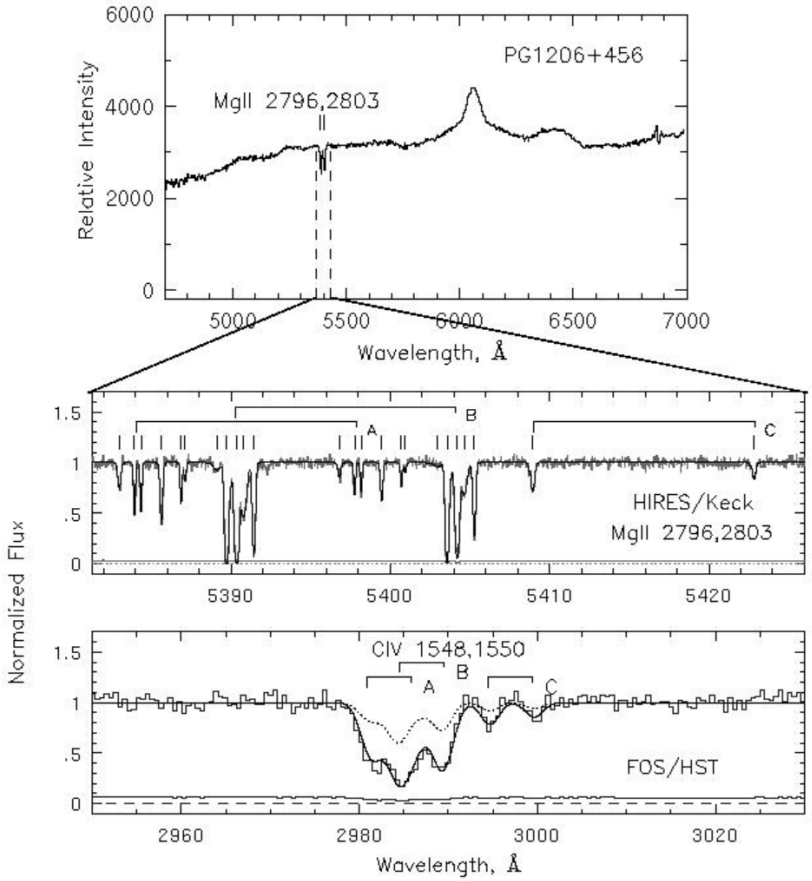

Figure 1.31: PG 1206+459 spectra. Credits to Charlton.

1.2.2 ExtraGalactic Background Light correlation

LSB galaxies, since weakly clustered, are correlated with the ExtraGalactic Background Light. In principle, they could help to place limits on the capable EBL intensity or even produce a rise of it by a factor 5 than the standard value of $\sim 10^9$ erg $cm^{-2}s^{-1}sr^{-1}A^{-1}$). LSB add to the level of the EBL without increasing the amplitude of the fluctuations and it permits constraining new galaxy evolution models, discriminating between cosmological models and galaxy counts. However not a lot of detailed research has been done regarding this issue [52] [53].

1.2.3 Dark matter content

One of the gaps between theories and observations is that the Cold Dark Matter model, thought satisfactorily reproduces the observations of the Big Bang cosmology, explaining in particular the cosmic background radiation (CMB), the large-scale structure of the universe and supernovae that indicate an accelerated expanding universe, predicts far too many dark halos to match the cataloged galaxy population [54] leading to questioning: Have many dark halos failed to form galaxies, or have they formed galaxies that have so far escaped detection? Figure 1.32 displays the dark matter fractions of HSBGs in blue, LSBGs in yellow and UDGs in red computed with analytical simulations on samples of galaxies. It suggests that very high-DM-fraction UDGs are extremely uncommon, and there are some that may have very low DM fractions [55].

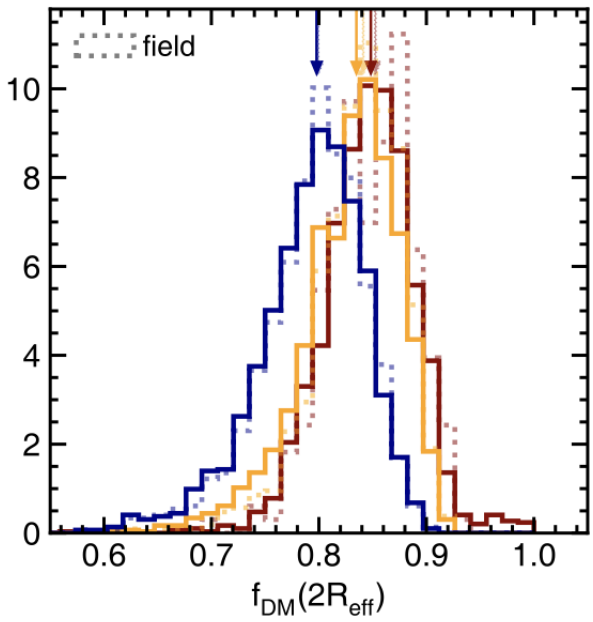

Figure 1.32: Dark matter fractions for a sample of HSB, LSB and ultra diffuse galaxies in blu, yellow and red respectively. The amount of gas fraction is computed inside 2 effective radius. Credits to Martin et al 2009.

However, astronomers agree that LSBGs are more dark matter dominated than their high surface brightness counterparts, so they are fundamental to understand the relative abundance of light and matter in the Universe. The importance of DM that thickens in LSB objects can be derived from the Tully- Fisher (TF) relation: L $(\Sigma_0 \cdot M/L^2) \propto V^4$ where M/L is measured within a fixed number of scale lengths, and Σ_0 is the central surface brightness μ_0 expressed in linear units. As said previously, the LSB galaxies do oddly follow the same TF relation as HSB galaxies that suggests a link between evolution rate and DM dominance. Figure 1.33 shows on the left the TF relation for HSB and LSB galaxies where the diagonal lines are TF relations for the indicated values of surface brightness if all galaxies had identical M/L. On the right side of the image the M_{HI}/L_B and M_{dyn}/L_B within 4h versus μ_0 is plotted. We can easily observe that there exist a coupling between μ_0 of a galaxy and its M/L ratio and if all galaxies had similar total M/L ratios, one would expect parallel TF relations for each surface brightness. Nevertheless, as it is evidently, LSB galaxies must have higher M/L values than HSB galaxies, and they must be more DM dominated.

The nature of dark matter is one of the most important issues in astrophysics since it is supposed to accounts for $\sim$ 25 % of the energy density of the Universe. Dark matter has not been identified yet. We are not able to establish what dark matter actually is composed of and none of the current candidates seems to be the right one. However, one of the nominees are Weakly Interacting Massive Particles (WIMPs) that can be produced in thermal equilibrium through interactions with standard model particles in the early Universe. To unveil the nature of DM astronomers estimate the total cross-section for their annihilation processes; when γ rays (20 MeV to 1 TeV) are produced in such processes, they can be detected by detectors like the Fermi Large Area Telescope (Fermi-LAT) on board the Fermi Gamma-Ray Space Telescope. Since the γ-ray emission is rare we have to search for it in high dark matter concentration regions of the universe, such as the Galactic Center or dwarf spheroidal galaxies. LSBGs are known to have very large dark matter contents and

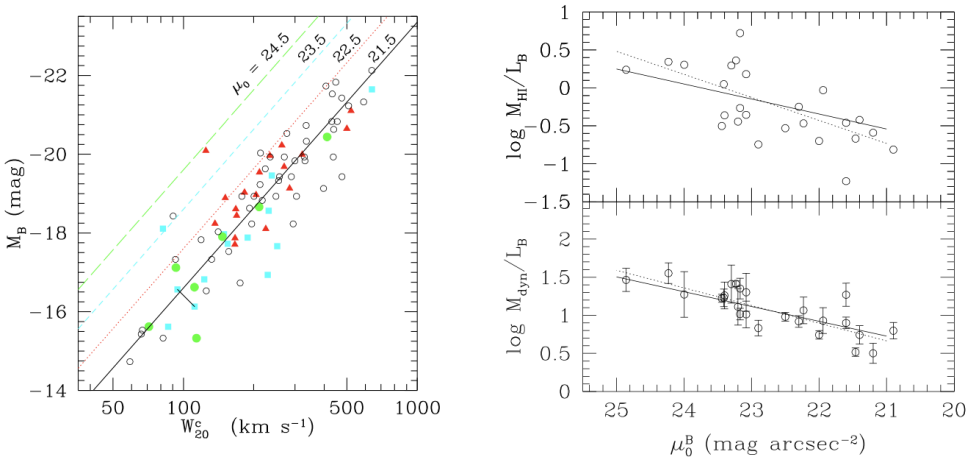

Figure 1.33: Left: TF relation for HSB and LSB galaxies. Right: M_{HI}/L_B and M_{dyn}/L_Bwithin 4h versus μ_0. Dotted lines as least-squares fits. Full lines are predictions from the TF relation.

be less contaminated by extragalactic γ-ray sources (blazars) compared to star forming galaxies, therefore low surface brightness galaxies can be also novel targets for the indirect detection of dark matter annihilation signals. The advantages of using LSBGs for constraining DM properties over other possible targets are: First, they are expected to have a low level of unresolved point source contamination within. Secondly, they are typically 10 times more massive than Milky Way draft spheroidal and, lastly, the expected number of LSBGs will be very large (much larger than that of dSphs). LSB galaxies are the best objects for tracing the mass profile of the dominant dark matter component since in other galaxy types, the stellar mass can provide a non-negligible contribution to the rotation velocity at observed radii.

1.2.4 Light and Matter in the Universe

Regarding the Light and Matter content, a great success of standard cosmology is that the prediction of primordial nucleosynthesis agrees with the observed abundances of light elements in the Universe but a careful accounting of the visible material in and between galaxies shows that the Big Bang model falls in deducting the amount of baryonic stuff. As a matter of fact for nucleon densities between $2.8 \cdot 10^{10}$ and $4.0 \cdot 10^{10}$, simulations predict a baryon density parameter to be ~ 0.01 [56] [57]. Observations indeed imply baryon density parameter ≥ 0.1, very difficult to understand if the standard scenario of a flat universe is correct. A similar discrepancy is found in the integrated luminosity density: Studies carried out with the APM survey shows that late-type LSB galaxies have $3 \pm 0.5 \cdot 10^7\ h_{100} L_{sun} Mpc^{-3}$ exceeding the luminous density of late type irregulars found by Marzke et al. (1994a), and being less than one third of the luminous density for all morphological types found by all investigators. Moreover, if we consider the total baryonic mass M of the galaxy (which therefore also includes the gas present in it) and its velocity dispersion we find a contradiction in the Baryonic Tully-Fisher relation; while theories provide M $\propto V^4$, the dark matter model assumption jointly with observations leads to M $\propto V^3$.

1.2.5 Large-Scale Structure (LSS)

Figure 1.36 presents the spatial distribution of galaxies with increasing redshift. When located in the cluster environment, LSB galaxies are usually near the edge of the galaxy distribution.

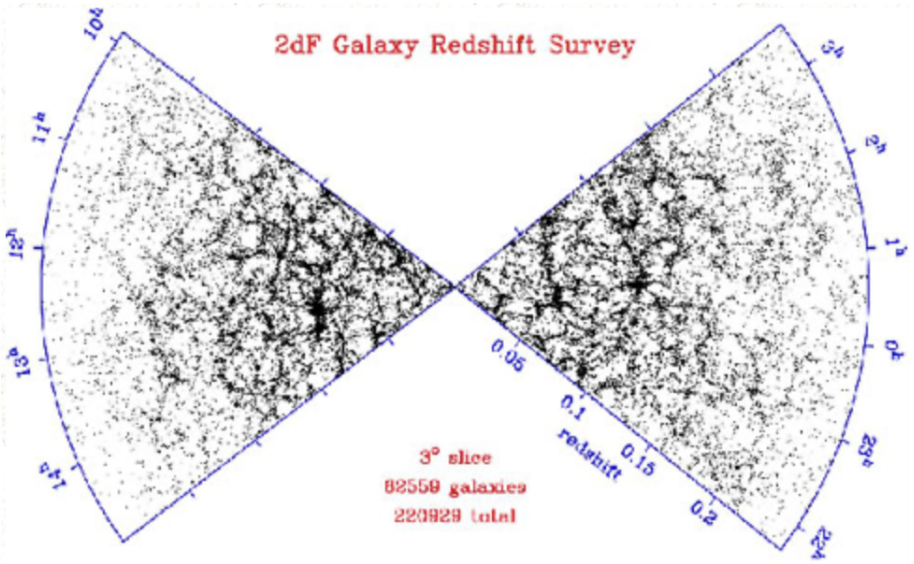

Figure 1.34: Spatial distribution of galaxies.

Though we have still less datas on LSB galaxies, the analysis conducted on the clustering properties of LSB disk galaxies in the CFA redshift survey lead few commonly accepted insights [58]. One of this is that LSB galaxies generally avoid virialized regions, and they are not found in large scale voids. Even if LSB galaxies trace the identical structures as HSB galaxies on scales $\geq 5\ h_{100}^{-1}$ Mpc, they are less clustered on scales $\leq 2\ h_{100}^{-1}$ Mpc. Indeed, LSB disk are usually isolated due to a significant deficit of companions within a projected distance of $0.5\ h_{100}^{-1}$ Mpc. The more reliable scenario predicts that LSBGs evolution is affected by this isolation since they have experienced fewer tidal interactions with nearby galaxies over a Hubble time. Nevertheless, tidal encounters are effective at driving global star formation and without them LSB galaxies would continue to evolve slowly and passively. The environment may play a less important role maybe only concerning the evolution of bulge-less LSB galaxies since the stellar populations of bulge-less LSB galaxies in low density regions are similar to those of bulge-less LSB galaxies in high-density regions. Accordingly, astronomers agree that the local galaxy density points the limits on the values of surface brightness of galaxies, and they advance a scenario where LSB galaxies are fair tracers of the mass distribution on large scales (better that the HSB counterpart).

1.2.6 The Faint End Slope of the Galaxies' Luminosity Function

Low surface brightness galaxies represent a significant fraction of objects at the faint end of the luminosity function and dominate the number density of galaxies at the present day. The number of galaxies per unit of volume with a given brightness interval is supplied by defining a physical quantity called luminosity function $\Phi(L)$. The function which approximates data is called Schechter's luminosity function:

$$\Phi(L)dL = \phi_{star}(L/L_{star})^{\alpha}exp(-L/L_{star})dL_{star} \tag{1.8}$$

where ϕ_{star} is the number of galaxies per Mpc. Figure 1.35 illustrate the space density of galaxies as a function of their absolute magnitude B band. The Schechter's luminosity function is painted red and it is clear that high luminosity galaxies stand in a smaller region than their faint counterpart which is uniformly distributed in the Universe.

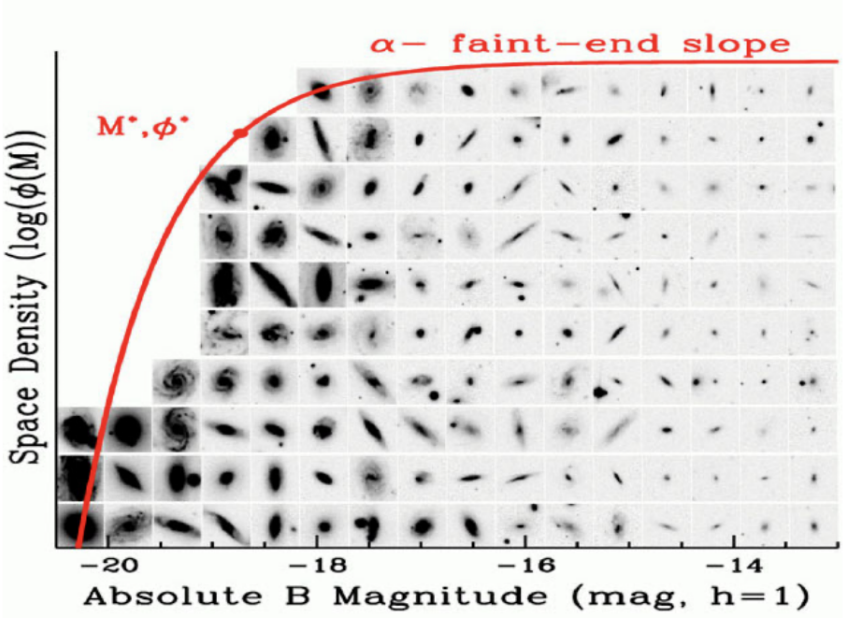

Figure 1.35: Space density of galaxies as a function of the B band magnitude. Credits to Simon Driver.

The α parameter of the Schechter luminosity function appears to have different values, it is uncertain and it may evolve with time. To confirm this, recent surveys have produced a variety of different values of α, ranging from -1.25 for HSBGs to -1.9 for low mass irregular galaxies. The galaxy luminosity function in the past was incorrect since galaxies are selected both on surface brightness and luminosity. Forgetting about this selection effect, a lot of large scale length galaxies now detected with the Malin method where missed, on the contrary LSBGs must play an interesting role to explain these different values. Taking properly into account these "missing galaxies" there is a significant increase in the faint end slope of the luminosity function. After these corrections, the Virgo and Fornax cluster dwarfs yield $\alpha = -1.55 \pm 0.05$. Figure 1.36 highlights that the slope of the luminosity function of SDSS galaxies in r-band changes with the surface brightness value. The curves are ranging from high to low surface brightness. It seems that low surface brightness galaxies do not make a huge contribution to the luminosity density of the universe. The faint end slope steepens but there is nothing that can prove which is the cause, astronomers can only

speculate that LSB galaxies dominate in clusters, and they might represent the results of a phase of intense baryonic blowout at higher redshifts. We will have to wait for deep-wide surveys such as LSST or EUCLID in order to get significant samples of LSBGs and UDGs to build a more accurate luminosity function.

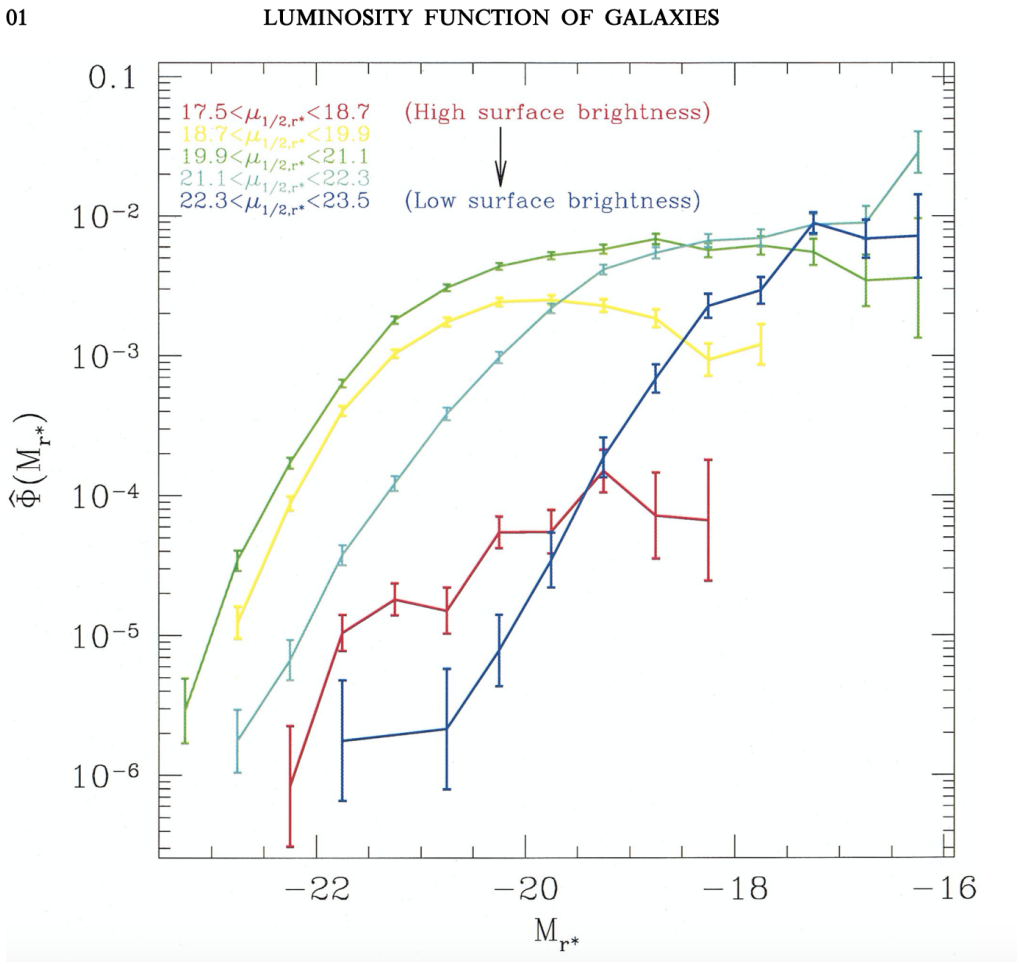

Figure 1.36: Luminosity function of SDSS galaxies in the r* band in units of galaxies per $h^{-3}Mpc^3$ per unit magnitude. Credits to Blanton.

1.2.7 The origin of UDGs

Another open astronomical issue regards the origin of the subset of ultra diffuse galaxies. There is no one unique channel since UDGs are ubiquitously distributed from the cores of galaxy clusters to the surrounding large-scale filaments, ranging from low to more high metallicity and different ages. Numerical simulations are one of the best approaches to exploring UDGs and nowadays two main mechanisms have been proposed. The first one supposes that UDGs are failed galaxies, since red UDGs in high density environments lost their gas content after forming their first few generations of stars at high redshift. To prove this scenario, Van Dokkum (2016) using stellar kinematics from spectroscopy and Toloba in 2018 using the technique of specific frequency of globular clusters computed respectively the virial mass of the faint galaxy DF 44 in Coma cluster ($M_{200} \sim 10^{12} M_{\odot}$) and the dark matter halo masses of VLSB-B and VCC615 galaxies in the Virgo cluster ($\sim 10^{12} M_{\odot}$). Unfortunately these results are unexpected from prediction of sub-halo abundance matching (SHAM) in which galaxy formation efficiency reaches its maximum at this halo mass value. Yozin & Bekki (2015) conducted the first self-consistent hydrodynamical simulations on ultra-diffuse galaxies in the Coma cluster to demonstrate that the red UDGs ($g - r \sim 0.8$) are accreted into the cluster at z $\sim$ 2 (depending on the assumed metallicity), and then efficiently quenched by ram pressure stripping in an over-dense environment (a late infall and a passive fading [59]). By artificially stopping star formation in a galaxy at a certain redshift and passively evolving its stellar population to z = 0, Hopkins showed that the quenching processes can reproduce the observed properties of UDGs in the Coma cluster. The second theory hypothesize that ultra diffuse galaxies are genuine dwarfs whose extended sizes are driven by their high spins. Boylan-Kolchin in 2009 presented an N-body simulation of dark matter evolution in the concordance Λ cold dark matter, the Millennium-II Simulation (MS-II) and three years after, he uses the Phoenix simulation to show that UDGs are dwarf galaxies with M $\sim 10^{12}$ with spatially extended sizes due to the combination of the late formation time and high spins of their host haloes [60]. Also, the Auriga cosmological Magneto-hydrodynamics simulations support the high-spin origin of field UDGs inferred from semi-analytical models. A new idea was proposed when the NIHAO simulations on isolated galaxies, were used to show that UDGs, which live in dwarf-sized dark matter halos with typical spins, originate from supernovae feedback driving gas outflows. Astronomers must agree that UDGs have multiple formation channels, and we need to investigate more on ages, metallicities, HI curves and use all of our effort to answer these unsolved questions.

1.2.8 Cusp/core problem

There seems to be a contradiction between lensing statistics and low surface brightness galaxies' rotation curves. LSB galaxies contain a greater quantity of dark matter than the HSB galaxies, and they have different rotation curves that steepen near the galactic center, as if within these galaxies, there is no luminous matter. Figure 1.37 point out a typical example of rotation curve for a faint galaxy in the UGC catalogue where velocity data come from different methods and techniques, including radio synthesis observations of the 21 cm spin flip transition of atomic hydrogen, and the n=3 to n=2 Balmer transition (Hα).

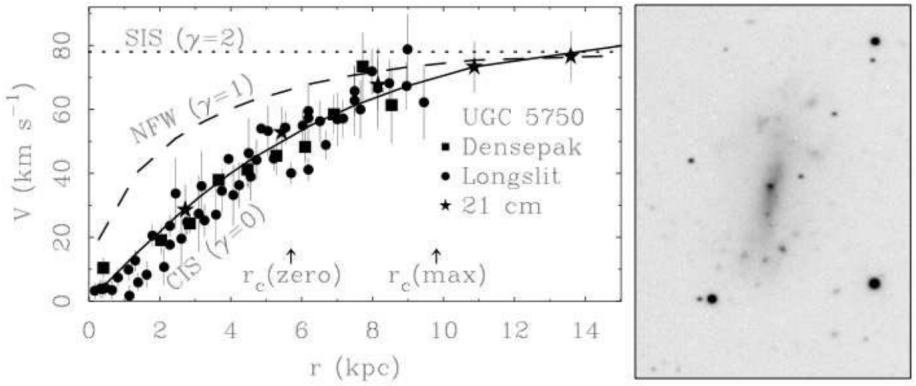

Figure 1.37: Rotation curve of UGC 5750. Navarro-Frenk-White profile and cored isothermal sphere as dotted and continuous lines. Credits to McGaugh (2008).

It is clear that nor the Navarro-Frenk-White (NFW) neither the singular isothermal sphere profile used to model galaxy and galaxy clusters do not correctly interpolate this rotation curve. The NFW model and the standard cosmology, which predicts that the universe is dominated by dark energy (Λ) and cold dark matter CDM, are correct on large scales, but they fail on smaller ones. As a matter of fact, observations on rotational curves for dark matter dominated low surface brightness galaxies imply a flat central core for galactic dark matter halos, theories and simulations instead predict a cuspy density profile at the center. This is the cusp/core problem which can find an explanation in stellar feedback or strong gravitational lensing. Stellar feedback can drive turbulent gas motion that erases the initial cusp which subsequently become a soft core. This model should apply to all masses of galaxies, but nowadays we have observed it to occur only with dwarfs. Gravitational lensing is very strong to prove the existence of dark matter and it depends on the slope γ of the central mass density profile. A better fit to LSB galaxies' dark matter halos down to small radii is the cored isothermal sphere (CIS). Anyway the CIS is a spherical model and it is correct to explain gravitational lensing only in clusters [61]. The question remains still debated.

Chapter 2

HiPERCAM pipeline

2.1 Data acquisition

Figure 2.1: GTC Canarias at La Palma. Credits to Daniel Lopez.

The observations of the UDG galaxy were carried out with the Gran Telescopio de Canarias (GTC) presented in Figures 2.1 and 2.2, it is a reflecting telescope with a primary mirror of 10.4 meters placed on the island of La Palma, in the Canary Islands, at an altitude of 2267 meters.

To obtain the optical raw images we used the quintuple-beam imager HiPERCAM camera (Figure 2.3) during 2.25h on source and with a requested spatial resolution of 0.6″ in the r-band. Figure 2.5 shows the ray-trace through the HiPERCAM optics; using four dichroic beamsplitters the light

Figure 2.2: GTC mirror architecture. Credits to Raab.

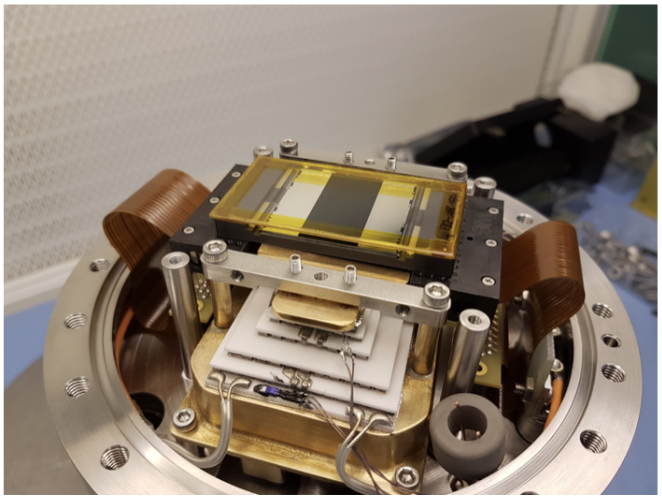

Figure 2.3: HiPERCAM detector and camera. Credits to Dhillon et al. 2016.

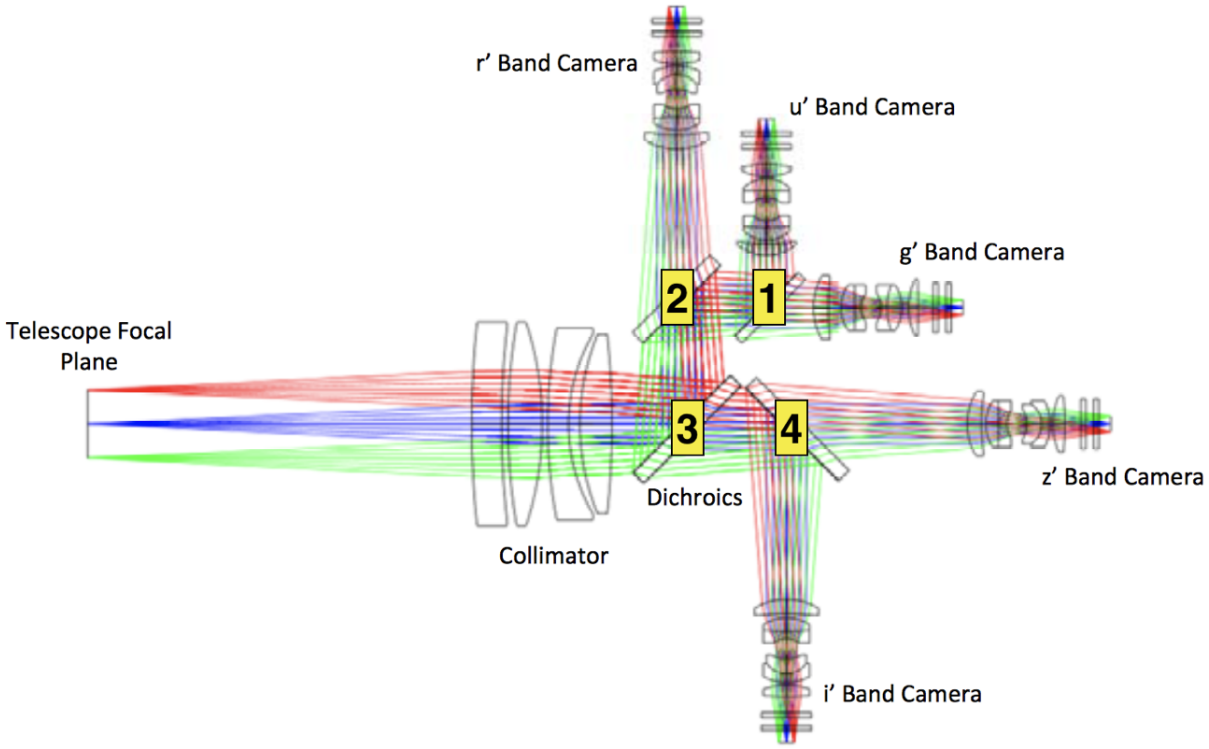

Figure 2.4: HiPERCAM optics. The four dichroic beamsplitters numbered in ascending order of the wavelength of the cut point and five beams set up. Credits to Dhillon et al. 2016.

coming from the telescope is first collimated and then split into five beams. The five HiPERCAM camera CCDs have 2048 x 2048 pixels with a pixel size of 15 microns. This structure gives on GTC a platescale of 0.081″/pixel and a total effective Field Of View of 2.8′ x 1.4′ (3.1′ diagonal). The raw images were obtained during two consecutive nights of observations using all 5 CCD's of the camera simultaneously (u′, g′, r′, i′, z′ filters), 27 images during the night of 2019-01-09 and 28 images

the night after. The 102 bias cube frame images were taken with an exposure time of 2^{-5} seconds during the afternoon of the first day of observations. The target is an unknown galaxy located at RA = 20.86418538h and DEC= −0.6229532711, detected in the IAC Stripe 82 Legacy Survey from Trujillo and Fliri [62]. Making sure that no pixel observes the same point in the sky as to minimize the problems related to the reflection of light inside the telescope, the observational strategy consist in a dithering scheme of 9 observing blocks with a rotation pattern. Firstly, a 9-points dithering pattern with 40 arcseconds of displacement from the center of the galaxy and a position angle of 0 degrees, then they change the position angle of 120 degree, they repeat the dithering scheme and finally the same 9-points dithering pattern with a position angle of 240 degrees. This dithering pattern makes an offset which is enough to have a proper background map. I worked with a total of 63 raw images of 42.1 Mb in .hcm format, each one corresponding to an observation time of 120 s. Each image is a cube frame of 20 images (HDUs) with standard headers, CCD and telescope parameters. The u′ filter image is made up with HDUs from 1 to 4, the g′ image with HDUs from 5 to 8, the r′ image with HDUs from 9 to 12, the i′ filter image with HDUs from 13 to 16, the z′ filter image with HDUs from 17 to 20.

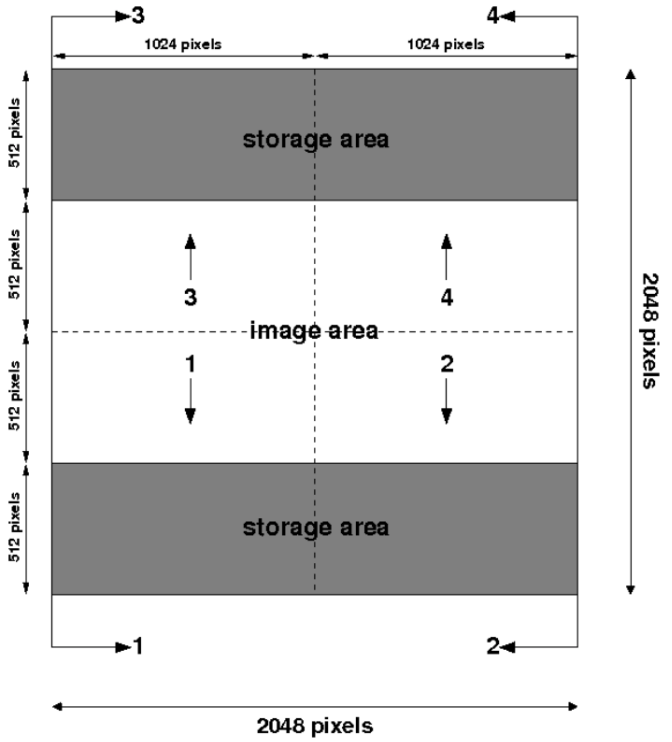

Figure 2.5: HiPERCAM CCD architecture. Credits to Dhillon et al. (2016).

Figure 2.5 illustrates the schematic of one CCD detector. Every CCD (one band image) is composed of 4 windows of 512 x 512 pixels (E, F, G, H). The windows have to be read from left bottom, right bottom, right top, to left top window for CCD 1, CCD 3 and CCD 4 (E1, F1, G1, H1). For CCD 2 and CCD 5 the sequence is left bottom, right bottom, left top, to right top window (E1, F1, H1, G1). We suppose that images are yet dark frame corrected because HiPERCAM's dark current is extremely low (10 electrons/pix/hr at 173 K) and uniform thanks to the thermo-electrically cooling of devices to -90° C. I have also not take into account the problem of fringing which occurs due to the upper atmosphere emission lines of OH during the night, in fact each CCDs has an anti reflection

coating that gives a fringe amplitude of 0.1% for i′ and 1% for z′ (e2v's anti-etaloning architecture: Astro Broadband in u', Astro Multi-2 in g', r', i', z'). I fortunately did not have problems of vignetting which means darkening of image corners when compared to the center. Vignetting is either caused by optics, or added in post-processing. Anyway it is possible to correct this problem by cutting bad columns and bad rows of the image, setting the values of those bad pixels with NaNs as not to affect the data reduction. To do this I developed a make script (*mask-bad-images.mk*) that can be easily added to the pipeline. Since vignetting can occur only in one filter, I annexed also the routine (*decompose.mk*) to decompose the cube raw image in five different CCD images (each one corresponding to a filter). I display in Figure 2.6, the H1 channel of the third HiPERCAM CCD before starting the reduction. The following Figure 2.7 shows with sls colors and logarithmic scale

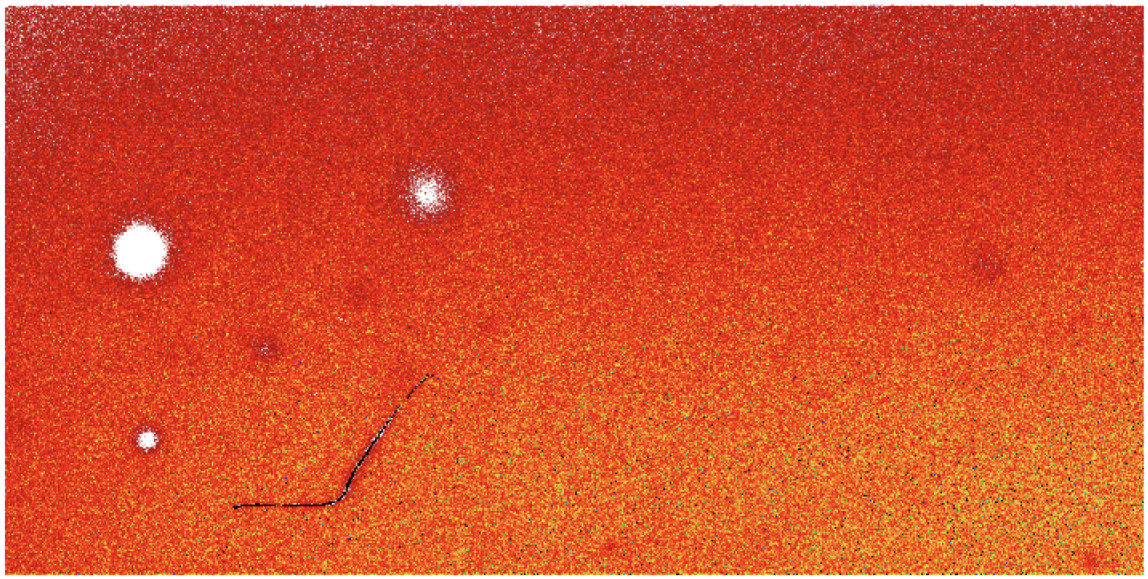

Figure 2.6: Raw image, H1 channel, R-band from HiPERCAM. Logarithmic scale, 99.5%, sls colors. SAOImageds9.

a different channel for u′, g′, i′, z′ filters. All images exhibit defects and artificial features, and they are not bias-corrected.

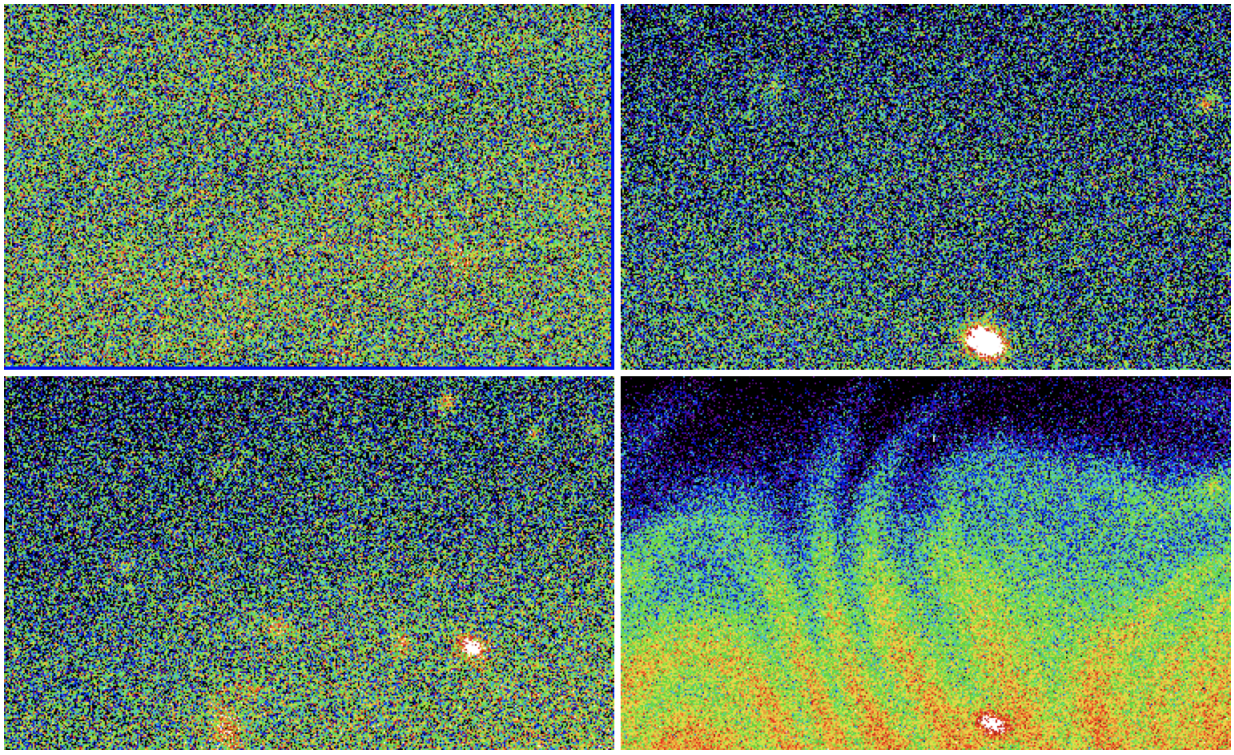

Figure 2.7: Left Top: u′ E1 channel, Right Top: g′ H1 channel, Left Bottom: i′ G1 channel, Right Bottom: z′ H1 channel. Logarithmic scale, 99.5%, sls colors. SAOImageds9.

2.2 Data reduction

All the reduction process follows a pipeline that I have saved online on Gitlab, called *Hipercam-pipeline project* at the webpage $< https : //gitlab.com/GiuliaGolini/hipercam - pipeline >$. In order to be able to run the HIPERCAM pipeline it is necessary to have it installed (see http://deneb.astro.warwick.ac.uk/phsaap/hipercam/docs/html/index.html). The architecture of the pipeline is easy: there are three main folders, one with the input images (Hipercam-inputs), one with all the scripts and configuration files (Hipercam-pipeline) and one with all the outputs (Hipercam-outputs). This pipeline can be downloaded and run from the console of every computer, with a 2.3 GHz Intel Core i5 processor computer I have taken 2 hours and a half to have a final stacked image just for one filter. Before starting any kind of subtraction raw-data should be decoded and modified to .fits format. I did it with an easy loop in console since I added only later the script *raw-to-fits.mk* to the web. The pipeline is fully automatic until the sky subtraction, then I decided to work with one filter each time to avoid any bug, so running script by script just by pressing the enter button when the process pauses. Since images are obtained with a CCD detector I follow the general technique consisting in eliminating, as far as possible, the instrumental effects that were introduced into the collected signal. In this section I discuss the main steps of this data reduction and I focus on troubles I encountered.

2.2.1 Bias correction

The overscan region is a part of the detector that is carefully shielded from the radiation and since these pixels are treated in exactly the same way as the others, their reading provides the signal level (pedestal) from which the image is constructed. The signal acquired from the overscan region, during the exposition to radiation, represents the bias signal to be subtracted from the whole image. The subtraction of this signal therefore eliminates the "pedestal" on which the image was built, thus returning to the pixels the value of the signal produced by radiation only. By subtracting of bias, we can remove the read noise contribution from the CCD and set the zero level of the camera independently of the pixel position and the observing time. The bias image does not affect on the visual appearance of the image. Since the bias can suffer from fluctuations during the observations it is good practice to acquire many frames to check this level with zero exposure time (102 images of 2^{-5} seconds in this case) with the shutter disabled. The bias image signal is due to the polarization currents, interference of the computer and the Readout Noise introduced by the electronics of HiPERCAM (theoretical value of 4.5 electrons at 263kHz). The RN expresses, the standard deviation of the statistical fluctuation of the output signal, with a constant input signal, it can be computed as:

$$RN = \sigma_{bias} G \tag{2.1}$$

and it is measured in electrons. G represents the gain of the camera (HiPERCAM gain is 1.2 $e^-/ADUs$) and σ_{bias} is the standard deviation of the bias image. I build the master bias by taking all the 102 bias images and combining all of them with a sigma-clip-mean between same extensions (hdus) to a single bias cube frame of twenty extensions. This master bias has a Gaussian ("normal") distribution with the range related to the read noise and gain of the detector. It is important to note here that each one of the twenty bias image extension has its own mean value, its own standard deviation and its own relative Readout Noise. Table 3.1 presents the mean and std values for each master bias image extension.

The resulting σ_{bias} is ranging from 0.05% to 0.9% of the mean bias values. The effective noise of the master bias can be computed by:

$$\sigma = \sqrt{RN^2(1 + 1/N)} \tag{2.2}$$

where N is the number of bias images combined. Each master bias HDU is then subtracted to the corresponding HDU raw image. Figure 2.8 displays the E1 channel master bias for the u′ filter.

Table 2.1: Master bias means and standard deviations for each HDU. Master bias is done by combining with a sigmaclip median 102 bias images.

Filter	Channel	Mean(ADUs)	Std (ADUs)	RN
u′	E1	1182.515	1.204	1.440
u′	F1	1195.884	0.856	1.027
u′	G1	916.340	0.931	1.117
u′	H1	1239.447	0.616	0.739
g′	E1	1173.910	0.836	1.003
g′	F1	1154.285	0.567	0.680
g′	G1	1209.559	0.515	0.618
g′	H1	1342.931	0.619	0.742
r′	E1	1575.773	0.534	0.640
r′	F1	1507.917	0.463	0.555
r′	G1	1119.680	0.520	0.624
r′	H1	1156.560	0.558	0.669
i′	E1	1277.292	6.915	8.298
i′	F1	1249.862	6.861	8.128
i′	G1	972.127	7.503	9.003
i′	H1	1392.365	7.110	8.672
z′	E1	943.807	0.775	0.929
z′	F1	1182.721	0.588	0.685
z′	G1	1278.563	0.878	1.053
z′	H1	1434.894	0.477	0.572

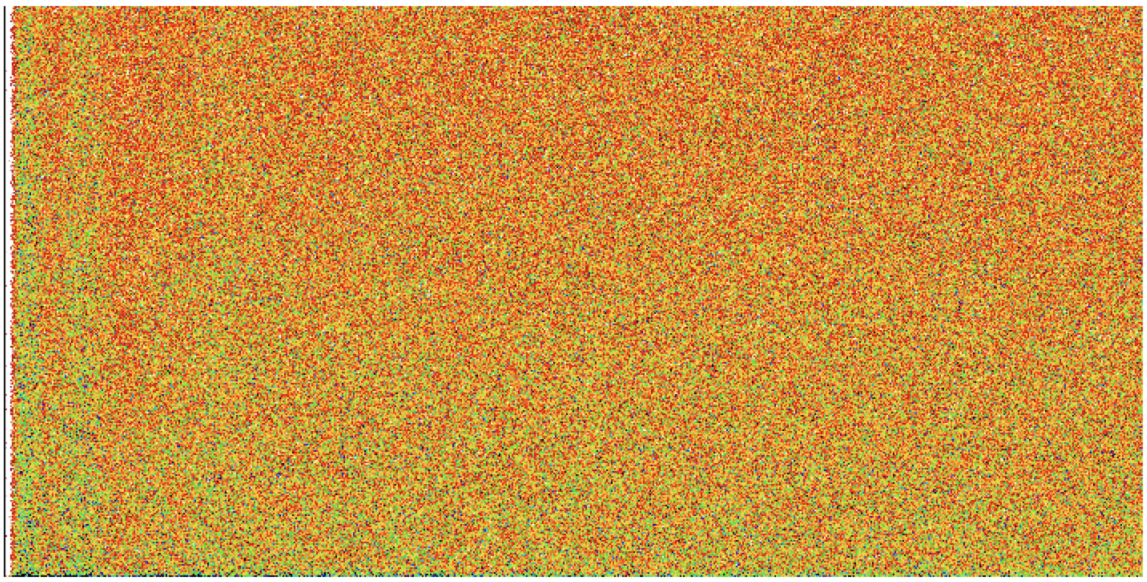

Figure 2.8: CCD 1, E1 channel Masterbias. SAOImageds9. Logarithmic scale, 99.5%, sls colors.

2.2.2 Flat correction

First flat correction

The correction of flat allows a compensation of the sensitivity differences between pixels. These differences may be due to the manufacture, to non-uniform transmissions in the optics, to deviations in the optical path (obstructions and reflections), to different electronic gains or quantum efficiency variations. All these causes produce a multiplicative error that must be corrected to restore the signal actually collected on the pixels with a flat image. The procedure to correct these differences is theoretically quite simple, it consists in observing a radiation source that is equally bright on the whole examined field to obtain a pixel sensitivity map. Finally, it is necessary to divide, pixel by pixel, the science images for the flat-field frame which is first normalized with respect to the average of the pixel values. However, flat fielding is the most challenging calibration routine, and the principal difficulty in proceeding with this kind of correction operation is to find a source that is really uniformly bright. Moreover, if broadband filters are used, the spectrum of sources used to obtain flat-frames differs from that of the observed astronomical sources, this can lead to systematic errors, the main causes that limit the accuracy of a flat-field. The best thing to do then is to acquire

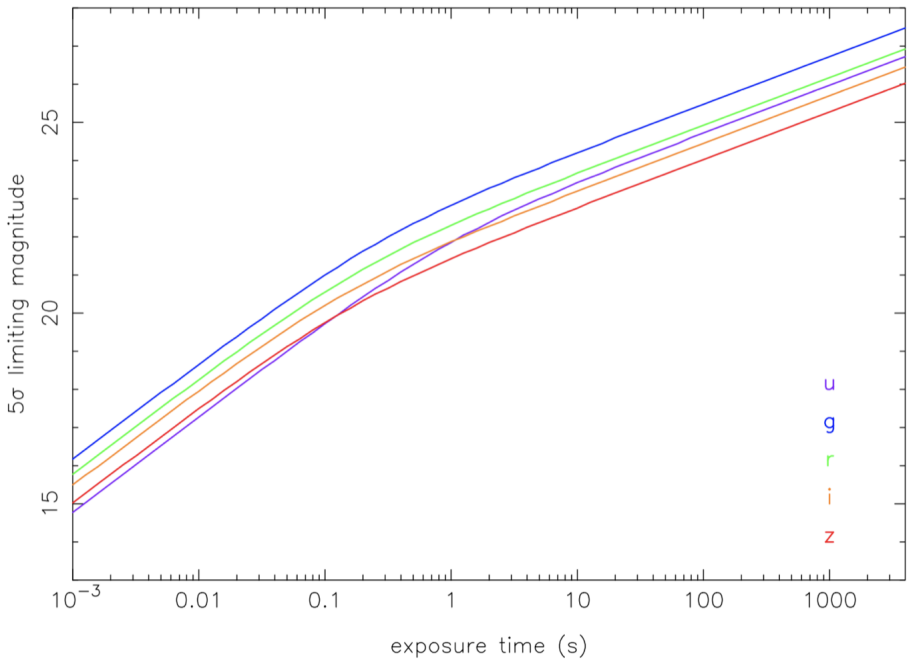

Figure 2.9: Limiting magnitudes of HiPERCAM on the GTC as a function of exposure time. The purple, blue, green, orange and red curves show the results for the u' g' r' i' z' filters, respectively. The calculations assume dark moon, observing at the zenith and seeing of 0.8". Credits to Dhillon et al. (2016).

different images of the same target that occupies different positions in the current field of view (the aforementioned dithering technique), and then do a median filtering of dithered frames. In this case the flat is built by using all science data, not on the dome of the telescope nor at sunset, twilight or with a dark sky, as astronomers used to do with infrared observations where the contribution of the thermal emission of the telescope and the dome are significant. The response of the CCD to the

stellar flux may not be linear, meaning that for example if we observe for a number of counts the telescope dome, the pixel response will may not grow linearly and it will not be proportionally the same during the whole night of observation (that may would be a bigger number of counts). Figure 2.9 shows the limiting magnitudes of HiPERCAM on the GTC as a function of exposure time, it is clear that the response decreases with time. I start the procedure with the normalization of all the 20 extensions present in each raw image. Normalizing means bring all the pixel values around one by taking the median value of the pixels in every image and by dividing each single hdu-image for its median pixel value. The median value is used, even if it reduces a little the accuracy (which cannot be better than 0.5 ADU), since it takes into account the values assigned to every single pixel of the image that appears the greatest number of times, the mean value instead takes into account the pixels which may contain a lot of stellar flux (but also bad pixels and cosmic rays) and overestimate the flat value. After this, with a sigma clip median I arrange all the normalized bias corrected extension images (63 images for each HDU) into a final flat cube frame image. Finally, the effective correction of flat is made by dividing each bias corrected channel (HDU) image by the corresponding channel flat image. Figure 2.10 illustrate on the left side one H1 channel i′ band raw image and on the right side the corresponding first version of flat. The subsequent Figure 2.11 displays the same i′ filter HDU divided by the flat.

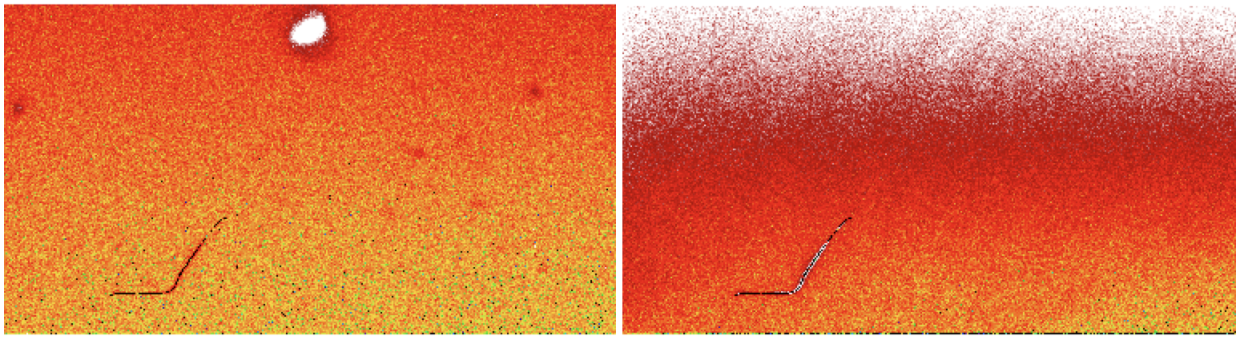

Figure 2.10: Right side: Raw i′ band image (Channel H1) Left side: i′ band flat image (Channel H1). Logarithmic scale, 99.5%, sls colors. SAOImageds9.

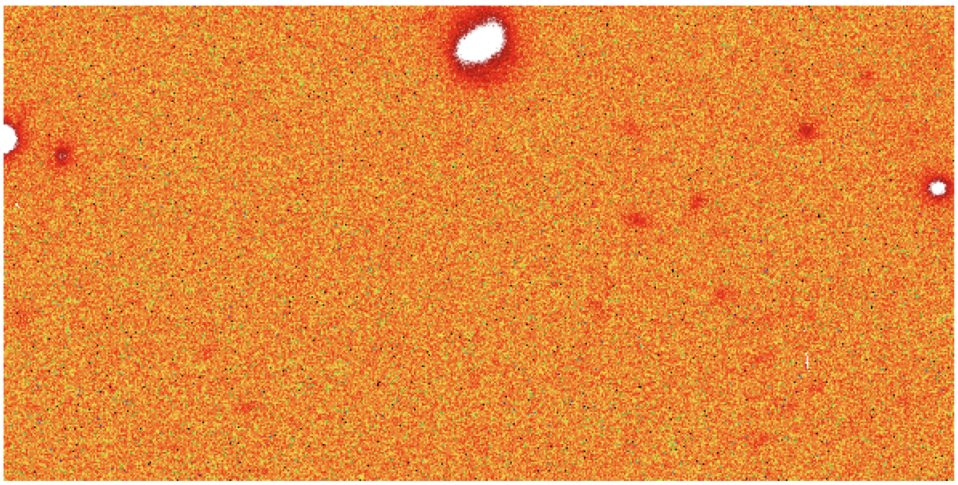

Figure 2.11: Flat corrected i′ band image (Channel H1). Logarithmic scale, 99.5%, sls colors. SAOImageds9.

The standard deviation for the different channels flat images ranges from 0.01 to 0.1. How do the errors on the flat estimate propagate when we evaluate the light coming from an astronomical source? The detected flux F is the sum of that of the source S plus that of the background B and since we cannot evaluate the foreground radiation exactly, we must settle for an estimate of it near the source. So, when the astronomical target is bright as the sky, an error of 1% in the evaluation of the background (B) corresponds to a relative error of 1% on the signal obtained for the source (S). If, however, the background is B $\sim$ 100 S then the error would be 100%. The flat-field correction is crucial in the case of very faint sources then.

Second flat correction

The first version of the flat allows removing possible fake signals captured by the image but especially when the astronomical target is very faint it can be confused with noise and it is convenient to do a further flat correction based on masking images. By masking images the values recognized as true sources are substituted with not a number (NaN). This is an important step because NaNs do not add up to the average. So, the first thing I did, was use *Astnoisechisel*. *Astnoisechisel* is a Gnu-make software which takes a fits extension image as input and build one output cube image with 4 extension: the input image with the sky subtracted, the mask of the image, the sky and the rms of the sky. The mask is the image containing the pixel value 1 where the software has recognized a real source and the value 0 where noise is detected. All images are masked by setting the NaN value on pixel containing real signal. Then I had to normalize the masked image by dividing by the median pixel value of the image and finally, the second flat image is computed by combining with a sigma clip median the masked and normalized images in each CCD's window. The second flat correction is done, as for the first, by dividing each bias corrected image extension for the corresponding second flat. Figure 2.12 displays the 4 steps of the second flat subtraction procedure on g′-band images. In the upper left side Channel E1 before the second flat correction is presented, while on the bottom left Channel E1 after the second flat correction is shown. On the upper right there is the corresponding mask for Channel E1 done on the first flat corrected image and on the bottom right the second version of flat on the same channel.

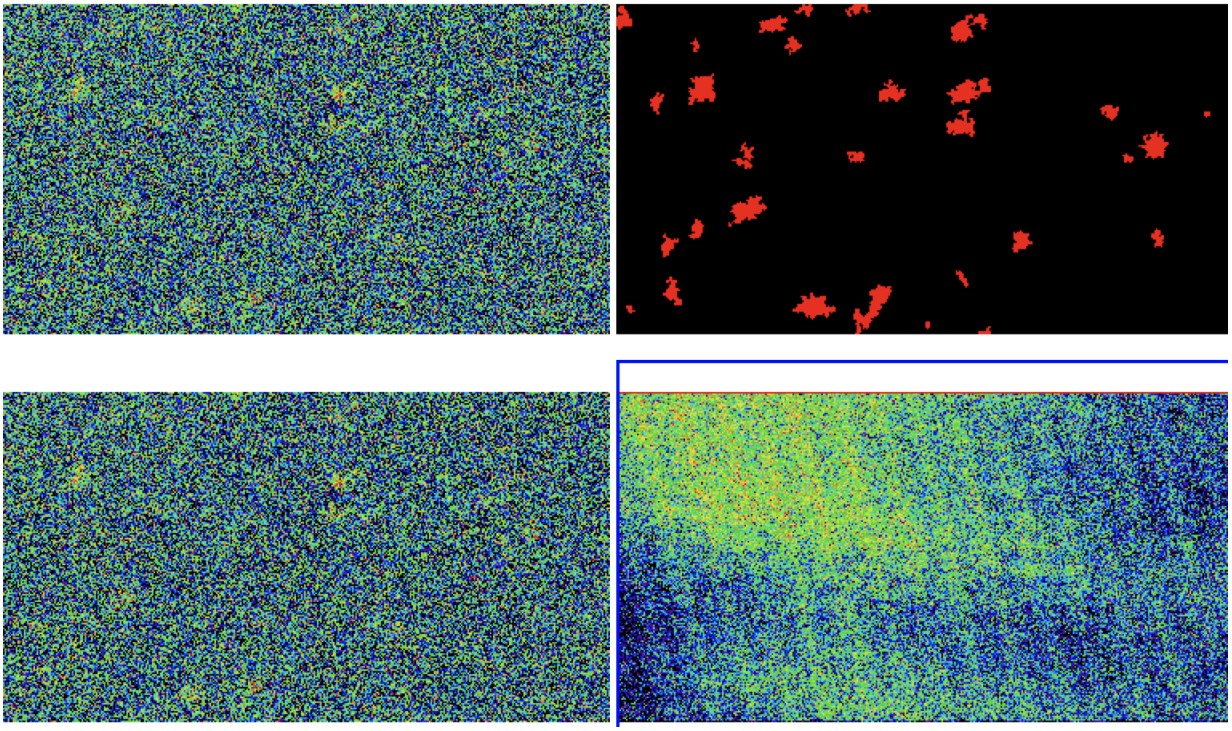

Figure 2.12: g′-band images. Upper left : Channel E1 before the second flat correction. Bottom left: Channel E1 after the second flat correction. Upper right : Channel E1 mask. Bottom right: Second version of flat for g′-band Channel E1. Logarithmic scale, 99.5%, sls colors. SAOImageds9.

In this case, the standard deviation for the different channels second-flat images ranges from 0.01 to 0.09.

2.2.3 Gain correction and arrangement of the CCD image

Arrangement of the four channels to one CCD's image

This step is needed because, as previously explained and highlighted in Figure 2.5 every CCD in the HiPERCAM camera is composed of 4 windows (E1, F1, G1, H1). The fits cube image is composed by the sequence E1, F1, G1, H1 for CCD 1, CCD 3, CCD 4 which correspond to u′, r′,i′ filters, CCD 2 and CCD 5 have the structure E1, F1, H1, G1 instead. Moreover, the area observed in the sky is sparsely populated so each single channel contains few real sources and it could be a problem when trying to make astrometry later during the data analysis. To join images I build a Python routine that takes as input the flat corrected images and has as an output a final cube frame holding 5 extension, each one corresponding to a band (from u′ to z′).

Gain correction on individual images

This arrangement step is not so simple because the effective gain of windows is not the same and it can change during the night. If you compute a standard alignment of the four channels of a CCD it is certain that one part of the full image can appear lighter or darker than the others, or even no one well-connected. Figure 2.13 emphasizes this imperfect mach and the artificial structure due to the typesetting of windows for the i′ filter. The upper right part (G1) looks lighter than the lower left section (E1), which one seems to be lighter even than the other two (F1, H1).

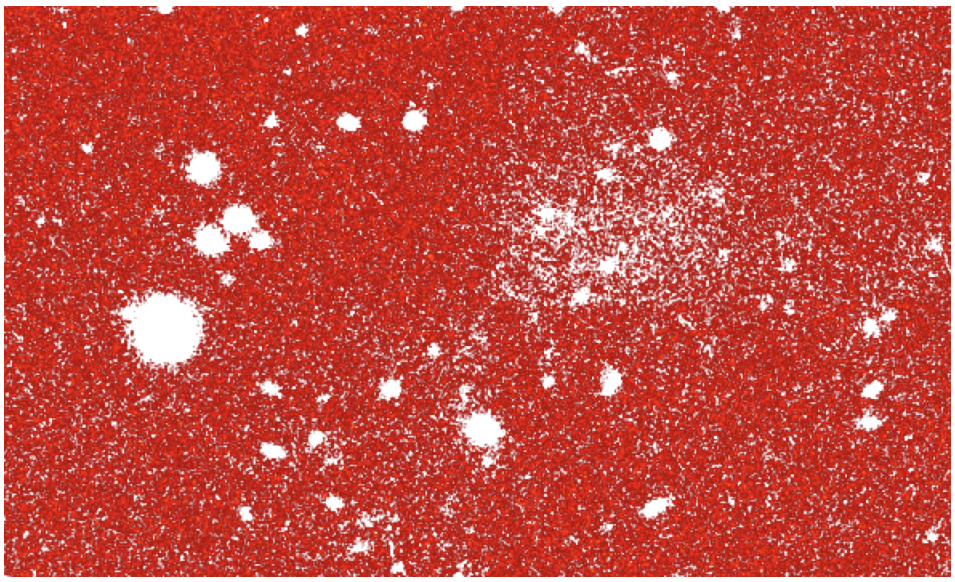

Figure 2.13: Un-uniformity when arranging channels in ′i filter. Logarithmic scale, 99.5%, sls colors. SAOImageds9.

To correct this un-uniformity I take 3 columns of pixels at the end of the bottom left side window (E1) and I compute the median $m_{b,l}$ among those pixel values. The same is done with the columns at the beginning of the bottom right side one ($m_{b,r}$). Then I compute the quotient of the two median values F_{bottom}:

$$F_{bottom} = \frac{m_{b,l}}{m_{b,r}} \tag{2.3}$$

and, assuming that the left image is correct, I multiply the right one (F1 channel) by that factor:

$$F1 \cdot F_{bottom} \tag{2.4}$$

The same is done for the two upper channels, G1 and H1 taking the median values of the last or first columns depending on the CCD structure and estimating the quotient. Equally, I reckon then the quotient between median values of the bottom tree rows of the combined upper strip and the upper three row of the bottom strip and. Finally, by assuming that the bottom strip is good I multiply the upper strip by the final quotient. Each CCD image is now arranged and gain corrected individually. Figure 2.14 points out that the gain correction must be applied in order to correct the imperfect join.

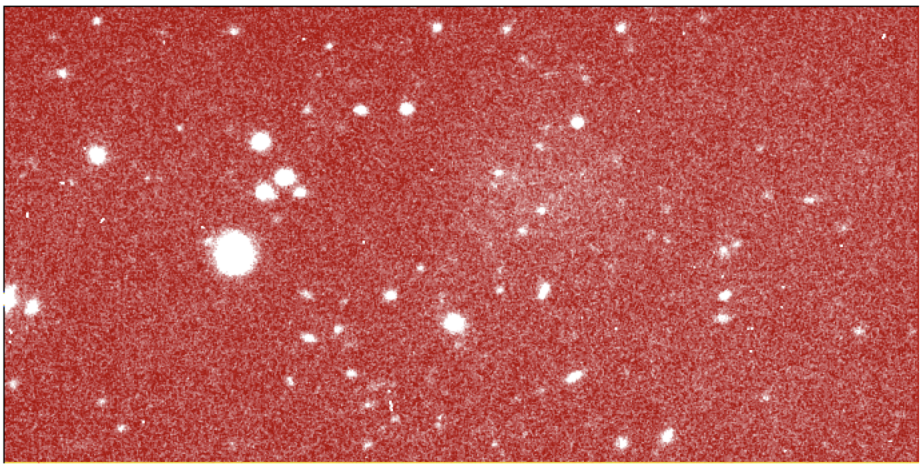

Figure 2.14: Arranged ′i filter image. Logarithmic scale, 99.5%, sls colors. SAOImageds9.

Gain correction with mean coefficients

It can happen that raw images are taken over a long exposure on source or maybe even for different nights. In this case the 63 images were recorded during 2.25 hours on source over two consecutive nights. Depending on the quality of observations and on the structure of the camera we can assume that the gain value do not change a lot during the whole time (or it does) and decide whether to use this step or not. This will affect the final co-added image, meaning that when you stack all the CCD images at the end of the process you may see non-homogeneity that recalls the architecture of CCDs. To improve this kind of correction I tested the distributions of the median coefficients among all raw cube images. Each filter must be analyzed individually. If that distribution is Gaussian then I can take its mean value and use it to multiply channels instead of employing the single quotient value. I used this step to improve the joining of g′, r′, i′, z′ filters. Since u′ presents a two-peak distribution of the coefficients, the second gain correction is not applied. As an example, Figure 2.15 expose the i′ filter histogram of the 63 F_{bottom} coefficients. The distribution is nearly Gaussian with a mean value of 1.002 and a standard deviation of 0.005. The following Figure 2.16 shows the u′ filter histogram of the F_{bottom} coefficients which is not normal-like. The standard deviation around the mean value of 0.9 is 0.01. High precision is required so even if 0.01 seems not too huge

it can bring inhomogeneities.

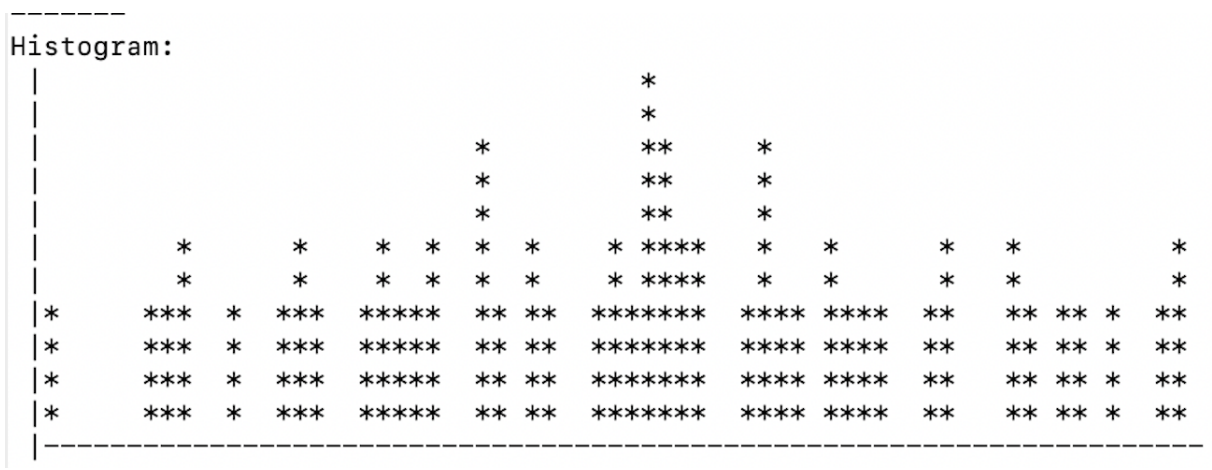

Figure 2.15: Histogram of the gain-correction bottom i′ coefficients.

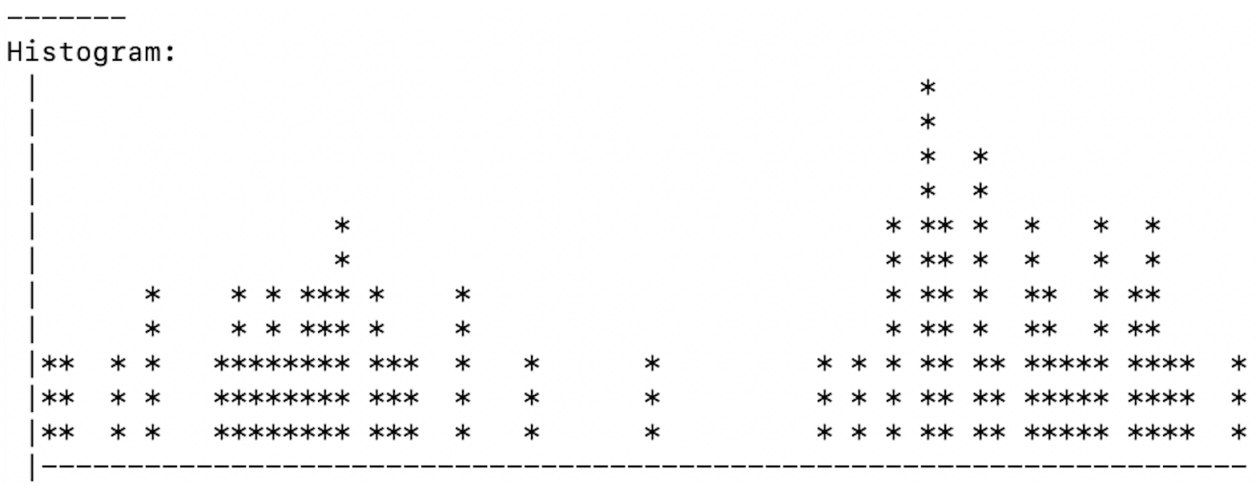

Figure 2.16: Histogram of the gain-correction bottom u′ coefficients.

The comparison between the first version of gain correction and the second one is almost imperceptible and difficult to observe with naked eyes but if we care of the final result, the inappreciable difference can lead to significant improvements. The left panel of Figure 2:15 illustrates one of the 63 full z′ image corrected with the individual coefficients, the left image is corrected with the mean coefficients. While switching from the image on the right to the one to the left, pixel values change by less than 10 counts.

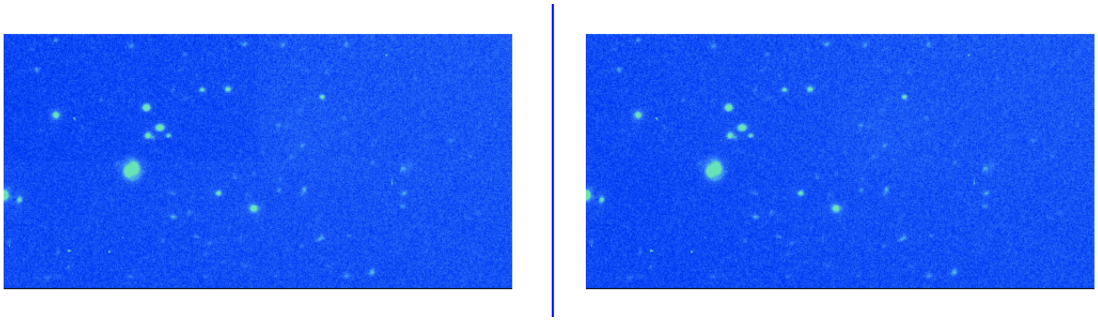

Figure 2.17: Full z′ CCD image. Right panel: Gain correction image by image. Left panel: Gain correction with mean coefficients. Logarithmic scale, 99.5%, sls colors. SAOImageds9.

2.2.4 Sky subtraction

An accurate estimate of the background noise is necessary to measure the morphological properties of astronomical sources and to asses photometric errors. Unfortunately, it is a hard task and there is not a single standard method to evaluate background. The correction of the sky is a crucial step especially during the reduction of data related to very faint objects where the halo of the galaxy or the intra cluster light can be underestimated. Depending on the target and observational conditions during the night the correction can be done by subtracting the median value of pixels in the image, a plane or a parabola. However, when evaluating the median, the value is overestimated and biased by the presence of real sources in the image. To solve this problem I masked the sources in the image by using *Astnoisecheisel*. To have a good mask, to maximize the source detections and to be the most representative, I played with *Astnoisecheisel* parameters, such as qthresh, detgrowquant, tilesize and threshold. I decided not to iterate the masking process in order to not over-subtract the sky. The covered sky area is very small so it is possible to assume that there is no gradient for the sky value. But the wavefront is not flat, so I decided to fit a 2D background model on masked images. Finally, the sky fit is subtracted from the gain corrected image. Figure 2.18 presents the

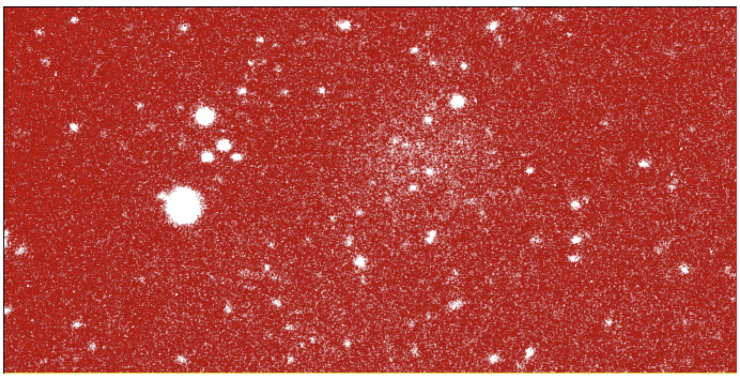

Figure 2.18: Gain-corrected g′ image. Logarithmic scale, 99.5%, sls colors. SAOImageds9.

g′ input image taken by *Astnoisecheisel* to build the mask which is shown in Figure 2.20. Then the image is masked and with a python routine I build the sky polynomial fit displayed in Figure 2.22. Finally, the sky-fit image is subtracted to the gain corrected one and the result is illustrated in Figure 2.22.

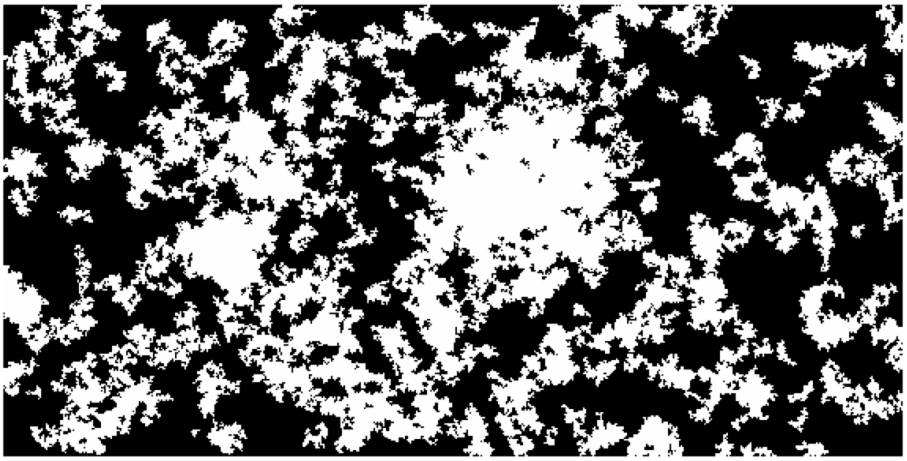

Figure 2.19: Mask of the gain-corrected g′ image. SAOImageds9.

Figure 2.20: A g′ image sky-fit. Sls colors. SAOImageds9.

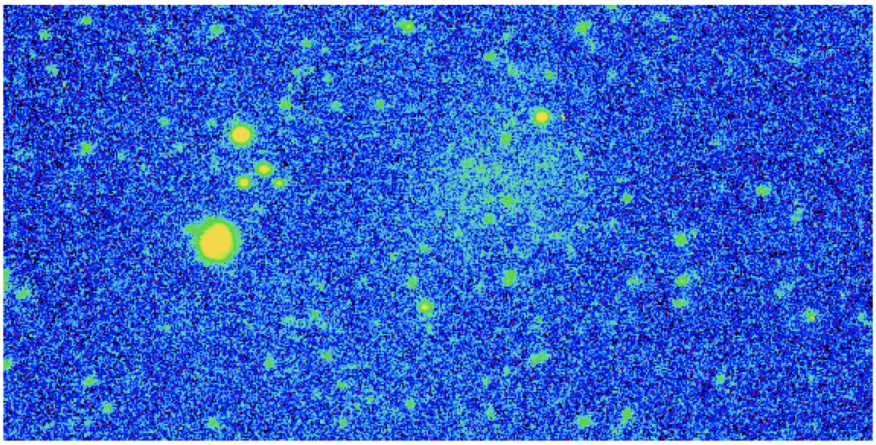

Figure 2.21: Sky corrected g′ image. Logarithmic scale, 99.5%, sls colors. SAOImageds9.

2.2.5 Astrometric calibration

In order to determine the Astrometric position (Right Ascension and Declination) of an object within our CCD image, it is necessary to know precisely the position of at least three reference stars in the sky and define the geometric scale factors to transform the X and Y coordinates of the CCD pixel grid of our image into the corresponding celestial coordinates (RA and DEC). The astrometric calibration has to be done for all individual dithering images in order to build a final stacked image without misalignment. I took as a reference the SDSS stripe 82 catalogue downloaded from Vizier, which one contains the most stars in the field of view around the ultra diffuse galaxy. To check whether the match between sources of Hipercam images and the SDSS catalog is good or not I sent to SAOImageds9 the catalog opened with TOPCAT. The result is Figure 2.22, green circles identify Stripe 82 sources over the background g′ science image.

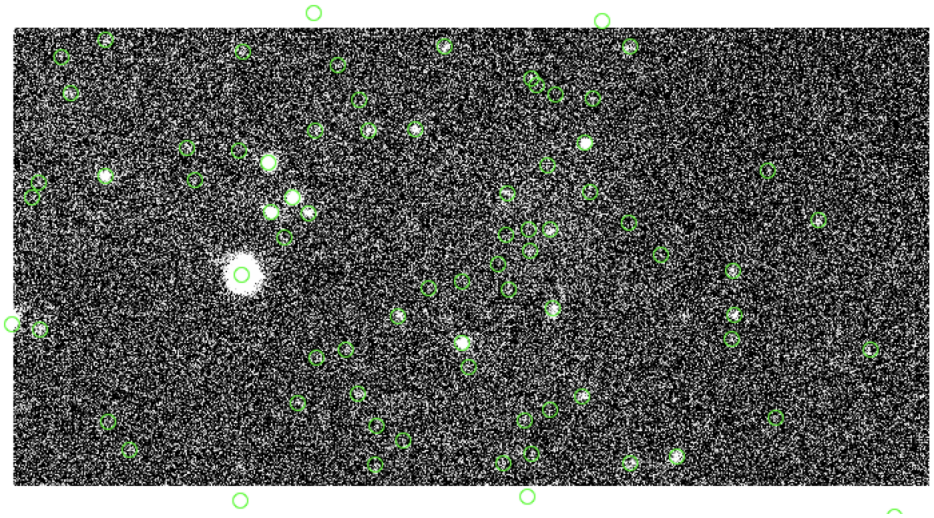

Figure 2.22: Matching between Stripe 82 catalog and Hipercam g′ science image g′.Logarithmic scale, 99.5%, grey colors. SAOImageds9. Green circles identify sources of Stripe 82.

Then I used solve-field ($https://www.mankier.com/1/solve-field$) and Sextractor to build the additional catalogs needed and compute the astrometric solutions. Unfortunately, since solve field needs at least few tens of reference stars in order to compute the astrometric calibration automatically, I could not run it on u′ filter image. In this observational case, solve field is not able to recognize in the science image more than 10 reference stars. To solve the problem it is possible to lower the –odds-to-solve parameter (which is $1{\cdot}10^6$ default) or to turn down the code tolerance but so much accuracy is lost, some image would not be placed in the correct position of the sky while computing the final stacking. Another method is to use the celestial coordinates of the center of g′ images, where solve field can work because it identifies more stars. By giving manually to the routine the coordinates of RA and DEC of the center of each g′ images that have to be applied to calibrate the u′ filter. However, the procedure that made it possible to resolve the issue consists in build a Moffattian function (spatial convolution) which has to be applied to each u′ filter image. The kernel function is displayed in Figure 2.23. It works as a smoothing and allows detecting more sources. The difference between before an after the application of the spatial convolution is shown in Figure 2.24.

After this smoothing I run solve-field and I could make the astrometry calibration even on u′. Since

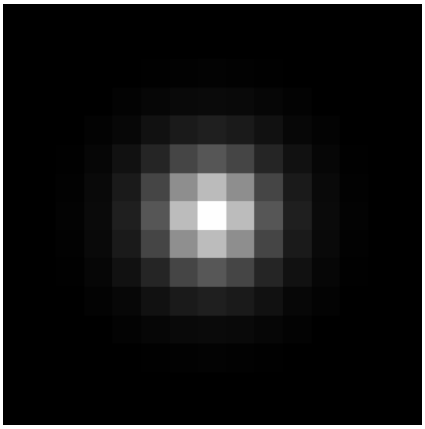

Figure 2.23: Kernel function. SAOImageds9.

this method increase the accuracy, I applied it also to the other filters.

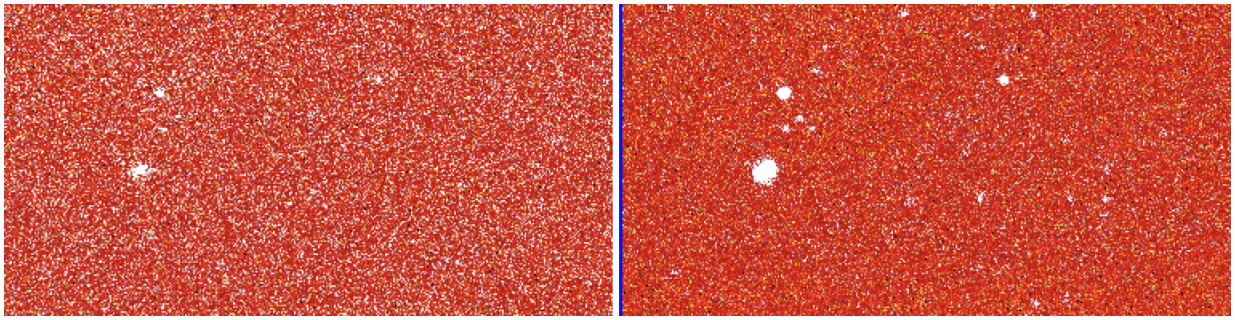

Figure 2.24: Before and after the convolution with a Kernel function U-filter. Scale Log, 99.5%, sls colors. SAOImageds9.

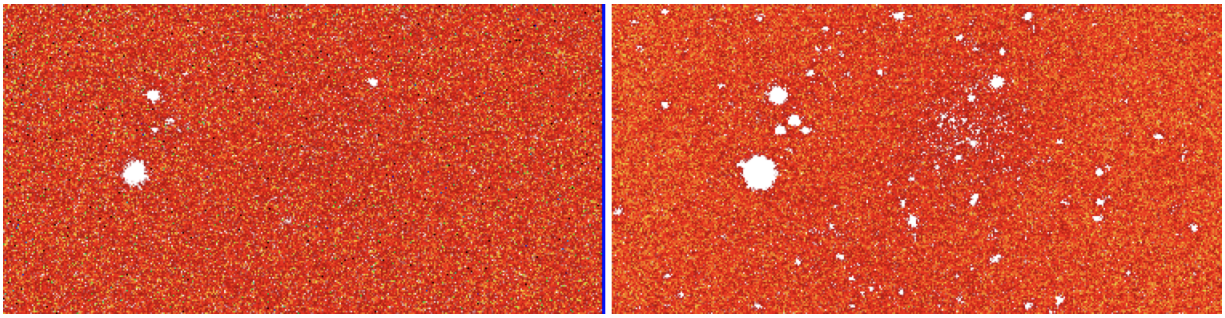

Figure 2.25: Before and after the convolution with a Kernel function G-filter . Scale Log, 99.5%, sls colors. SAOImageds9.

2.2.6 Photometric calibration

I based the photometric calibration on the photometry of the SDSS Stripe 82 catalog within my field of view. Real sources of my science images are matched with the Stripe 82 standards using a $1''$ matching radius. I used astmakecatalog to build catalogs on my science images and compute the science magnitudes m_s. After matching, the magnitude difference distribution as a function of reference magnitude has a very low scatter and images are re-scaled to a final common zero-point of 22.5. The photometric calibration factor δm is computed as:

$$\delta m = m_{stripe82} - m_s \tag{2.5}$$

and the pixel scaling factor f as

$$f = 10^{-0.4*\delta m} \tag{2.6}$$

This photometric calibration is necessary to switch from counts (pixel values) to magnitudes and it is done on every individual science image, for each optical band.

2.2.7 Final co-addition of images and RGB image

To improve the co-addition I decided to combine images with a sigma-clip mean instead of using SWarp (Bertin et al. 2002), since it automatically uses the median of FITS images to put all data into a common grid. Firstly I resampled the individual images on a bigger one of 4084 x 4484 pixels (73 Mb) and then I substituted the pixels with 0 value to NaN. This is necessary because zeros can affect the final sigma-clip mean value. The final g′ coadded image is shown in Figure 2.26 which is significantly deeper than the individual exposures. As a matter of fact the single images hide low surface brightness features that now appear. The ultra diffuse galaxy emerge just below the center of the image, at RA = 20.86418538h and DEC= −0.6229532711. The galaxy emission is different at different wavelengths. On the left panel of Figure 2:24 I illustrate the u′ final stacked image whereas on the right side there is the z′ image with the same scale parameters and colors.

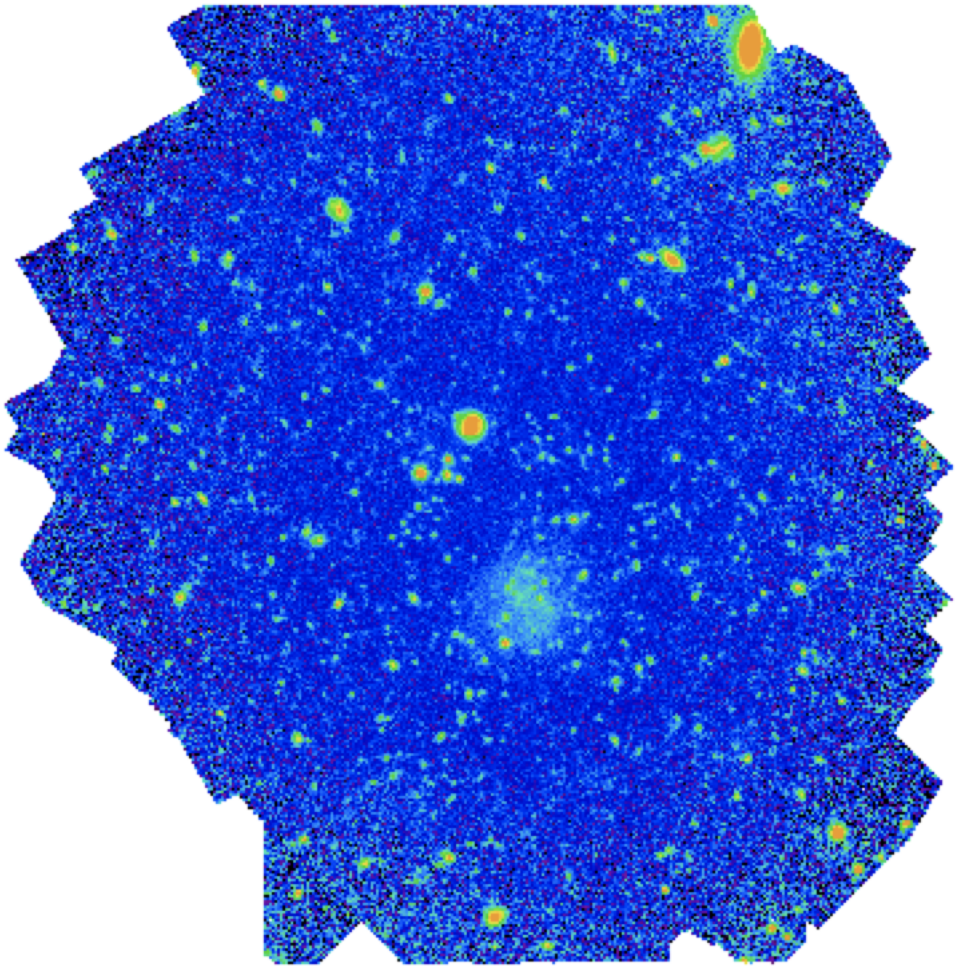

Figure 2.26: g′ co-added final image. $\sim 5'x5'$. Scale Log, 99.5%, sls colors, block 4. SAOImageds9.

To compute the RGB colors image of the galaxy I used the Python routine $< RGB.py >$. The inputs are the g′, r′, i′ filter co-added images and the output is pointed out in Figure 2.28. It is possible to change the percentage of lighter and darker colors by simply modify the Python script. Colors are very similar to the ones on SDSS server.

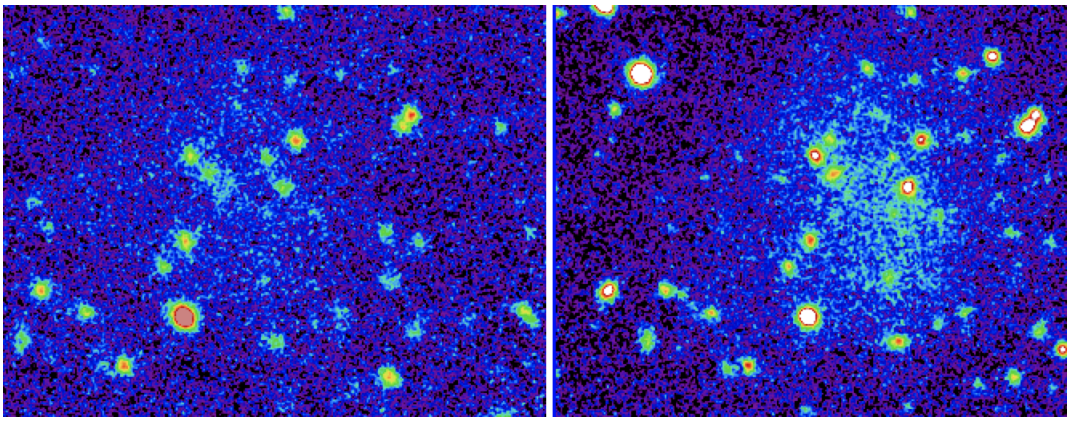

Figure 2.27: Left panel: u′ stacked image. Right panel: z′ stacked image of target UDG. Scale Log, 99.5%, sls colors, block 4. SAOImageds9.

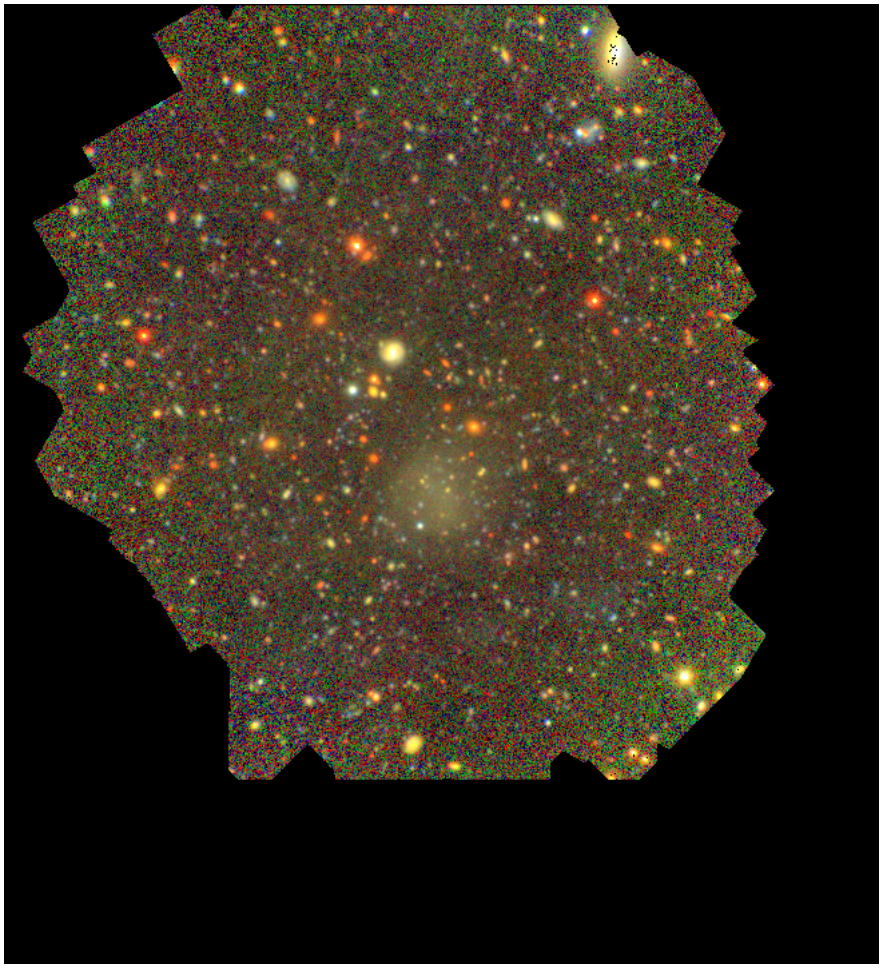

Figure 2.28: RGB colors image.

2.2.8 Further considerations on flats

For what concerns this data reduction procedure, the flat is done by using all 63 science images, which correspond to two consecutive nights of observations. However, the night sky brightness could vary during the course of several nights and the sky pattern could change intensity, so if the observational conditions change a lot during the time this way of combining the master flat could not be very representative of background. This problem is reflected in noticeable artificial structures that recall the structure of the CCD. In particular, these features come out in Figure 2.29, which highlight a piece of the final co-added i′ image next to the target galaxy.

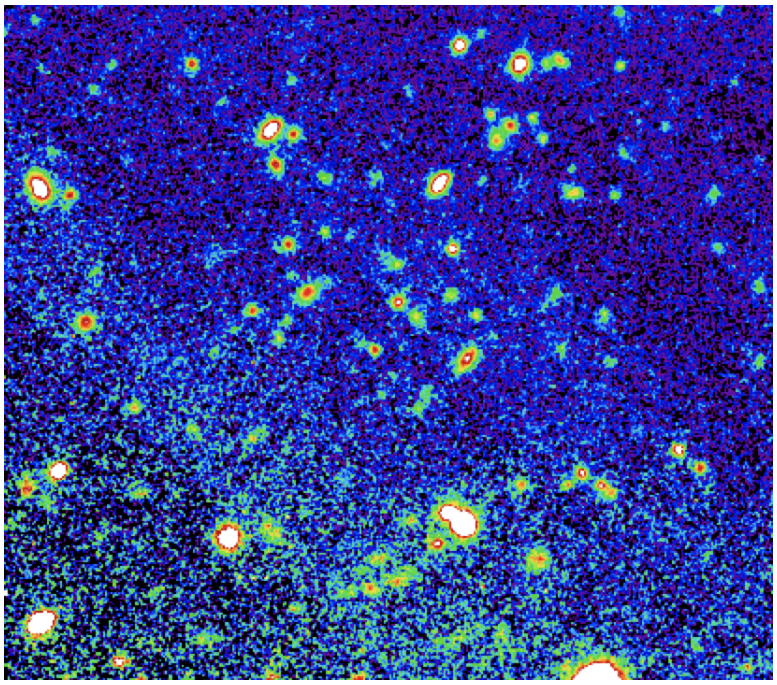

Figure 2.29: Artificial structures in the final co-added i′ image. Scale Log, 99.5%, sls colors, block 4. SAOImageds9.

To improve the stacking, sometimes it could be better to use a master flat built on nights of observation images or even on dithering blocks images. To check what is the best solution, I built a master flat for each night, and other seven master flat, each one corresponding to a block of observations. Then I computed the quotient between two of them: the quotient between first night master flat and second night master flat, the quotient between block master flats of the same night and the quotient between block master flats of two different nights. On the left side of Figure 2.30 I illustrate the u′ flat of the first night and on the other side the u′ flat of the second night. Though the structure is similar and the mean pixel value is ~ 1, the individual pixel values can change up to 0.04. The same difference between flat of different nights can be appreciated also in other filters, Figure 2.31 shows the difference for i′ filter (rms = 0.03); first night master flat on the right and second night master flat on the left side. The histograms of the difference between u′ night flats and i′ night flats is presented in Figure 2:31. Rms of i′ filter is 0.0076 while the rms of u′ is 0.035.

The same analysis was done with block master flats. I report as an example the difference between flats built with 2 different blocks images of the first night of observations in Figure 2.34, where on the right side appears the i′ filter master flat for the first block of dithering images (F1 Channel) and

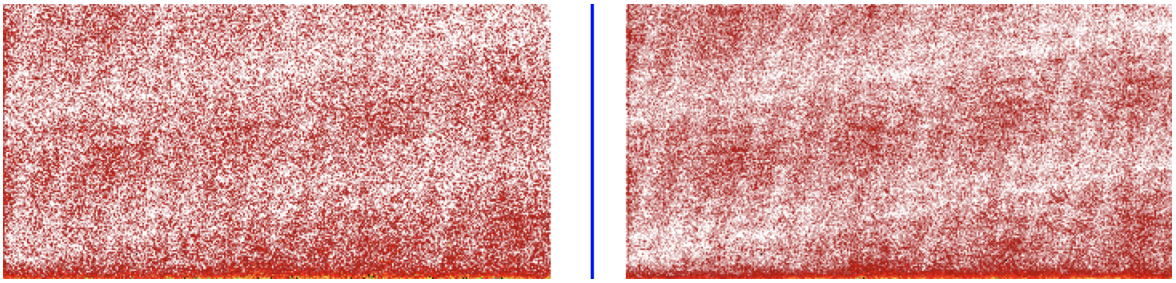

Figure 2.30: Left panel: Master flat built on night-1 u′ individual images (Channel E1). Right panel: Master flat built on night-2 u′ individual images (Channel E1). Scale Log, 99.5%, sls colors, smoothed. SAOImageds9.

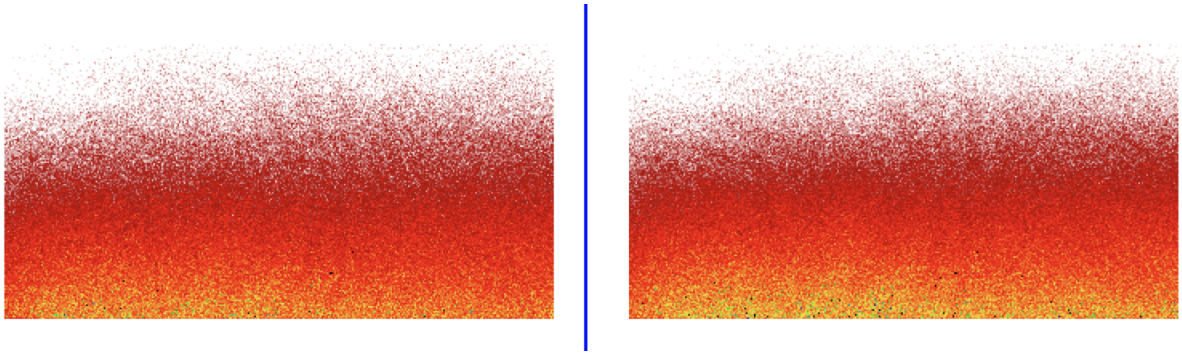

Figure 2.31: Left panel: Master flat built on night-1 i′ individual images (Channel H1). Right panel: Master flat built on night-2 i′ individual images (Channel H1). Scale Log, 99.5%, sls colors. SAOImageds9.

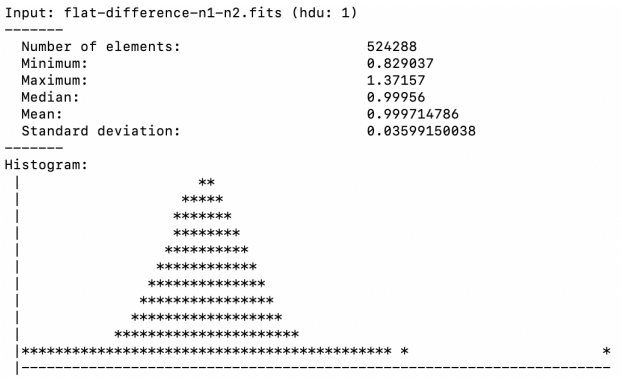

Figure 2.32: Histogram of the difference between u′ night flats (Channel E1).

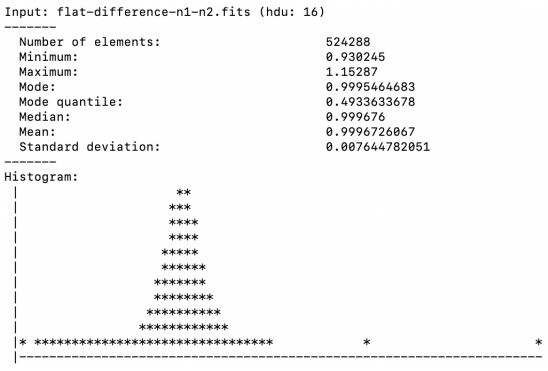

Figure 2.33: Histogram of the difference between i′ night flats (Channel H1).

on the right side the last block of dithering images of the same night (F1 Channel). Subsequently, I examined the difference between dithering blocks of different nights as illustrated in Figure 2.36 and I studied the Histograms of the quotient distributions.

In case of u′ filter the rms of the difference between dithering block master flat is 0.06 during the same night and 0.07 during different nights. While for i′, the standard deviation is ∼0.01 in both cases. Since the standard deviation of flat is given by the quadratic sum of the error due to noise and the error due to the gradient, I would expect that the rms between different blocks is less than between different nights. However, in this case, it is the gradient that dominates the error. As a matter of fact by looking with Ds9 at the ratio between flats built with night individual images

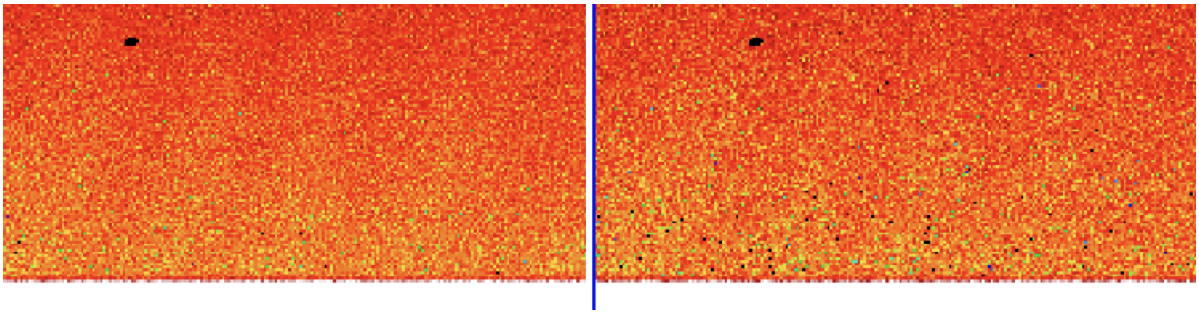

Figure 2.34: Left panel: Master flat built on night-1, dithering block-1 i′ individual images (Channel F1). Right panel: Master flat built on night-1 i′, dithering block-1 individual images (Channel F1). Scale Log, 99.5%, sls colors. SAOImageds9.

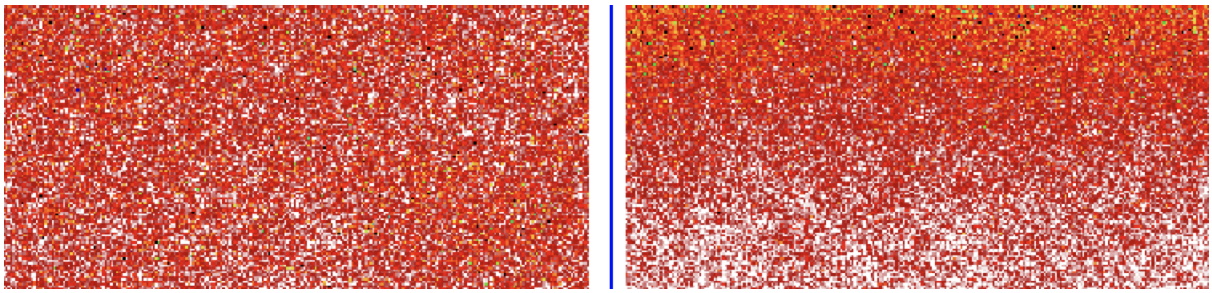

Figure 2.35: Left panel: Master flat built on night-1, dithering block-1 i′ individual images (Channel G1). Right panel: Master flat built on night-2 i′, dithering block-1 individual images (Channel G1). Scale Log, 99.5%, sls colors. SAOImageds9.

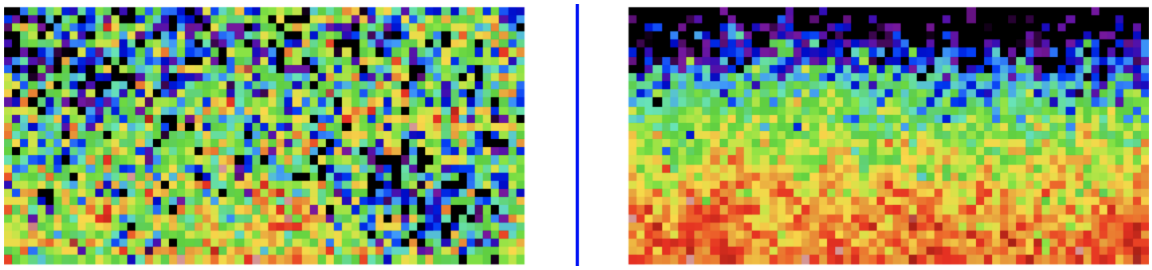

Figure 2.36: Left panel: Difference between master flats built with i′ individual images of different nights (Channel G1). Right panel: Difference between master flats built with dithering block individual images of the same night (Channel G1). Scale Log, 99.5%, sls colors, block 4. SAOImageds9.

and flats built with dithering blocks images, as emphasized in Figure 2.36 on the right and on the left side respectively, one can appreciate the presence of a color-gradient. The number of one color pixels that compose the two images is more or less the same and the standard deviation around the mean value is 0.05 for both. This mean that Aststatistics is not able to detect this gradient due to the fact that it is mathematically not appreciable. The variations of the gradient are greater than the fluctuations of noise. For the moment I am satisfied to work with a master flat built by combining all the science images collected, since the problem does not appear in the filters g′ and r′ and the artificial structures do not overlap with the image of the galaxy. Anyway it is worth handle this issue in further works.

Chapter 3

Photometry of the faint target galaxy

This chapter begins with the analysis the sources that are located near the target galaxy. To do this I referred to online catalogs such as SIMBAD and GAIAdr2 in the optical regime and 2MASS in the infrared. Later I focus on the galaxy, which is composed by stars that cannot be resolved in the image, and I explain the method that allowed me to estimate its brightness to verify whether it is actually a low-surface galaxy or even an ultra-diffused galaxy. Since I cannot use the standard process to do surface photometry which consists in fitting ellipses to isophotes because the galaxy is not well-defined, I proceeded in another way. The method I used consists in masking the bright sources in front of or behind the galaxy and it allows to accurately define the edges of the galaxy in order to not confuse real signal with background emission and to not affect the final brightness estimate. After that, from the comparison of the Spectral Energy Distribution of the galaxy with theoretical models I assess the metallicity and the Mass-to-Light ratio of the galaxy.

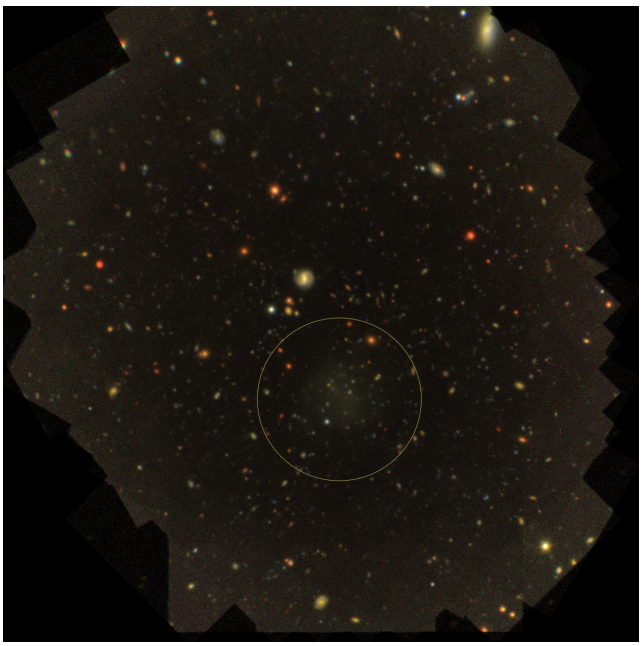

Figure 3.1: Sources around $RA = 20.86418538$h and $DEC = -0.6229532711$. Dimension: $4'$x$4'$ RGB colors.

3.1 Visible structures in the field of view around the UDG

Figure 3.1 displays the result of my effort, that is an RGB image of the galaxy ($RA = 20.86418538$h, $DEC = -0.6229532711$) and its surroundings. The galaxy appears diffuse and very faint, it is located just below the center of the image and it is highlighted with a yellow circle. The full image covers an area of $4'$ x $4'$. I verify the goodness of the image by comparing it with the official and referred images on the Aladin Sky Atlas website. As further confirmation I report the data of the astronomical sources cataloged with SIMBAD, GAIA dr2 and 2MASS which I have founded in this field of view.

The SIMBAD database provides two sources that I visualize with bluish circles in Figure 3.2, one on the upper left and one on the upper right of the pink-crossed target galaxy.

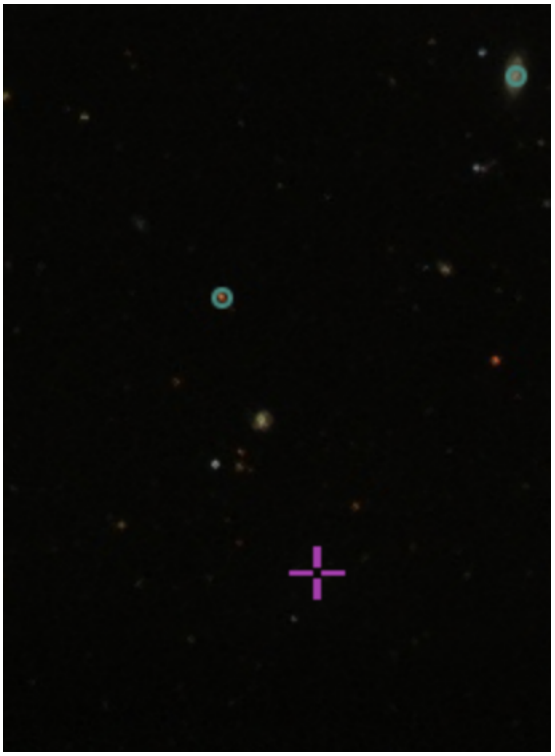

Figure 3.2: Sources around $RA = 20.86418538$h and $DEC = -0.6229532711$. AladinLite. Bluish circles identify sources cataloged with Simbad. The pink cross identifies the target galaxy.

LEDA 1139929, the upper right source, is a Seyfert 1 Galaxy with the following characteristics: it is located at RA(J2000)=140.360433 and DEC(J2000)=-62.363537 (Galactic coordinates), it has a redshift equal to 0.0278, it has relative fluxes described in Table 3.1 and finally has a radial velocity of V = 8242 km/s. This galaxy is highlighted on top right corner in both panels of Figure 3.3 with a yellow circle. It is worth noting the huge difference in resolution between the left panel which presents the galaxy observed with GTC and the right panel, where LEDA is observed with SDSS.

The other SIMBAD source is the SDSS J012329.48-003552.8 star. It is located at RA(J2000)= 140.4278108032206 and DEC=(J2000)-62.3759653844877 (Galactic coordinates), it has a redshift ~ 0.000290 and it has a radial velocity of 87 km/s. The star appears as a bright red dot on the top of both panels of Figure 3.4 circled in yellow. It is a low-mass ($M \leq 1M_{\odot}$) star and its fluxes are

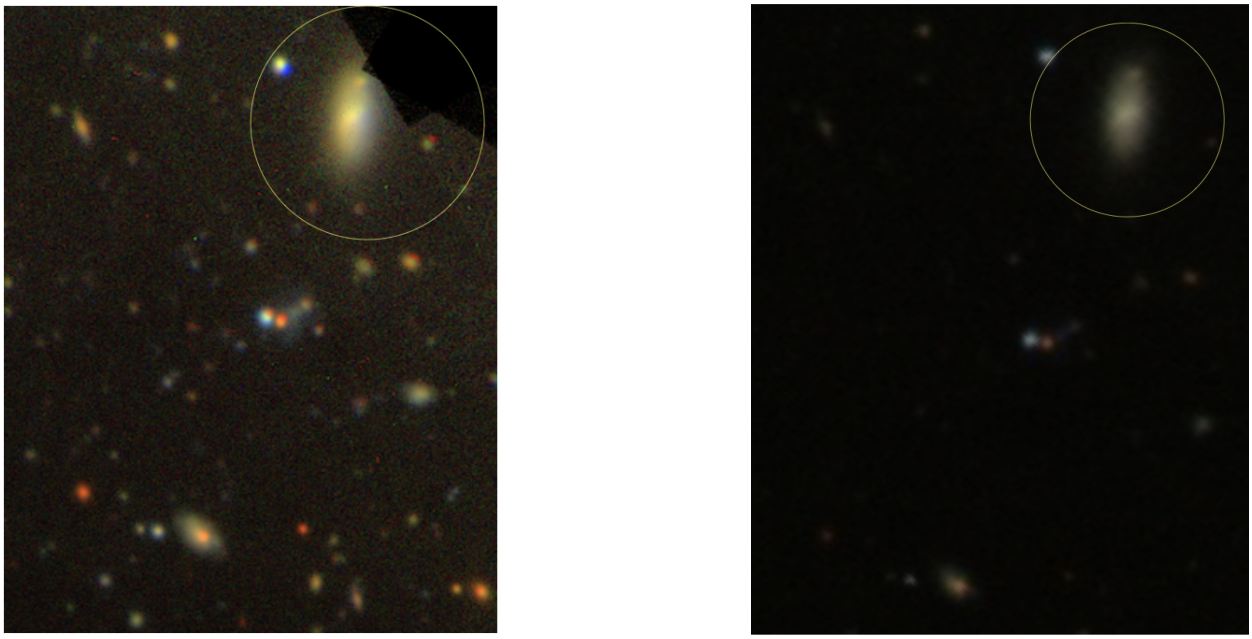

Figure 3.3: Left panel: LEDA 1139929 with GTC. Right panel: LEDA 1139929. Aladin Lite, SDSS9.

Table 3.1: LEDA 1139929 fluxes

Filter Name	System	Magnitude
u	AB	19.34
g	AB	17.92
r	AB	17.28
i	AB	16.97
z	AB	16.75

reported in Table 3.2. Also in this case, I remark the difference between the quality of the image I took with GTC and the one from the Aladin Lite database.

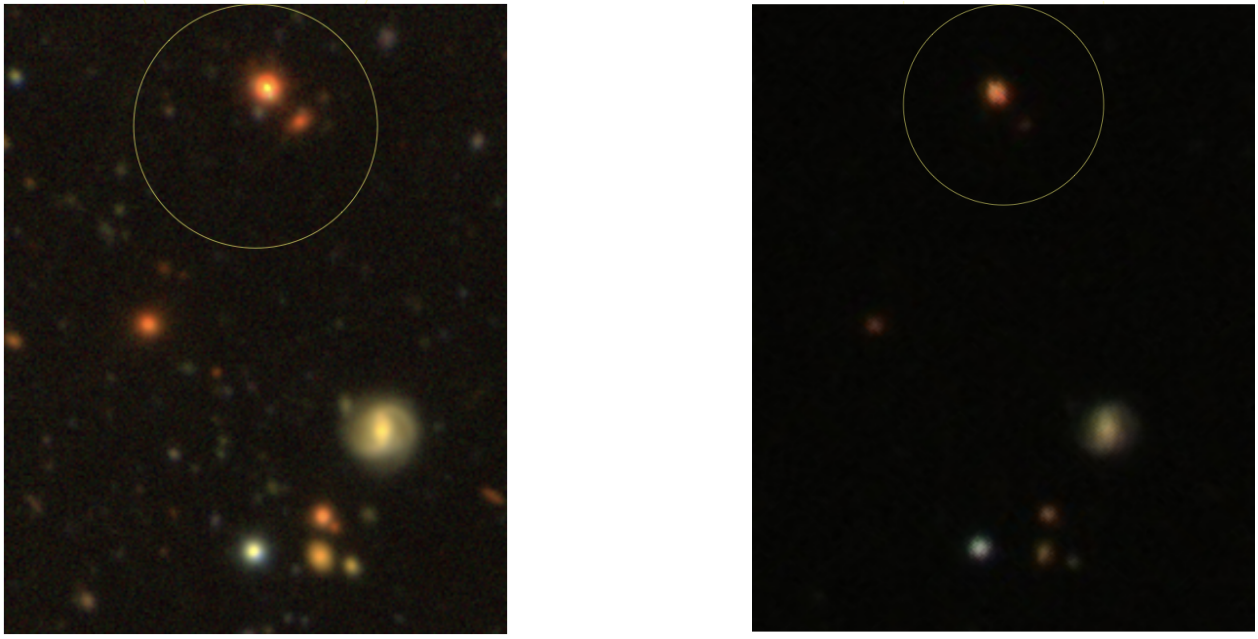

Figure 3.4: Left panel: SDSS J012329.48-003552.8 with GTC. Right panel: SDSS J012329.48-003552.8. Aladin Lite, SDSS9.

Table 3.2: SDSS J012329.48-003552.8 fluxes

Filter Name	Flux value
G	18.45
J	15.74
H	15.10
K	14.88
u (AB)	23.04
g (AB)	20.35
r (AB)	18.93
i (AB)	17.72
z (AB)	17.08

Then I explored the same field of view with the GAIA DR2 archive and I found the following point-like sources exposed in Table 3.8. I placed on these sources a black circle as shown in Figure 3.5.

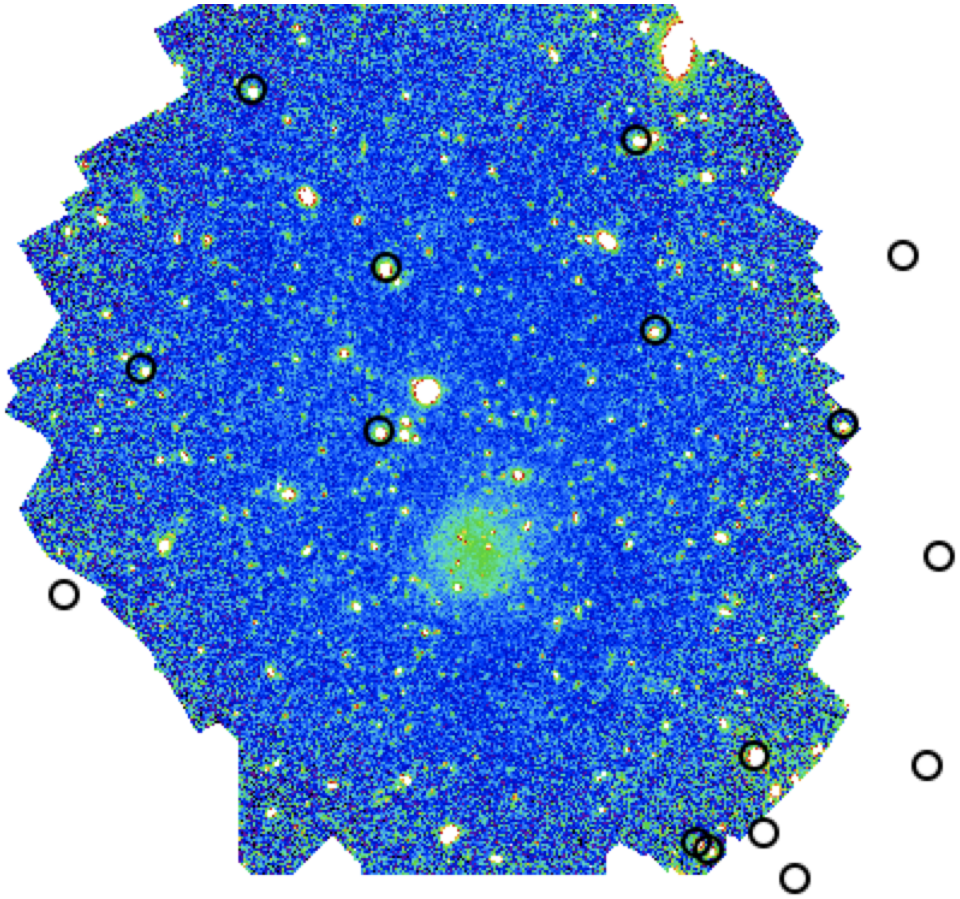

Figure 3.5: GAIA DR2 Sources around $RA = 20.86418538$h and $DEC = -0.6229532711$, r′ filter. Black circles identify sources cataloged with GAIA DR2. SAOImageds9. Scale Log 99.5%, color:sls.

Table 3.3: GAIA DR2 Catalog

RA(J2000)	DEC(J2000)	Source ID	Gmag
020.9025395072829	-00.6281115390112	2533918936706349952	20.49
020.8379554518116	-00.6502640153133	2533921341887779328	19.93
020.8226822720390	-00.6439076947367	2533921406312769408	19.35
020.8386928856903	-00.6430611445533	2533921406312769792	17.34
020.8349159706833	-00.6543319726219	2533921337593288576	20.47
020.8440700378053	-00.6510556169830	2533921337593289472	19.72
020.8428822103694	-00.6517330737804	2533921337593289216	20.31
020.8216918060778	-00.6246061399518	2533921715550420736	18.63
020.8305865380405	-00.6124302564707	2533921818629638400	19.61
020.8728083688965	-00.5980207534119	2533921956068595584	18.45
020.8734375974515	-00.6131087382418	2533921960363668864	19.34
020.8953904910034	-00.6072243501922	2533921990428331264	19.69
020.8497214891504	-00.5861633466892	2533922230946506368	20.21
020.8479289452714	-00.6036679356685	2533922127867285760	19.23
020.8852569084221	-00.5814720227260	2533922299665985280	20.26
020.8249104346250	-00.5969288084072	2533922574543886848	19.09

After that, I did the same with the astronomical survey 2MASS (Two Micron All-Sky Survey) in the infrared. Here, black circles in Figure 3.6 identify the 2MASS sources of Table 3.8.

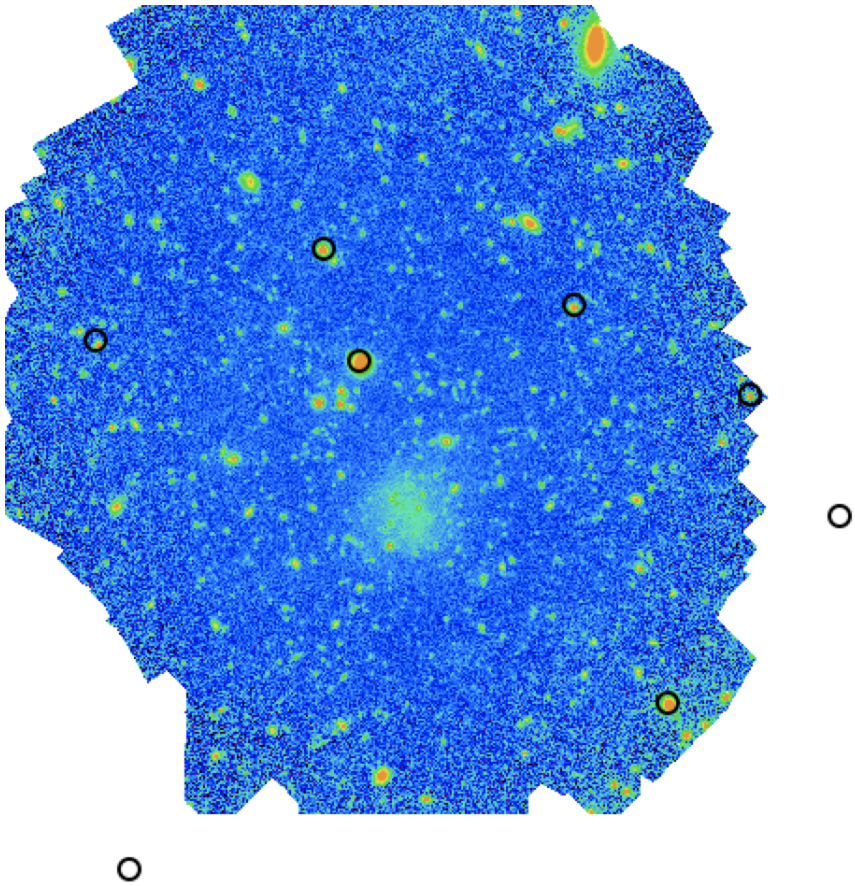

Figure 3.6: 2MASS Sources around $RA = 20.86418538$h and $DEC = -0.6229532711$, r′ filter. Black circles identify sources cataloged with 2MASS. SAOImageds9. Scale Log 99.5%, color:sls.

Table 3.4: 2MASS Catalog

RA(J2000)	DEC(J2000)	Source ID	Jmag
020.83869800	-00.64306200	01232128-0038350	15.35
020.89199500	-00.65950900	01233407-0039342	16.16
020.83059600	-00.61247200	01231934-0036448	16.81
020.87280700	-00.59805600	01232947-0035530	15.74
020.84794500	-00.60368200	01232350-0036132	16.08
020.82171300	-00.62459000	01231721-0037285	16.09
020.86927600	-00.60924800	01232862-0036332	16.89
020.89537100	-00.60724300	01233488-0036260	16.36

3.1.1 Point Spread Function (PSF)

The spatial (and angular) distribution of the light collected from a point source (star) on CCD is described with the Point Spread Function (PSF). The quality of the PSF of a ground based image can be worsened due to the turbulence of the upper atmosphere, to diffraction and aberrations of the optical system. As a matter of fact, when the light coming from a source pass trough the different layers of the atmosphere, it changes its path depending on the refractive index of the layer and hence arrive at different places on the detector. The PSF in its central part (core), is well approximated by a Gaussian profile:

$$f(r) = Ae^{\frac{-(x-\mu)^2}{2\sigma^2}} + d \tag{3.1}$$

with a FWHM=$2\sqrt{2ln2}\sigma$. I remark that this approximation is correct within the Full Wight at Half Maximum (FWHM), which is the distance between the points where the flow of the source decays by half with respect to its maximum value. However, along the wings of the distribution, the two functions are significantly different and, in particular, the Gaussian profile is sharper. Therefore, it is possible to build a Moffat function with radial parameter α to have a better fit:

$$f(r) = a[1 + (r/\alpha)^2]^{-\beta} \tag{3.2}$$

with FWHM=$2\alpha\sqrt{2^{1/\beta} - 1}$.

Figure 3.8 reports the typical PSF slope of a selected star in my field of view (the one in Figure 3.7). Even if it does not completely describe the PSF, the FWHM is the key parameter to characterize its angular dimension. For what concerns this study, the FWHM is $\sim 0.8\ ''$ distributed on an area covering 10 pixels. This number pixels guarantees that there is no sub-sampling and an eventually inaccurate evaluation of the FWHM.

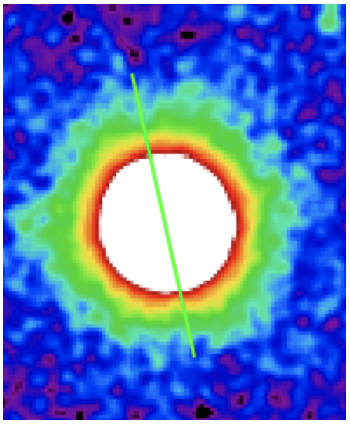

Figure 3.7: Gaiadr2 star 2533921337593288576 to characterize the PSF. SAOImageds9. Sls colors, scale Log, 99.5%

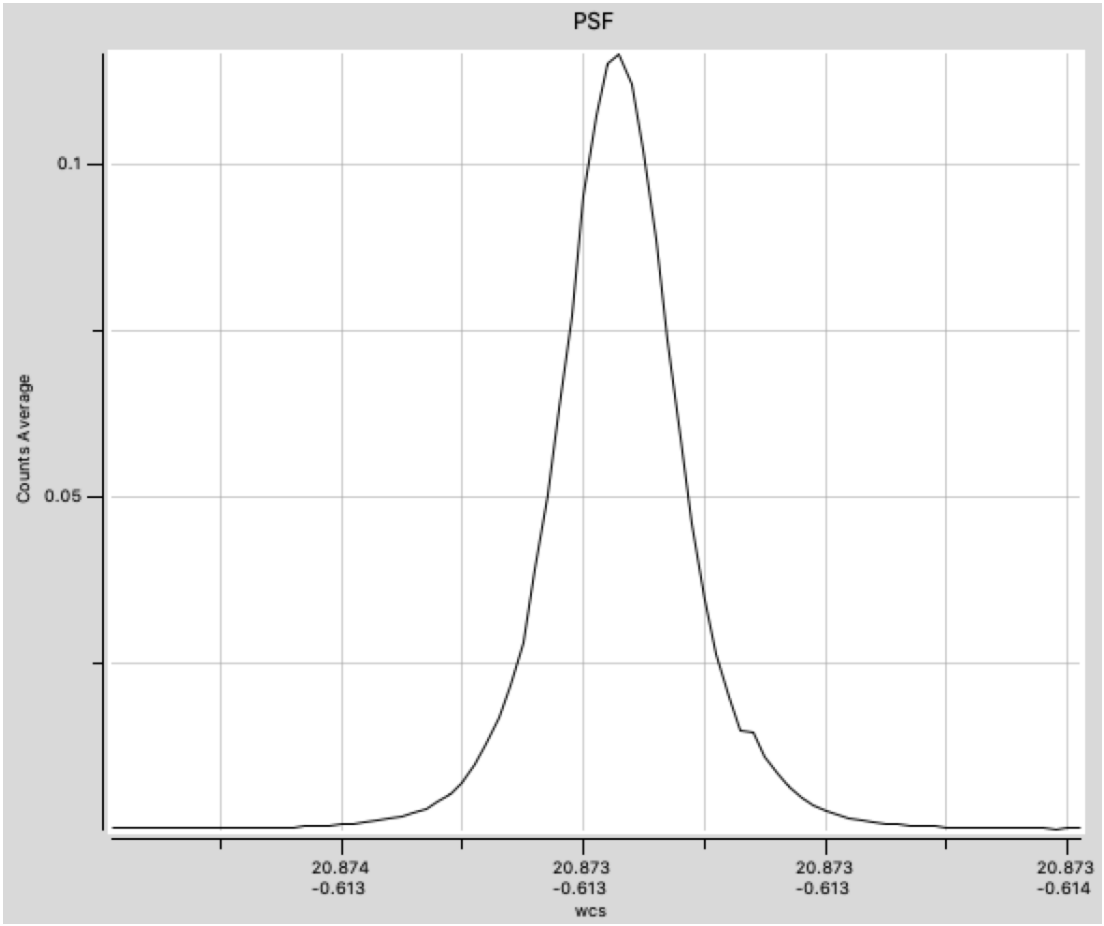

Figure 3.8: Surface brightness profile relative to the Gaiadr2 star 2533921337593288576. SAOImageds9.

3.1.2 Signal to noise ratio

The precision associated with a physical measurement is just as important as the measurement itself. The best way to indicate the accuracy of astronomical CCD measurements is the signal-to-noise ratio (SN). The higher the SN the better is the measure. Generally, the signal consists of the photons that come from a source while the real noise is the total random contribution from various sources: Shot Noise, Object noise, Sky Noise, Dark Noise and Read-out-noise. In fact, the CCD electronics introduces other contributions to noise such as the thermal noise due to the thermal agitation of pixel that produce an electric current and charge accumulation, and the read out noise (RN) introduced by the reading electronics (in particular the output pre-amplifier) whenever a pixel is read. In the case of an ideal detector, where the noise due to the electronics is negligible, the signal itself is subject to an intrinsic uncertain which can be quantified with the statistics of Poisson by using the number of detected photons (n):

$$\frac{S}{N} = \sqrt{n} \tag{3.3}$$

This is a theoretical limit and it is valid only when the number of source-photons collected is very large (source-limited case). However, when observing faint astronomical objects, the background-sky emission is the major source of error (sky-limited case). In addition, the sky noise and the source noise become the dominant contributors as the integration time increases. All these random, uncorrelated noises add quadratically and lead to the following (simplified but quite accurate) formula for the signal-to-noise ratio:

$$\frac{S}{N} = \frac{N_s t_{exp}}{\sqrt{N_s t_{exp} + n_{pix}(N_b t_{exp} + N_d t_{exp} + N_r^2)}} \tag{3.4}$$

where

- N_s is the number of photons (signal) per pixel collected from the target;
- N_d is the number of photons per pixel due to dark current;
- N_b is the number of photons per pixel of the sky background;
- N_r is the number of photons per pixel due to the Read out Noise;
- t_{exp} is the exposure time;
- n_{pix} is the number of pixels involved in the calculation of noise terms.

Both for bright sources and faint sources SN is proportional to $\sqrt{t}$. The Hipercam camera has N_r of 4.5 electrons and N_d equal to 100 electrons/pixel/hour. To compute the effective time on source I checked with *astarithmethic* the number of individual images that I summed up to build the final image of the galaxy. It leads to $t_{exp} \sim 3600s = 1$h. In this case I obtained SN = 20, the error associated to the magnitude is:

$$\sigma(m) = \pm 2.5 log(1 + 1/SN) \tag{3.5}$$

so the relative error is about $\sim 5\%$.

3.1.3 Image visualization

The Histogram of the pixel values is a useful way to have a quick look on the main properties of the astronomical image. Figure 3.9 presents the characteristic slope of the histogram of the r′ co-added image of the galaxy. The distribution is peaked in proximity to the median value, which corresponds to the background value ($\sim 9 \cdot 10^{-5}$). Moreover, there are few defective pixels with lower values than the mean one and there are pixels with greater values that coincide with real sources.

```
Input: stacked-r-filter.fits (hdu: 1)
-------
  Number of elements:                     10932634
  Minimum:                                -0.0179356
  Maximum:                                0.908321
  Median:                                 9.05403e-05
  Mean:                                   0.0001468827782
  Standard deviation:                     0.002198130468
-------
Histogram:
 | *
 | *
 | *
 | *
 | *
 | *
 | *
 | *
 | *
 | *
 |****************************************** ******** ******* ******
 |-------------------------------------------------------------------
```

Figure 3.9: Histogram of r′ co-added image. Number of pixels with a given intensity on the y-axis with respect to the value of the intensity on x-axis.

I report here in Figure 3.14, from the top to the bottom, the stacked final images of the target galaxy observed with u′, g′, r′, i′, z′ filters respectively.

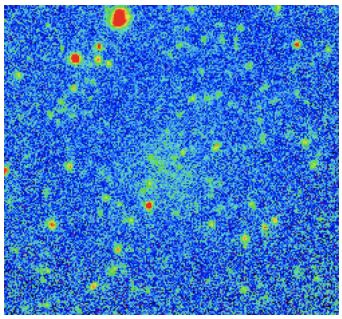

Figure 3.10: Stacked u′ final image of the galaxy. SAOImageds9. Sls colors, scale Log, 99.5%

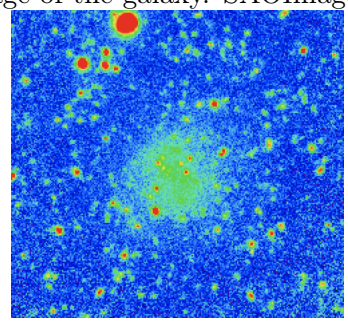

Figure 3.11: Stacked g′ final image of the galaxy. SAOImageds9. Sls colors, scale Log, 99.5%

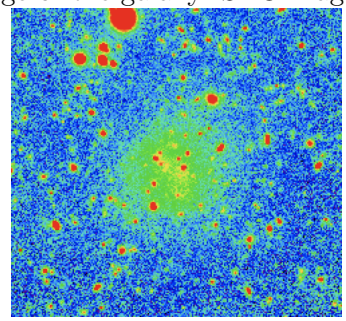

Figure 3.12: Stacked r′ final image of the galaxy. SAOImageds9. Sls colors, scale Log, 99.5%

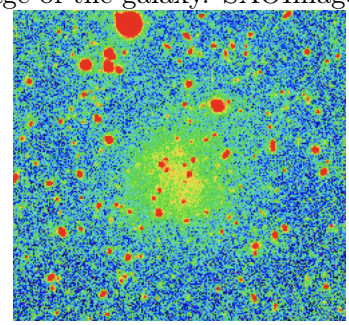

Figure 3.13: Stacked i′ final image of the galaxy. SAOImageds9. Sls colors, scale Log, 99.5%

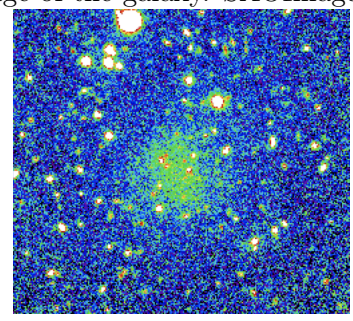

Figure 3.14: Stacked z′ final image of the galaxy. SAOImageds9. Sls colors, scale Log, 99.5%

3.1.4 Magnitude and Surface brightness of the galaxy

I determine the u′, g′, r′, i′, z′ magnitudes of the target through the construction of a mask which is quite representative of its shape and large enough to include the majority of the halo component in order to do an accurate estimate of the total flux. To find the total brightness I need to integrate the light coming from all parts of the galaxy, therefore I identified and added only the values of the pixels that contain the galaxy emission. If I build a different mask for each filter, the final brightness value may not be correct, since for example, the galaxy u′ filter emission can appear less noticeable than g′ (or than the remaining filters). To pass this problem I build a deeper mask by combining the final images of g′ r′ and i′ with a mean. The mean of g′ r′ and i′ is highlighted on the left panel of Figure 3.16.

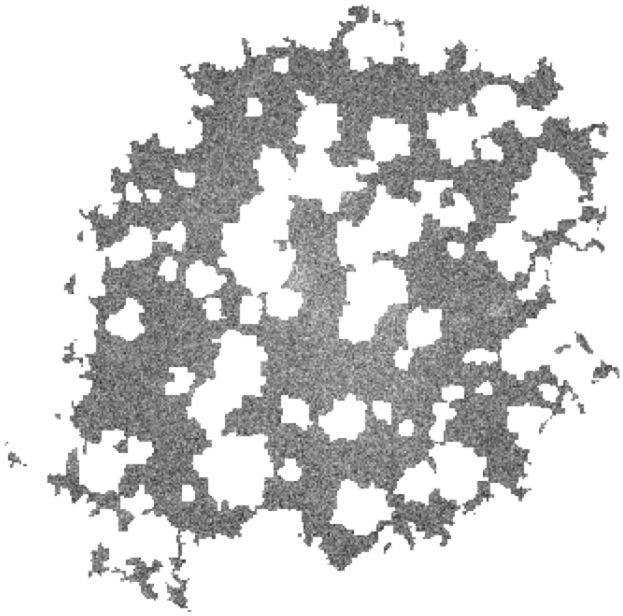

Figure 3.15: Masked galaxy, G-filter. Scale Log, 99.5%, grey colors, SAOImageds9.

After that, I confine the target source with a generic polygon figure (see right panel of Figure 3.16) to remove the noise that could make Astnoisechisel not work well when building the mask. Building a perfect representative mask around an ultra diffuse object is not easy because I have to identify the bright astronomical objects in front of (or behind) the target and I must not confuse the halo of the galaxy with the sky background. To do this I play with Astnoisechisel parameters (such as tilesize), I build a kernel Gaussian function to improve Astsegment to detect any clumps and objects of the image, I substitute any blank pixels with Nans and I erode the "rivers" between clumps that can affect the magnitude estimate. Finally, I apply this deep mask to all co-added final images (the same mask to each filter). The result of this effort is shown in Figure 3.15, where the colored part is galaxy and the white part covers Nan pixels. The mask has a final diameter of $\sim 34''$. At this point, considering that the area covered by Nans pixels is lost galaxy emission, I attribute the average value among the pixels that have not been masked to the "empty" pixels. In this manner

I can estimate, even if approximately, the emission lost due to the masking process. This emission is take into account and add to the estimate of the brightness value, which would otherwise be underestimated. Then I calculate the apparent mean magnitudes of the galaxy as:

$$m_\lambda = -2.5 log_{10}(S_\lambda) + z_p \tag{3.6}$$

where S, the sum of the pixel values belonging to the galaxy, is computed with aststatistcs and corresponds to the flux of the galaxy. I decide to use a zero point z_p equal to 22.5 (as Sloan). The values that I have estimate are: $m_{u'}$=18.975, $m_{g'}$=18.810, $m_{r'}$=18.101, $m_{i'}$ =17.844 and $m_{z'}$=17.339.

The absolute magnitude instead, M_λ, can be easily found trough the distance modulus:

$$M_\lambda = m_\lambda + 5 - 5 log(d) \tag{3.7}$$

by assuming d, the distance of the UDG, to be roughly the distance of the Abell 194 cluster (∼100 Mpc). This distance modulus of 35 leads: $M_{u'}$=-16.45, $M_{g'}$=-16.52, $M_{r'}$=-17.13, $M_{i'}$ =-17.32 and $M_{z'}$=-17.72. After that, I compute the mean luminosity of the galaxy with the following formula:

$$L_\lambda = 10^{-0.4(M_\lambda - M_{\odot,\lambda})} \qquad [L_\odot] \tag{3.8}$$

where $M_{\odot,\lambda}$ is the absolute magnitude of the Sun at the given wavelength. This leads to: $L_{u'}$=2·10^8 $L_\odot$, $L_{g'} = 3 \cdot 10^8$ $L_\odot$, $L_{r'} = 5 \cdot 10^8$ $L_\odot$, $L_{i'} = 6 \cdot 10^8$ $L_\odot$, $L_{z'} = 9 \cdot 10^8$ $L_\odot$. Finally, I have to take into account the galactic extinction: it is the reduction of light coming from distant astronomical sources caused by the absorption of radiation by very small dust grains (with a diameter of ∼1 μm) in the interstellar space. These grains of dust and gases weaken the blue light more than the red one and therefore the final light intensity received by the observer will be different with respect to the real value. The galactic extinction A(λ) is measured in magnitudes and its value changes as a function of the wavelength and it is color dependent. Therefore, I correct each magnitude of galactic extinction by using the coefficients found at NED website. I report in the following Table 3.5 these coefficients and the corrected-magnitudes of this UDG.

Table 3.5: Extinction coefficients at $RA = 20.86418538$h and $DEC = -0.6229532711$ and corrected magnitudes of the target galaxy.

Filter Name	Extinction coefficient	m-corrected
u′	0.429	18.54
g′	0.335	18.47
r′	0.232	17.86
i′	0.172	17.67
z′	0.128	17.27

The surface brightness of an astronomical source is the radiative flux per unit solid angle (Ω) subtended by the source and it is generally defined as:

$$SB = \frac{Flux}{\Omega} \qquad [L_\odot / pc^2] \tag{3.9}$$

However, in the optical regime, it is preferable to express the surface brightness as:

$$SB = -2.5log_{10}(\frac{Flux}{\Omega}) + Cost \qquad [mag/arcsec^2] \tag{3.10}$$

It is worth noting that, the surface brightness of an extended object in Local universe (flat and static universe approximation) does not depend on distance since Flux and Ω are proportional to $1/r^2$.

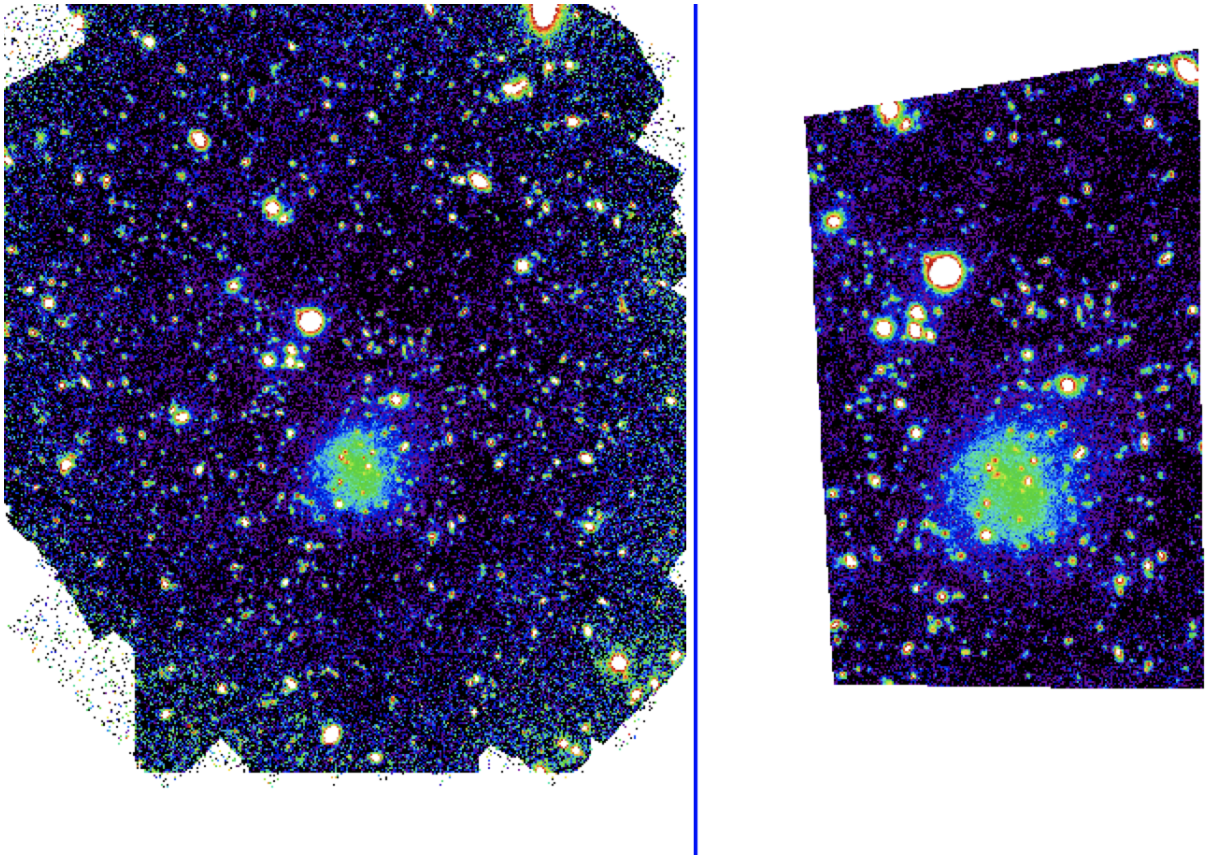

Figure 3.16: Left panel: Deep Image of the target galaxy obtained by mediating g′ r′ and i′ co-added images. Right panel: Cropped deep image. Scale Log, 99.5%, sls colors, SAOImageds9.

For what concerns this thesis, I estimate the surface brightness μ_λ with the formula:

$$\mu_\lambda = -2.5log_{10}(\frac{S_\lambda}{A}) + z_p \qquad [mag/arcsec^2] \tag{3.11}$$

and I measure the area on which the galaxy rests as:

$$A = N_{pixels} \cdot d^2_{pixels} \qquad [arcseconds^2] \tag{3.12}$$

The pixel size d_{pixels} of Hipercam is $0.081''$. Galaxies are diffuse objects and have no well-defined edges so their brightness is much harder to measure than stellar luminosity. I assumed the diameter of the galaxy to be approximately $34''$, so the resulting mean surface brightness values are: $\mu_{u'} = 27.39\, mag/arcsec^2$, $\mu_{g'} = 26.99\, mag/arcsec^2$, $\mu_{r'} = 26.31\, mag/arcsec^2$,$\mu_{i'} = 26.11\, mag/arcsec^2$,$\mu_{z'} = 25.76\ mag/arcsec^2$. The error which is associated to the surface brightness measure is 0.5 $mag/arcsec^2$. Table 3.8 reports the mean of the pixels values, the apparent and absolute magnitude,

the luminosity and the mean surface brightness of the galaxy of each optical band. Since the

Table 3.6: UDG galaxy results

Filter Name	Mean to substitute	$\mu(mag/arcsec^2)$	m	M	L($L_\odot$)
u′	0.00007	27.39	18.54	-16.45	$2 \cdot 10^8$
g′	0.0001	26.99	18.47	-16.52	$3 \cdot 10^8$
r′	0.0002	26.31	17.86	-17.13	$5 \cdot 10^8$
i′	0.0002	26.11	17.77	-17.32	$6 \cdot 10^8$
z′	0.0003	25.76	17.27	-17.72	$8 \cdot 10^8$

surface brightness is ranging from 27.39 $mag/arcsec^2$ to 25.76 $mag/arcsec^2$, I can confirm that the astronomical object under exam is an Ultra Diffuse Galaxy.

Figure 3.17 highlight with light blue color the mean surface brightness profile of this UDG, the orange straight line in the graph represents the linear fit to data (see Table 3.7), that are colored light blue, and they are shown with relative error bars. This analysis of surface brightness values with increasing distance from the center of the galaxy is done manually and with Python Programming Language.

Table 3.7: UDG data to fit the surface brightness profile.

r (arcseconds)	r (kpc)	$\mu(mag/arcsec^2)$
0.8	0.37	25.62
4.5	2.0	25.84
8.0	3.7	26.00
12.04	5.5	26.34
13.6	6.3	26.46
15.37	7.1	27.04
18.18	8.4	27.79

The projected surface brightness profile of galaxies usually shows an exponential fall off with radius which can be described with the following relation:

$$\mu_r = \mu_0 \cdot 1.086(r/h) \tag{3.13}$$

Here, h is the scale length of the exponential light fall off and μ_0 is the central surface brightness of the galaxy. The linear polynomial fit to data leads to $\mu_0 = 22.0$ $mag/arcsec^2$ r-band and a scale height (h) of -1.2 pc. The slope of this brightness profile presents a cut off at $\mu_{co} \sim 26.3$ $mag/arcsec^2$ corresponding to a radius of ~ 6 kpc.

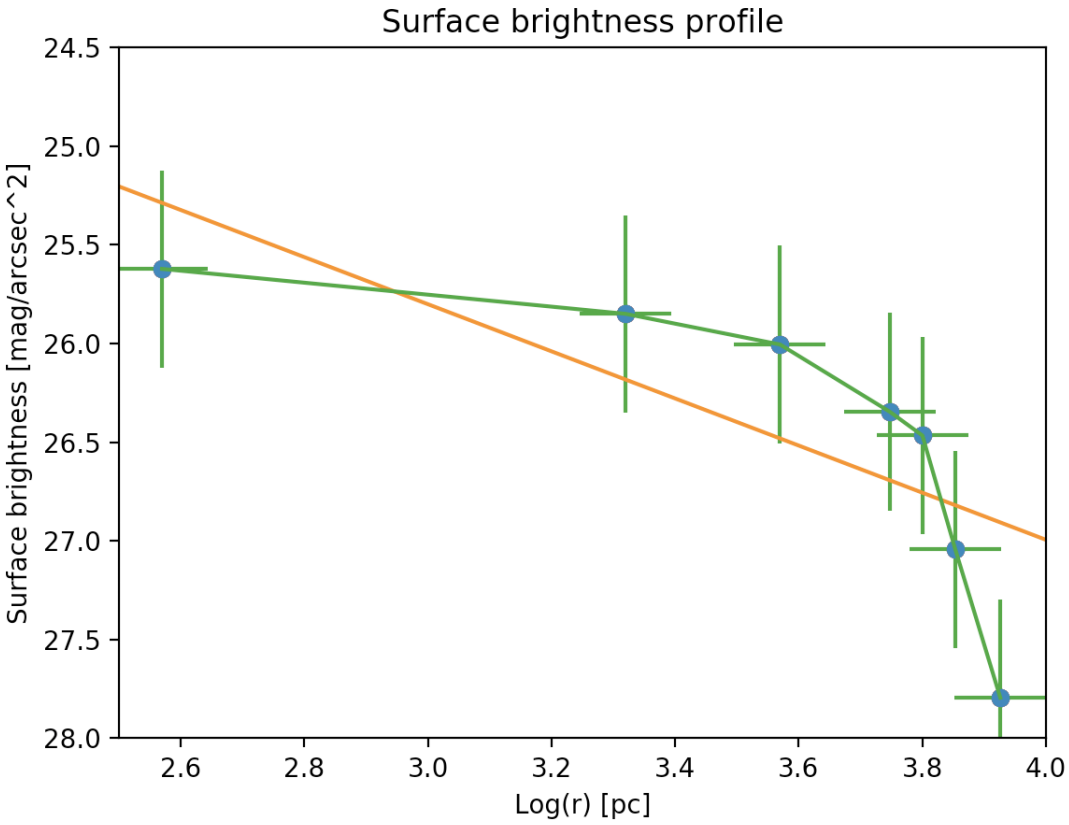

Figure 3.17: Mean surface brightness profile of the UDG. Surface brigthness ($mag/arcsec^2$) as a function of log(r) measured in pc. Light blue dots identify the data with relative errors. The orange straight line is the linear fit to data.

In order to compare the properties of this UDG with those of other galaxies, I also fit Sersic functions to its surface brightness profile. The Sersic profile assumes the following formulation in logarithmic form:

$$\mu_r = \mu_0 + c_n((\frac{r}{r_e})^{1/4} - 1) \tag{3.14}$$

where μ_0 is the central surface brightness, r_e is the effective radius, n is the Sersic index and c_n is a parameter which depends on n. For n = 0.5 the law $r^{1/4}$ assumes a Gaussian trend, for n = 1 it takes the form of an exponential law, while for n = 4 we obtain the de Vaucouleurs law. The Sersic n index grows with brightness and it allows us to characterize disk galaxies (if n $\sim$ 1), elliptic galaxies (if n = 1.5-20) or bars (n $\sim$ 0.5). Figure 3.18 shows the best $r^{1/4}$ fit to the ultra-diffuse galaxy analyzed in this study. The fit leads to an estimate of central surface brightness of $\mu_{r,0}$ = 26 $mag/arcsec^2$, an effective radius of 4.5 kpc and a Sersic index of 0.3.

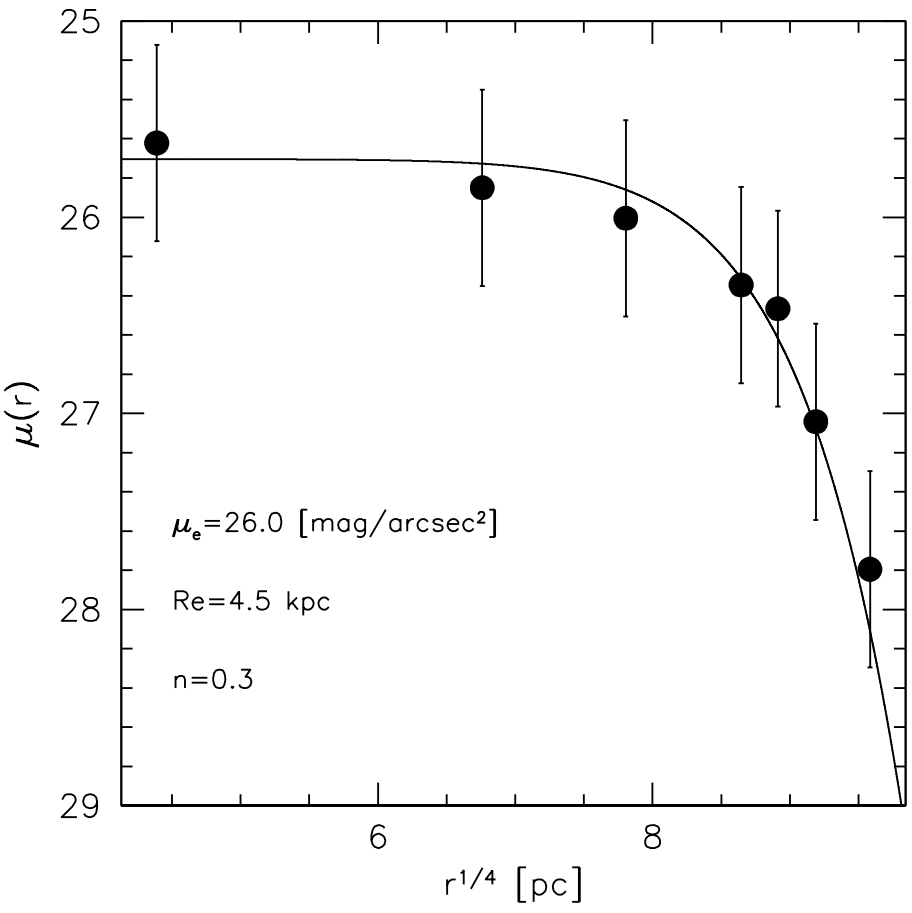

Figure 3.18: Sersic profile to UDG data. The best fit leads to μ_0 = 26 $mag/arcsec^2$, re = 4.5 kpc, n= 0.3.

3.1.5 Colors

To rapidly understand what is the stellar population that predominates the galaxy I calculate the difference of its magnitude in two different bands, which is equal to the quotient between the two intensities of the corresponding bands. In the case of g′ and i′ it means to compute:

$$m_G - m_I = 2.5log\frac{f_I}{f_G} \tag{3.15}$$

A high color value indicates a greater emission power in the infrared than in the blue one, young stars appear blue and old stars red. I report in Table 3.8 the main colors of the UDG.

Table 3.8: Colors of the UDG located at $RA = 20.86418538$h and $DEC = -0.6229532711$.

Color	Value
u′-g′	0.071
g′-r′	0.605
r′-i′	0.196
i′-z′	0.410
g′-i′	0.802

3.1.6 Spectral energy distribution

The graph of the energy emitted by an object as a function of different wavelengths is the spectral energy distribution (SED). For this instance I report the SED relative to the u′, g′, r′, i′ and z′ brightness of the UDG galaxy (at 3580, 4754, 6204, 7698 and 9665 respectively) in Figure 3.19, with relative error bars. The light blue dots identify the fluxes before the correction of galactic extinction while orange dots indicate the corrected fluxes.

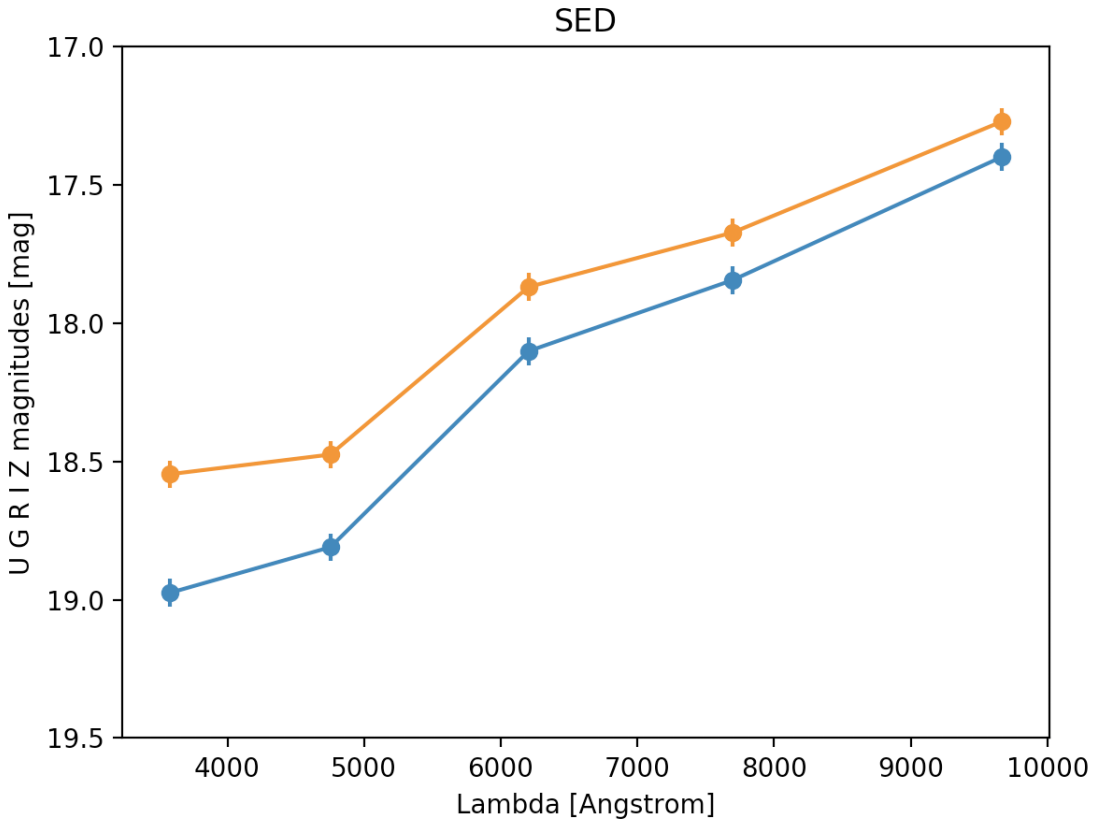

Figure 3.19: Spectral energy distribution of the target UDG. Light blue dots identify the values of the computed magnitudes, error bars colored light blue. The orange dots are the extinction corrected values of magnitudes with relative error bars.

3.1.7 Mass to Luminosity ratio

To determine the plausible Mass to Luminosity ratio (M/L) I compare the spectral energy distribution of the ultra diffuse galaxy with the photometric predictions generated by the Vazdekis et al.(2010) code based on the E-MILES SEDs. I use the Chabrier PADOVA+00 isochrone of the SSDSs predictions (AB system). To do this comparison I write a Python routine to find out what is the best fit according to the χ^2 minimization. I assume that the galaxy has a single stellar population and that the models provide a good match to the data. The best model, with $\chi^2 = 0.4$, is light blue colored in Figure 3.20. It leads to $log(M/L)_u = 0.05$, $log(M/L)_g = 0.09$, $log(M/L)_r = 0.13$, $log(M/L)_i = 0.12$, $log(M/L)_z = 0.11$.

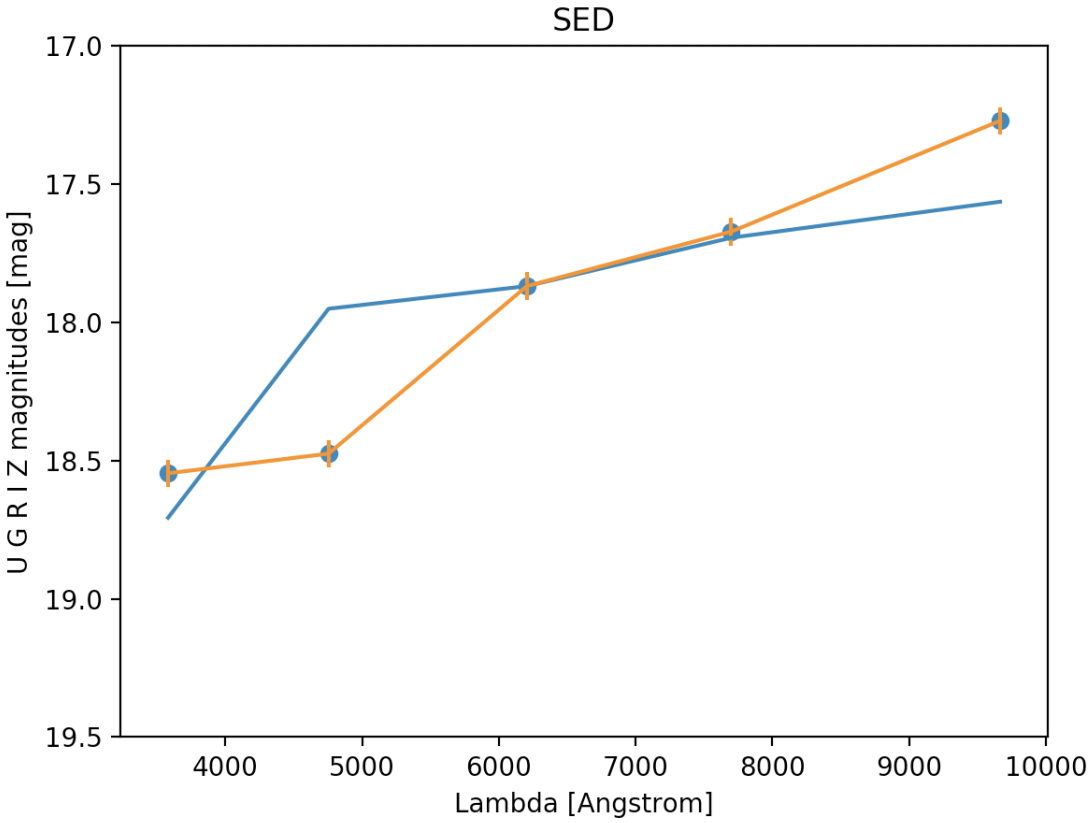

Figure 3.20: Spectral energy distribution of the target UDG. Orange dots identify the values of the computed magnitudes, error bars colored orange. The Chabrier PADOVA+00 isochrone which fits the distribution of the corrected magnitudes is colored light blue.

3.1.8 Stellar mass density

The stellar mass density profile (Σ) of the galaxy is estimated by applying the following formula from Bakos & Trujillo (2008):

$$log(M/L)_\lambda = a_\lambda + b_\lambda(g' - r')) - 0.15 \tag{3.16}$$

$$log(\Sigma) = log(M/L)_\lambda - 0.4(\mu_\lambda - m_{abs,\odot,\lambda}) + 8.629 \qquad [M_\odot/pc^2] \tag{3.17}$$

where μ_λ and $m_{abs,\odot,\lambda}$ are respectively the surface brightness of the UDG and the absolute magnitude of the Sun at a given wavelength λ. I decide to refer calculations to r$'$ band, so then:

$$log(M/L)_{r'} = (-0.306 + 1.097(g' - r')) - 0.15 \tag{3.18}$$

$$log(\Sigma) = log(M/L)_{r'} - 0.4(\mu_{r'} - 4.68) + 8.629 \qquad [M_\odot/pc^2] \tag{3.19}$$

Since g$'$-r$'$ = 0.605, then $log(M/L)_{r'} = 0.2$. Moreover, a $\mu_{r'}$ equal to 26.31 gives $\Sigma = 1.53\ M_\odot/pc^2$. Subsequently, I supposed the galaxy to be located at 100 Mpc (z = 0.0275), I approximate its diameter to $34''$ on image that, with a scale of 0.464 $kpc/''$, corresponds to 15.77 kpc. I assumed the galaxy to be circular, then its area is $1.95 \cdot 10^8\ pc^2$. Finally, the assessed stellar mass value is $\sim 3 \cdot 10^8 M_\odot$.

Discussion

The aim of this study is to investigate the limits in the surface brightness photometry of galaxies. Despite numerous advances, such as the discovery of UDGs with William Herschel Telescope in the Perseus cluster and in the massive galaxy cluster Abell 2744 with the Hubble Frontier Fields program, nowadays still little is known about what concerns the faint universe under the night sky brightness. Weak astronomical objects are challenging to be observed and it is even more complex with ground based telescopes. As a matter of fact, galactic cirrus, optical aberrations and atmospheric turbulence are just few of the factors that can make harder and more difficult the detection of faint sources. Therefore, more and more effort is required by astronomers and experts to go beyond these limits. The effort, however, will be worth and it will be rewarded in discovering a huge amount of galaxies with various masses and sizes and with different star formation histories that could allow us to understand more deeply the origin of the Universe. We may finally be able to "give light" to dark matter, to analyze the relative abundance of light and matter in the universe and to fill those gaps between observations and theoretical models that have not yet been fixed, such as the faint end slope of the galaxies' luminosity function. Moreover, there are numerous theories that aim to understand the origin of low surface brightness galaxies but, to date, no one is definitive. Maybe the discovery of faint astronomical objects would clarify the ideas, maybe it would lead to an even greater confusion but it is very important to go further and not being fulfilled. To contribute to this topic, I built a data reduction pipeline which is supposed to be a starting point for future researches and for the improvement of data analysis of very faint objects. This pipeline allows obtaining excellent image resolution, even better than that of recent surveys as Sloan.

In particular, I inquired into the nature of a very faint astronomical object located at $RA = 20.86418538$h and $DEC = -0.6229532711$ in the Abell 194 cluster, that was detected with the Stripe82 Legacy project by Fliri & Trujillo. The target was observed with GTC telescope at La Palma using the Hipercam camera, a quintuple-beam imager that records u′, g′, r′, i′, z′ (from 300 nm to 1000 nm) images simultaneously on its CCD cameras. The raw images coming from the telescope were then processed with this new and optimized pipeline, which I developed at IAC at La Laguna (Tenerife) under the supervision of the researchers I. Trujillo and R. Infante-Saint. To set up the pipeline I used Make and Python programming languages. This target is found to be an ultra diffuse galaxy with u′, g′, r′, i′, z′ mean surface brightness values of 27.39 ± 0.5 $mag/arcsec^2$, 26.99 $\pm 0.5 mag/arcsec^2$, 26.31 ± 0.5 $mag/arcsec^2$, 26.11 ± 0.5 $mag/arcsec^2$, 25.76 ± 0.5 $mag/arcsec^2$ respectively and whose stars are not resolved. These values of magnitudes can be considered reliable since the 10.4 m GTC telescope provides imaging with a limiting surface brightness of 31.5 $mag/arcsec^2$ r-band. However, measurement uncertainties are proved to be very

large due to the masking process and, until a deeper and more precise photometric analysis will be done, I want to keep this discussion more general. The galaxy covers an area of $\sim 34''$ in diameter on image, but it is very difficult to establish its edges. The apparent values of magnitude, corrected of galactic extinction, are $m_{u'}$=18.54, $m_{g'}$=18.47, $m_{r'}$=17.86, $m_{i'}$ =17.67 and $m_{z'}$=17.27. The accuracy of magnitude measurement is ∼5%. To compute the distance modulus of the galaxy I supposed that it is located at 100 Mpc, which is approximately the distance of the Abell 194 cluster. This assumption leads to absolute magnitude values of $M_{u'}$=-16.45, $M_{g'}$=-16.52, $M_{r'}$=-17.13, $M_{i'}$ =-17.32 and $M_{z'}$=-17.72. The color g′-i′ of this UDG is 0.8, this is a number that make me suppose a great emission power in the infrared and an old stellar population.

These data are similar to those of the study by Bergmann (2003) carried out with the Hobby-Eberly telescope that shows the existence of a huge number of red faint galaxies in the universe. Moreover, the range of magnitudes of this ultra diffuse galaxy is nearly the same of that of the UDGs found by Janssens (2016) in the ABELL 2744 cluster. In addition, to support these results, the astrophysicist Roman (2019) reports the discovery of a red ultra diffuse galaxy ($\mu_{g'}$ = 25.7 $mag/arcsec^2$; g′-i′ = 0.78 mag) located in a nearby cosmic void that is very similar to the one that I studied [63][64][65]. After that, through the comparison between the observed Spectral Energy Distribution of my target galaxy and theoretical predictions (MILES), I obtained an estimate of its Mass to Light ratios: $log(M/L)_u$ = 0.05, $log(M/L)_g$= 0.09, $log(M/L)_r$=0.13, $log(M/L)_i$= 0.12, $log(M/L)_z$=0.11. These results are compatible with the study of Zackrisson on low surface brightness galaxies that leads $log(M/L)$(V band) between 0.8 and 2. However, these values are low if they are compared with those of more massive faint galaxies such as Malin 1, whose baryonic mass to light ratio rises from $\log(M/L) \sim 0.4$ to ~ 0.7 in the u′ band.

All results are summarised in Table 3.9.

Table 3.9: Main characteristics of the UDG located at RA = 20.86418538h and DEC = −0.6229532711.

Filter	Ext.coefficient	m	M	Surface Brightness ($mag/arcsec^2$)	L($L_\odot$)	log(M/L)
u′	0.07	18.54	-16.45	27.39	$2 \cdot 10^8$	0.05
g′	0.60	18.47	-16.52	26.99	$3 \cdot 10^8$	0.09
r′	0.19	17.86	-17.13	26.31	$5 \cdot 10^8$	0.13
i′	0.41	17.67	-17.32	26.11	$6 \cdot 10^8$	0.12
z′	0.80	17.27	-17.72	25.76	$9 \cdot 10^8$	0.11

Finally, the surface stellar mass density of the galaxy, that I have analyzed, is approximately Σ = 1.53 $M_\odot/pc^2$. Since the galaxy has an area of $1.95 \cdot 10^8$ pc^2, I estimate a mass of $3 \cdot 10^8$ $M_\odot$ which is a typical value for UDGs. As a matter of fact, the study carried out by G. Martin et al.(2019) reports the discovery of ultra diffuse galaxies in Coma and Virgo cluster with similar masses. Figure 3.21 illustrates the mean surface brightness profile of the galaxy and compares it with the estimated surface brightness value of the sky (21.3 $mag/arcsec^2$).

The slope of the exponential brightness, marked green, shows a cut off at $\sim$ 26 $mag/arcsec^2$ (corresponding to r $\sim$ 6 kpc). Moreover, the orange-colored linear fit allowed me to evaluate the scale height (h) and the zero value of the exponential fall off (μ_0 r-band) to be respectively -1.2 and

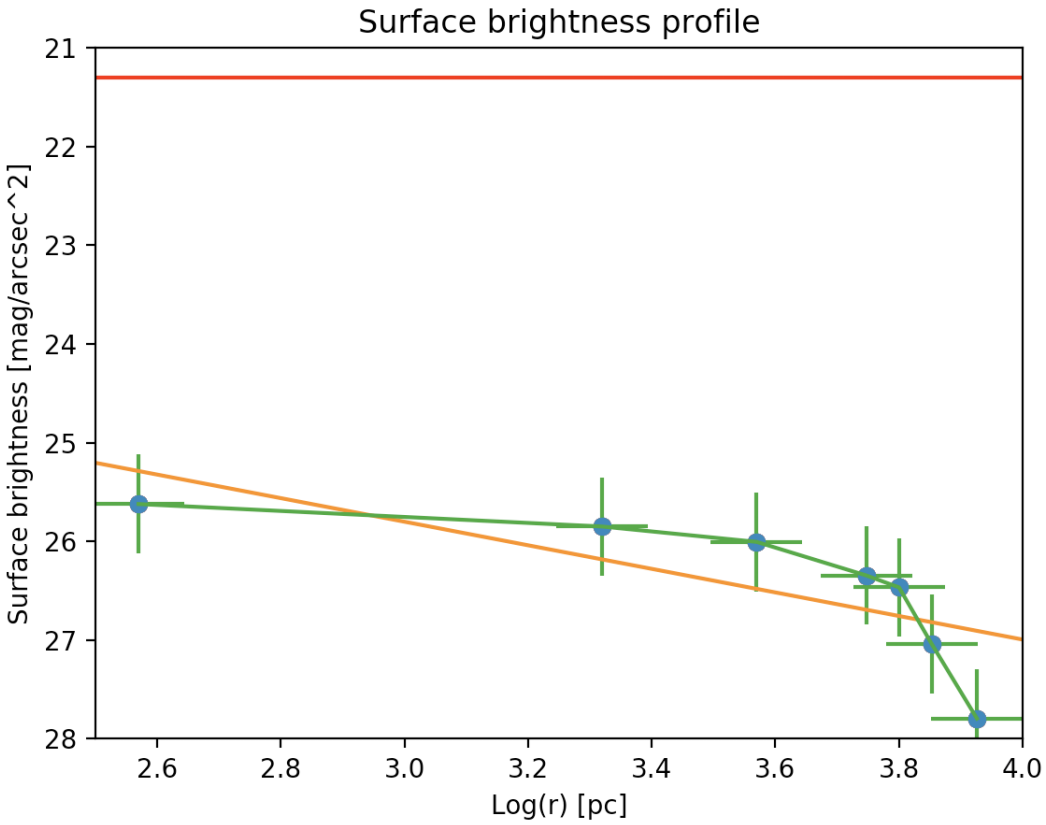

Figure 3.21: Mean surface brightness profile of the UDG. Surface brightness ($mag/arcsec^2$) as a function of log(r) measured in pc. Light blue dots identify the data with relative errors colored green. The orange straight line is the linear fit to data. The night sky emission is colored red.

22.0 $mag/arcsec^2$. To support of these results I report the study of Pahwa (2018); he found that by studying a sample of LSBGs observed by the Green Bank Telescope, the μ_0 is ≥ 21 $mag/arcsec^2$ in the r-band if the galaxies have a central disk, and a median central surface brightness value of 21.71 $mag/arcsec^2$ in the r-band if they are bulge-less faint galaxies. To have a better characterization of the structure of the UDG I fitted a Sersic profile to the surface brightness data. The best fit shows a $\mu_0 = 26$ $mag/arcsec^2$, an effective radius of 4.5 kpc and a Sersic index n of 0.3. Since r_e and n reveal the internal structure, they are also key parameter to understand the formation history of different types of galaxies. The value of the effective radius that I have found is compatible with the work of G. Martin et al. (2019) on low surface brightness galaxies and the low Sersic index make suppose a very faint barred galaxy. The work conducted by M. Gonzalez (2018) confirms that all LSB galaxies, even if in different environment, have Sersic index below 1. In particular, the galaxies detected in the direction of Pegasus I display a more restricted range of values ($0.44 \leq$ n ≤ 0.97). Liao et al. (2019) point out the difference between fitted projected surface brightness profiles for a UDG and a normal dwarf in the Auriga simulations; the UDG under exam presents $r_e = 4.57$ kpc, $\mu_{g,0} = 25.03$ $mag/arcsec^2$ and n = 0.54, while draft have generally greater Sersic indexes and lower effective radii.

Finally, it is clear that the galaxy brightness is far below the mean night sky emission (~ 21 $mag/arcsec^2$); in fact, in order to observe its features from the ground, it was necessary to use a telescope of 10.4 meters in diameter and, above all, an optimized reduction pipeline.

The result that I obtained through this thesis reflects the possibility of going ever beyond into the Universe and towards limits that we still do not know due to all the technological and physical problems related to the observations of faint sources in the sky. Although previous studies had already provided good successes, the present work complements the existing literature and it allows looking forward to future astronomical researches. It is important to note that this thesis has focused very much on the technical part of the data reduction process while the photometric analysis of the properties and of the characteristics of the galaxy remains subject to errors and it is approximate. With a more accurate study on the photometry of this galaxy, the current results could be different.

Future works

This pipeline is optimized for the Hipercam camera mounted at GTC telescope and it provides an excellent base to get better results when studying faint astronomical objects with ground based telescopes. Nevertheless, there are many aspects of the pipeline that could be improved.

First it must become completely automatic until the final image is built. Nowadays the pipeline is fully automatic up to the sky subtraction from the individual images, after which I execute step by step, one after the other, to obtain the final image. This choice was made to avoid and trace any bugs and to be able to work by reducing each filter separately in order to analyze each step and speed up the study. As a matter of fact the reduction process, from a computational point of view, requires long times (it takes around 2 hours with a 2,3 GHz Intel Core i5 processor computer). Furthermore, the Gnu Make programming language is relatively recent and has a logical and syntax structure that is very different from other programming languages such as Python: what is missing is understood how to set up the correct "pattern-match" to maintain the same data reduction structure before and after the separation of cube images into single-filter images.

Secondly, the problem of Flat Fielding. As already explained in Chapter 2, if during the nights of observation the environmental and atmospheric conditions suffer considerable variations, the way to combine all the individual images with sigma-clipping to build the master flat may not be representative and may lead to the formation of artificial structures on the final image of the target that could be confused with astronomical sources. It is therefore required to carry out a more accurate analysis to establish a criterion for evaluating whether it is better to use a master flat field built on dithering block observational images or on night block observational images or even again if it is better to use all the frames collected during the whole exposure time. This decision is not easy, a wrong choice can cause a loss in brightness resolution and very faint objects, that in one case could be observed, in the other case they could disappear. Moreover, it is important to examine whether it is necessary or not to capture more dithering block images in order to have a better characterization of the night sky brightness. I have also observed that, at this level of precision, it could happen that the software used for data analysis may not be able to mathematically identify with simple statistic the background fluctuations on smaller scales.

The third problem is that of the composition of band frames, namely the correct arrangement of the individual images of the four channels (E1,F1,G1,H1) of which the CCD is composed. Despite the accurate bias and flat correction, if you perform a convolution on the gain-corrected images, to be picky, you can still observe structures that recall the shape of the individual channels. Also in this case it would be required to conduct a more accurate analysis to define the number of columns that have to be used to estimate the average of the pixel values in order to calculate the exact correction

factor of which to multiply the individual channels.

The major source of error that I encountered, while deriving the brightness, was building the mask of the galaxy with Astnoisechisel. In fact, the galaxy is very faint and diffuse and therefore it is difficult to define what its edges are, where its halo ends and where the intergalactic medium begins on image. In addition, other sources of contamination (such as stars) may be located in front of or behind the galaxy. It is necessary to play with Noisechisel parameters (see Section C.2, Appendix C) to improve the masking process. Once the galaxy and the stars that are not part of it are masked, I replaced the pixels marked with Not a Number (NaN), that in any case belong to the galaxy, with the average of the unmasked pixel values which concern the galaxy. Even here, a more precise criterion should be defined to decide whether to replace the average or the median value and whether to take into account a possible error threshold or not.

I believe it would be important in the future to observe the object also in the infrared regime to deepen its star formation history. However, it is a very difficult task with current telescopes; as a matter of fact, the 2MASS provides a central surface brightness limit of $\sim 20\ mag/arcsec^2$ in K band, this means that the UDG should have at least $\sim 24\ mag/arcsec^2$ in B-band in order to be detected [66]. Maybe with new increasing technologies such as JWST and EUCLID it would be possible to have a broader view of the spectral energy distribution and to assess the nature of this galaxy.

Bibliography

[1] Chris Impey, Greg Bothun (1997) *Low surface brightness galaxies*

[2] van den Bergh (1959) *A Catalogue of Dwarf Galaxies*

[3] Beckwith et al. (2006). *HUDF*

[4] Gunn, J. E.; Knapp, G. R. (1993) *The Sloan Digital Sky Survey*

[5] Martınez-Delgado, D. et al. (2010) *Stellar Tidal Streams in Spiral Galaxies of the Local Volume: A Pilot Survey with Modest Aperture Telescopes*

[6] Ferrarese, L. et al. (2012) *The next generation virgo cluster survey. Introduction to the survey*

[7] Duc P.-A., et al. (2015) *Applying galactic archeology to massive galaxies using deep imaging surveys*

[8] Cooper A.P. (2010) *Galactic stellar haloes in the CDM model*

[9] Hodges-Kluck Bregman (2014) *Hot Coronae Around Local Spiral Galaxies: A Key Probe of Galaxy Formation Theory*

[10] Klypin et al. 1999 *Where Are the Missing Galactic Satellites?*

[11] Tollerud (2008) *Hundreds of Milky Way Satellites? Luminosity Bias in the Satellite Luminosity Function*

[12] Majewski et al. (2003) *A Two Micron All Sky Survey View of the Sagittarius Dwarf Galaxy. I. Morphology of the Sagittarius Core and Tidal Arms*

[13] Ibata et al. (2001) *Unveiling the environment and faint features of the isolated galaxy CIG 96 with deep optical and HI observations*

[14] Van Dokkum (2014) *First Results from the Dragonfly Telephoto Array: The Apparent Lack of a Stellar Halo in the Massive Spiral Galaxy M101*

[15] Zwaan (1995) *The Tully-Fisher relation for low surface brightness galaxies: implications for galaxy evolution*

[16] Sprayberry (1995) *Properties of the Class of Giant Low Surface Brightness Spiral Galaxies*

[17] Benson (2003) *What Shapes the Luminosity Function of Galaxies?*

[18] S. Phillipps (1992) *Surveys for Low Surface Brightness Galaxies*

[19] Schwartzenberg, J. M.; Phillipps, S.; Parker, Q. A.(1995) *A Survey for Low Surface Brightness Galaxies using Tech Pan Film*

[20] Van Dokkum (2018) *Hunting faint dwarf galaxies using integrated light surveys*

[21] Cebrian, Trujillo (2016) *What do galaxies look-like beyond 31 mag/arcsec2*

[22] Gora- nova et al. (2009) *CFHTLS*

[23] Fliri ,Trujillo (2016): *Beyond 31mag/arcsec^2 : the low surface brightness frontier with the largest optical telescopes*

[24] Kiss et al. (2002) *Small-scale structure of the galactic cirrus emission*

[25] Veneziani et al. (2009) *Properties of Galactic cirrus clouds observed by BOOMERanG*

[26] Jeong et al. (2005) *Far-infrared detection limits – I. Sky confusion due to Galactic cirrus*

[27] Chiboucas et al. (2009,2013) *Faint Dwarf Galaxies in the M81 Group*

[28] Cortese et al (2010) *Diffuse far-infrared and ultraviolet emission in the NGC 4435/4438 system: tidal stream or Galactic cirrus?*

[29] Besla et al. (2016) *Low Surface Brightness Imaging of the Magellanic System: Imprints of Tidal Interactions between the Clouds in the Stellar Periphery*

[30] Duc, Pierre-Alain (2018) *Revisiting Stephan's Quintet with deep optical images*

[31] Ramirez-Moreta e al. (2018) *A giant stream of metal-rich stars in the halo of the galaxy M31*

[32] Sandin, Christer (2014) *The influence of diffuse scattered light. I. The PSF and its role in observations of the edge-on galaxy NGC 5907*

[33] Sandin, Christer (2014) *The influence of diffuse scattered light. II. Observations of galaxy haloes and thick discs and hosts of blue compact galaxies*

[34] Rudick et al.(2010) *Optical Colors of Intracluster Light in the Virgo Cluster Core*

[35] McGaugh, Bothun (1995), AJ, 109, 2019 *Drafts and low surface brightness galaxies*

[36] Laporte, Agnello & Navarro (2018) *Reconciling mass-estimates of ultra-diffuse galaxies*

[37] Wittmann et al (2018) *A population of faint low surface brightness galaxies in the Perseus cluster core*

[38] Mihos et al (2015) *Galaxies at the extremes: UDG in the virgo cluster*

[39] Munoz et al (2015) *Unveiling a Rich System of Faint Dwarf Galaxies in the Next Generation Fornax Survey*

[40] Janssens (2017) *Ultra-diffuse and Ultra-compact Galaxies in the Frontier Fields Cluster Abell 2744*

[41] Javanmardi (2016) *DGSAT: Dwarf Galaxy Survey with Amateur Telescopes. I. Discovery of low surface brightness systems around nearby spiral galaxies*

[42] Shihong Liao (2019) *Ultra-diffuse galaxies in the Auriga simulations*

[43] Bothun et al. (1987) *Extremely low surface brightness galaxies in the Fornax cluster*

[44] Knezek (1993) *Morphology and stellar populations in the gas-rich, giant Low surface brightness galaxies*

[45] Impey, Bothun (1989) *Discovery of a low surface brightness galaxy*

[46] Galaz (2015) *Deep optical images of Malin 1 reveal new features*

[47] Martin (2019) *The formation and evolution of low-surface-brightness galaxies*

[48] Blok and McGaugh (1996) *The dark and visible matter content of low surface brightness*

[49] De Blok (1996) *Does Low Surface Brightness Mean Low Density?*

[50] Papastergis (2018) *The HI content of isolated ultra-diffuse galaxies: A sign of multiple formation mechanisms?*

[51] Phillipps (1993) *The case for low surface brightness galaxies as the absorbers in QSO MgII systems*

[52] Vaisanen (1999) *Detecting the low surface brightness universe*

[53] Vaisanen (1996) *Extragalactic background light*

[54] White & Frenk (1991) *Galaxy formation through hierarchical clustering*

[55] van Dokkum P. et al., 2018, *Nature* 555, 629

[56] Walker, Terry P (1991) *Primordial Nucleosynthesis Redux*

[57] Persic , Salucci (1992) *The Lymann alpha forest at low redshift.Tracing the dark matter filaments*

[58] Bothun et al. (1993) *Low Surface Brightness Galaxies: Evolution without Mass transfer*

[59] Yozin & Bekki (2015) *The quenching and survival of ultra-diffuse galaxies in the Coma cluster*

[60] Rong et al. (2017) *A Universe of Ultra-Diffuse Galaxies: Theoretical Predictions from* Λ*CDM Simulations*

[61] Chen (2010) *Contradiction between strong lensing statistics and a feedback solution to the cusp/core problem*

[62] Fliri ,Trujillo: *The IAC Stripe 82 Legacy Project: a wide-area survey for faint surface brightness astronomy*

[63] Janssens (2016) *Ultra diffuse galaxies in the Abell 2744*

[64] Roman (2019) *Discovery of a red ultra-diffuse galaxy in a nearby void based on its globular cluster luminosity function*

[65] Bergmann (2003) *Spectroscopy of LSBG with Hobby Eberly Telescope*

[66] Ragaigne (2003) *A search for Low Surface Brightness galaxies in the near-infrared*

List of Tables

List of Figures

Appendix A

Appendix A - Make tools

This appendix is just a brief summary of the basics commands to run a makefile and how to write a make script. More details can be found at the webpage:
$https : //www.gnu.org/software/make/manual/make.html\#toc - An - Introduction - to - Makefiles$.

Firstly, the file must have a *.mk* extension. Then, a simple makefile usually starts with:

```
.ONESHELL:
```

which is necessary to read an information block and not to read only one line each time. The command:

```
all:
```

defines the final target which will be created by using any variables.

The variable (or variables) in the rule which has to be written in order to build the target is callable with the keyword $< (or $^). Moreover, I refer to the name of the target with @, to the length of the variable with the command $(words $^) and to the HDU of the FITS image with -g$$n (or –hdu=$$n).

The rule must always follow the declaration of the variables.

The command line:

```
make name-file.mk
```

runs the name-file.mk script from the bash shell.

Appendix B

Appendix B - Pipeline structure

With this appendix I explain the basic structure of the Hipercam-pipeline. The pipeline is public and it is available on Gitlab at the webpage $< https://gitlab.com/GiuliaGolini/hipercam-pipeline >$. Its download provides three main folders: one of them is used for the input images, one other for Make and Python files and the last one is the output directory.

To run the pipeline you have to use the following command line:

```
./local/bin/make (-j4)
```

In this particular pipeline, each output image will be located in a different sub-directory and it will have the same name of the corresponding input image from the input directory. This operating mode is useful to trace any bugs and eventually, to check image by image.

To do this, for each make file I defined:

```
#  The output directory
outdir = $(BDIR)/output-directory-name
# The input directory
indir = $(INDIR)/input-directory-name
# The names of the input images
images := $(wildcard $(indir)/*.fits)
base-names = $(foreach input,$(inputs),$(notdir $(subst .fits,,$(input))))
# The names of the output images
output-images = $(foreach base-name,$(base-names),$(cb-outdir)/$(base-name).fits)
```

In this specific example, the command *foreach* works as a loop: for each name in the set of base-names write the name of the output image (the same name of the input one but in another directory) in the output directory.

The steps of the pipeline are (in chronological order):

- build the bias frame with raw images;
- correct all the individual images of the corresponding bias frame;
- build the first version of flat with bias corrected images;
- correct all the individual images of the corresponding flat frame;
- build the mask of individual flat corrected images;
- build the second version of flat with masked images;
- correct all the individual images of the corresponding second version of flat frame;
- arrange CCD image and correct all the individual images of gain;
- correct all the individual images of sky by using a plane sky model;
- astrometric calibration of band images;
- photometric calibration of band images;
- resample images on a common larger image;
- stack all CCD images (one filter each time);
- build the RGB image.

Each script of the pipeline ends with:

```
$(mtexdir)/script.tex: $(output-images) | $(mtexdir)
touch $@
```

which is necessary to build the final target.

Appendix C

Appendix C - Gnuastro tools

Gnuastro is a very useful software consisting of separate programs and libraries that allow to operate with astronomical data. This appendix is a summary of the major Gnuastro programs and commands which I used to build the pipeline. To have more details on how each individual program works, see the tutorial at *<https://www.gnu.org/software/gnuastro/manual/gnuastro.pdf>*. The last version of Gnuastro is avaiable at *http://akhlaghi.org/gnuastro.pdf*.

C.1 Astfits, Aststatistics

The first program that I employed is *astfits* which allows to print the cube information of the FITS file. In particular, I used *astfits* to manipulate the FITS file and create images with the same cube format of the initial raw images (20 extensions = 4 windows x 5 filters). I did it by computing:

```
astfits $<  --copy=0 --output=$@
astfits $< --hdu=0 --copykeys=1:-1 --output=$@ --outhdu=0
astfits $@ --remove=1
```

After that, *aststatistics* is useful to visualize the statistics and the histogram of the image. For example, *aststatistics* is used to build the normalization factor, that is the median of the pixel values of the image:

```
vnorm=$$(aststatistics $< --hdu=$$n --median)
```

C.2 Astnoisechisel

Astnoisechisel is another important program. Though the analysis of the input image, *astnoisechisel* creates an output FITS file of 4 extensions (HDU): the first HDU contains the input image to which the sky (that is detected with *astnoisechisel*) was subtracted, the second HDU is the mask of the input image, the third extension is the sky model and the last is the rms of the sky. The mask is an image containing 0 and 1 values: value=1 is assigned to pixels on which the software has recognized any emission coming from a real source and value=0 on "only noise" pixels. *Astnoisechisel* allows doing noise band detection of diffuse signal by dropping the noise threshold to see ever fainter

sources. To do this, *astnoisechisel* automatically "erode" the input image by filling the closest pixels near the identified real sources under a certain threshold. The result of this process is a discrete segmentation of sorted pixels. I report as an example the command line that I used to obtain the mask of the galaxy in order to estimate its brightness:

```
astnoisechisel $< --hdu=$$n  --qthresh=0.15 --detgrowquant=0.6 --tilesize=25,25
```

In this case: *–qthresh* is the quantile threshold to apply to the convolved image; *–detgrowquant* is the quantile limit to "grow" the final detections and *–tilesize* is the size of each tile for the tessellation.

C.3 Astarithmetic

Astarithmetic is package that allows to operate mathematically with cubes frames. In particular, when I had to build the Bias frame (or the Flat Field) I used *astarithmetic* to compute sigma-clipping between images:

```
astarithmetic $^ -g$$n $(words $^) 3 0.2 sigclip-mean
```

Moreover, I used *astarithmetic* when I had to subtract each Bias image to the individual HDUs or when I had to normalize images using its median value:

```
astarithmetic $< --hdu=$$n $(word 2,$^) --hdu=$$n -
astarithmetic $< --hdu=$$n $$vnorm /
```

Astarithmetic is also necessary to divide every HDUs by Flat Field:

```
astarithmetic $< --hdu=$$n $(word 2, $^) --hdu=$$n /
```

or when masking:

```
astarithmetic $< --hdu=$$n $(word 2,$^) --hdu=$$n 1 eq nan where
```

C.4 Astsegment, Astmkprof

Segment is another significant program that allows to break the detection image into objects. *Segment* needs a configuration file and it is run with the command line:

```
astsegment $$input-image --config=astsegment.conf
```

To solve the problem of the u′ filter astrometry calibration, I appealed *astmkprof* in order to build a mock astronomical profile which will be applied to u′ images:

```
astmkprof --kernel=moffat,3,2.8,5 --oversample=1
```

C.5 Astconvolve, Astmkcatalog, Astmatch, Asttable and Astcrop

Before doing the astrometric calibration, I blurred the images (smoothing) by mixing pixel values with a spatial domain convolution. This method appeals *astconvolve* to raise up the faintest sources of the images:

```
astconvolve $< --kernel=$(word 2,$^) --type=float32 --domain=spatial --khdu=1
```

I have also used *Makecatalog* to obtain a catalogue with RA, DEC, magnitude and brightness of the detected astronomical objects. I needed *Match* to find the common sources between the catalogue that I have built and the SDSS catalogue ($1''$ of tolerance). Subsequently, I used *Table* to save the difference-factors (δ_m) to do the photometric calibration. These steps are summarized in the following:

```
astmkcatalog $< --ra --dec --magnitude --zeropoint=22.5 --config=astmkcatalog.conf
astmatch $(word 2,$^) $<
                --ccol1=RA_ICRS,DE_ICRS --ccol2=RA,DEC --aperture=1.0/3600.0
                --config=astmatch.conf
asttable $<  -cimag,MAGNITUDE  | awk '{print $$1-$$2}' > $$im_dif
```

Finally, I employed *Crop* to select polygonal regions around the ultra diffuse galaxy in order to compute its final brightness.

```
astcrop $< --mode=img --polygon=1473,1586:2618,1574:2600,3549:1386,3338
astcrop $< --hdu=1 --mode=wcs --center=20.8643733,-0.6237515 --width=0.01
```